NASA/TM—2016-219144

Improving Free-Piston Stirling Engine Power Density

Maxwell H. Briggs
Glenn Research Center, Cleveland, Ohio

September 2016

NASA STI Program . . . in Profile

Since its founding, NASA has been dedicated to the advancement of aeronautics and space science. The NASA Scientific and Technical Information (STI) Program plays a key part in helping NASA maintain this important role.

The NASA STI Program operates under the auspices of the Agency Chief Information Officer. It collects, organizes, provides for archiving, and disseminates NASA's STI. The NASA STI Program provides access to the NASA Technical Report Server—Registered (NTRS Reg) and NASA Technical Report Server—Public (NTRS) thus providing one of the largest collections of aeronautical and space science STI in the world. Results are published in both non-NASA channels and by NASA in the NASA STI Report Series, which includes the following report types:

- TECHNICAL PUBLICATION. Reports of completed research or a major significant phase of research that present the results of NASA programs and include extensive data or theoretical analysis. Includes compilations of significant scientific and technical data and information deemed to be of continuing reference value. NASA counter-part of peer-reviewed formal professional papers, but has less stringent limitations on manuscript length and extent of graphic presentations.

- TECHNICAL MEMORANDUM. Scientific and technical findings that are preliminary or of specialized interest, e.g., "quick-release" reports, working papers, and bibliographies that contain minimal annotation. Does not contain extensive analysis.

- CONTRACTOR REPORT. Scientific and technical findings by NASA-sponsored contractors and grantees.

- CONFERENCE PUBLICATION. Collected papers from scientific and technical conferences, symposia, seminars, or other meetings sponsored or co-sponsored by NASA.

- SPECIAL PUBLICATION. Scientific, technical, or historical information from NASA programs, projects, and missions, often concerned with subjects having substantial public interest.

- TECHNICAL TRANSLATION. English-language translations of foreign scientific and technical material pertinent to NASA's mission.

For more information about the NASA STI program, see the following:

- Access the NASA STI program home page at http://www.sti.nasa.gov

- E-mail your question to help@sti.nasa.gov

- Fax your question to the NASA STI Information Desk at 757-864-6500

- Telephone the NASA STI Information Desk at 757-864-9658

- Write to:
  NASA STI Program
  Mail Stop 148
  NASA Langley Research Center
  Hampton, VA 23681-2199

NASA/TM—2016-219144

Improving Free-Piston Stirling Engine Power Density

Maxwell H. Briggs
Glenn Research Center, Cleveland, Ohio

National Aeronautics and
Space Administration

Glenn Research Center
Cleveland, Ohio 44135

September 2016

Level of Review: This material has been technically reviewed by technical management.

Available from

NASA STI Program
Mail Stop 148
NASA Langley Research Center
Hampton, VA 23681-2199

National Technical Information Service
5285 Port Royal Road
Springfield, VA 22161
703-605-6000

This report is available in electronic form at http://www.sti.nasa.gov/ and http://ntrs.nasa.gov/

Contents

List of Tables

List of Figures

Improving Free-Piston Stirling Engine Power Density

Maxwell H. Briggs
National Aeronautics and Space Administration
Glenn Research Center
Cleveland, Ohio 44135

Abstract

Analyses and experiments demonstrate the potential benefits of optimizing piston and displacer motion in a free piston Stirling Engine. Isothermal analysis shows the theoretical limits of power density improvement due to ideal motion in ideal Stirling engines. More realistic models based on nodal analysis show that ideal piston and displacer waveforms are not optimal, often producing less power than engines that use sinusoidal piston and displacer motion. Constrained optimization using nodal analysis predicts that Stirling engine power density can be increased by as much as 58% using optimized higher harmonic piston and displacer motion. An experiment is conducted in which an engine designed for sinusoidal motion is forced to operate with both second and third harmonics, resulting in a maximum piston power increase of 14%. Analytical predictions are compared to experimental data showing close agreement with indirect thermodynamic power calculations, but poor agreement with direct electrical power measurements.

Introduction

Free-Piston Stirling Engines

Practically achievable Stirling engines typically achieve high thermal efficiency (net work out/heat in) but have low power density (power per unit volume) when compared to internal combustion engines [1] [2] [3]. One potential method of increasing power density is to enforce piston and/or displacer motion that more closely approximate those of the ideal Stirling cycle. The ideal Stirling thermodynamic cycle consists of isothermal compression and expansion processes and constant volume heat addition and heat removal processes. Achieving the ideal cycle requires that the piston and displacer dwell and abruptly change direction throughout the cycle, which can difficult to achieve in both kinematic and free-piston configurations. Designers typically sacrifice ideal motion for practically achievable motion, most often converging on a mechanical linkage or electrical control scheme that imposes sinusoidal or nearly sinusoidal motion [4] [5] [6]. While there are certainly benefits to choosing sinusoidal motion, it is not the optimal choice since sinusoidal motion reduces power density. There are some patents based on achieving piston motion that more closely approximates ideal motion in kinematic Stirling engines [7] [8], but the author was unable to find any examples of a functional kinematic Stirling which uses non-sinusoidal motion for the purpose of improving performance. Furthermore, the author could find no examples of attempts to achieve performance benefits through non-sinusoidal motion on free-piston Stirling engines.

Free-piston Stirling devices are closed-cycle regenerative devices that can achieve high efficiencies (>50% of Carnot efficiency is achievable in well-made engines) [1]. Applications include cryo-coolers [9] [10], natural gas co-generation units [11] [12] [13], solar-dynamic power conversion [14] [15] [16], and nuclear dynamic power conversion [17] [18] [19] [20] [21]. They are typically used in applications which have high fuel costs or in systems that require closed cycle operation. High efficiency and closed-cycle operation are both requirements of space power systems, making free-piston Stirling engines candidates for these applications. They are the key technology in NASA's Advanced Radioisotope Generator (ASRG) project because their high efficiency allows NASA to increase the number of missions it can fly using the limited supply of plutonium-238 [20] [21] [22]. They also trade favorably in low to moderate fission power applications because their high efficiency requires less heat input from the reactor and reduces heat rejection requirements, reducing the mass of the reactor shield and the radiators [17] [18] [19] [23].

Stirling engines have been considered for use in several terrestrial applications including automotive engines, solar dish-Stirling power plants, and residential co-generation systems, especially when rising fossil fuel costs indicate that their high efficiency can make them economical. However, the low power density and high cost of Stirling engines typically prevent them from competing when fuel costs are low and internal combustion or other open-cycle engines are viable.

The Stirling Thermodynamic Cycle

The Ideal Stirling thermodynamic cycle is characterized by isothermal compression/expansion and constant volume regenerative heat addition/removal, as

shown in Figure 1. Although the Stirling thermodynamic cycle is well-defined, the term "Stirling" is used imprecisely to describe a wide variety of closed cycle reciprocating regenerative devices. This can be misleading because the Stirling thermodynamic cycle is not restricted to closed-cycle regenerative reciprocating machines, and many closed-cycle regenerative reciprocating machines that are described as "Stirling" engines do not use the ideal Stirling thermodynamic cycle.

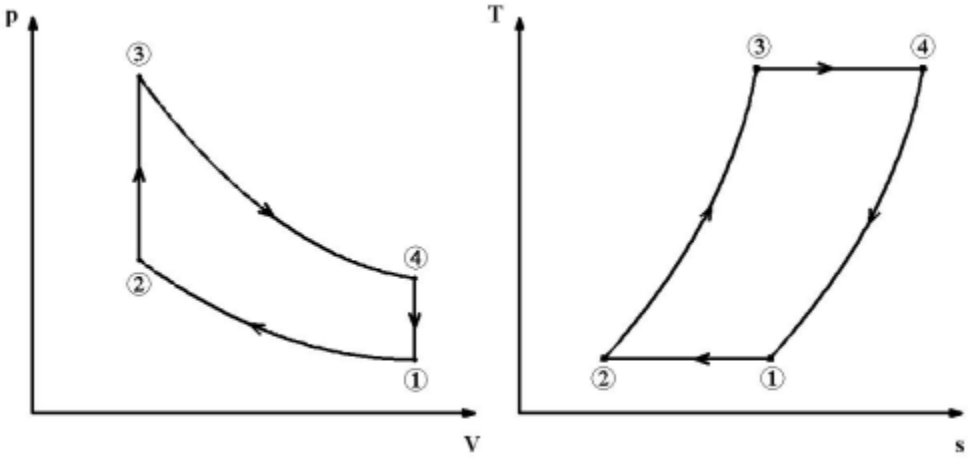

Figure 1. P-V and T-S diagrams of the Ideal Stirling Cycle

Although the Stirling thermodynamic cycle need not be realized through reciprocating motion or any specific configuration, the ideal Stirling engine has historically been presented in a configuration resembling Figure 2, referred to as the alpha-configuration. In this configuration, there is an expansion piston and a compression piston, with a regenerator in between. The combined volume of the expansion space and compression space are typically referred to as the working space. Any volume not traversed by a piston is referred to as "dead volume". Sometimes a distinction is made between dead volume that is part of the heat exchangers and clearance volume within the compression and expansion spaces, although they can be lumped

together for analysis purposes. Analysis of the ideal Stirling cycle typically assumes zero dead volume / zero clearance volume and perfect regeneration. The analysis in Appendix I considers the more general case of non-zero dead volume.

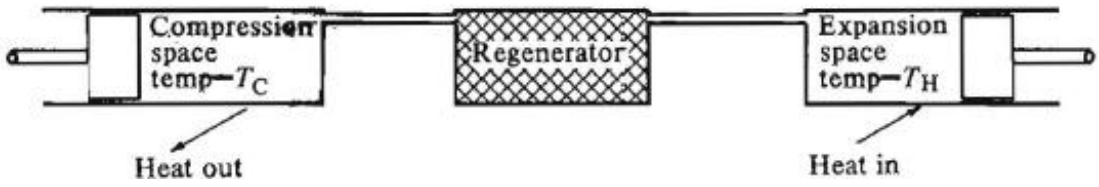

Figure 2 - Conceptual Layout of an Ideal Stirling Convertor, alpha configuration [24].

(Reprinted with permission from Oxford University Press)

During the constant volume heat rejection process, both pistons move to the left, keeping the working space volume constant, until all of the hot gas is cooled through the regenerator and moves into the compression space. During the constant temperature compression phase the compression piston travels to the right while the expansion piston remains fixed. During the compression process heat is removed from the gas, keeping the compression isothermal. During the constant volume heat addition process both pistons travel to the right, again keeping the working space volume constant, until all of the cold gas is heated through the regenerator and passes into the expansion space. During the constant temperature expansion process, the expansion piston moves to the right while the compression piston remains fixed. Heat is added during expansion, making this process isothermal. For an ideal Stirling engine, as the regenerator effectiveness approaches unity the external heat addition and rejection requirement during the constant volume processes approaches zero, and the Stirling cycle efficiency approaches the Carnot efficiency (Figure 3). The power density of an ideal Stirling engine with zero dead volume is independent of regenerator effectiveness and is

proportional to the natural log of the volume ratio (Figure 3.). The details of the analysis leading to these conclusions can be found in Appendix I.

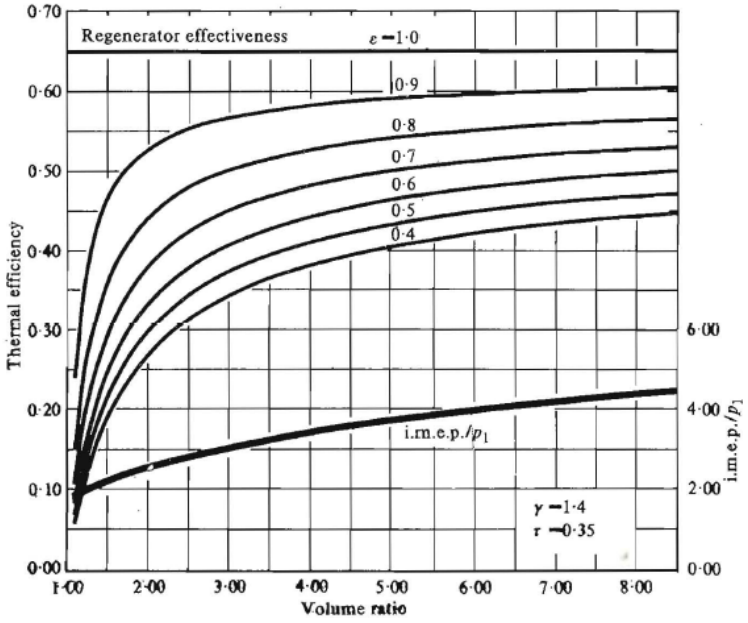

Figure 3 - Thermal efficiency of the ideal Stirling cycle plotted against volume ratio for several values of regenerator effectiveness [24]

(Reprinted with permission from Oxford University Press)

Ideal vs. Sinusoidal Piston/Displacer Motion

Ideal piston motion requires the piston and/or displacer to dwell during periods within a cycle and abruptly change direction during others. This requires large forces which have been difficult to achieve. Engine designers typically trade ideal motion for practically achievable motion, most often settling on sinusoidal motion. Analysis of an engine with isothermal gas volumes under the constraint of sinusoidal motion is called the Schmidt analysis after Gustav Schmidt [25], and is shown in detail in Appendix I. Isothermal engines with perfect regeneration operating under the Schmidt cycle achieve the same efficiency as the ideal Stirling engine, which is equal to the Carnot efficiency.

The sinusoidal piston motion associated with the Schmidt cycle does, however, reduce power density. Ideal Stirling cycle piston motion results in higher pressure ratio because heat addition and heat rejection both take place at constant volume. In addition, since the pistons dwell at their inmost position, the ideal cycle can achieve a higher volume ratio than a Schmidt cycle operating for the same piston amplitudes. When engines are forced to use sinusoidal motion, expansion during the heating process and cooling during the compression process reduce the pressure ratio, reducing power density. Power density is further reduced because the phase angle between the pistons prevents the pistons from both being at top-dead-center or bottom-dead-center at the same time, which reduces the working space volume amplitude. These concepts are fleshed our more rigorously in Appendix I and the Analysis sections below.

Free-Piston Stirling Engines and the Beta-Configuration

Stirling engines can be categorized by a number of their design features, one of which is the method used to couple the motions of the pistons or the piston/displacer system. The term "kinematic" is used to refer to Stirling engines that use mechanical linkages to connect the pistons (or the piston and displacer). This mechanical linkage is also typically used to extract power from the cycle. An alternative design termed "free-piston", uses internal gas dynamics to synchronize the motions of the piston and displacer. Since free-piston engines do not have linkages that can be used for power removal they typically attach permanent magnets to the piston and use linear alternators to extract power from the piston. Free-piston designs typically use one piston and one displacer in a common cylinder (the beta configuration), as opposed to the two piston (alpha configuration) arrangements that are shown in Figures 2. A displacer is

distinguished from a piston in that it “displaces” gas from the compression space to the expansion space without affecting the working space volume. This results in little or no net work done on or by the displacer. Displacers are typically used on free-piston engines because two-piston designs require a second linear alternator to operate at the hot-end of the engine. This is undesirable because it limits the hot-end temperature and adds additional mass and volume to the system. Figure 4 shows a schematic of a free-piston engine cross-section.

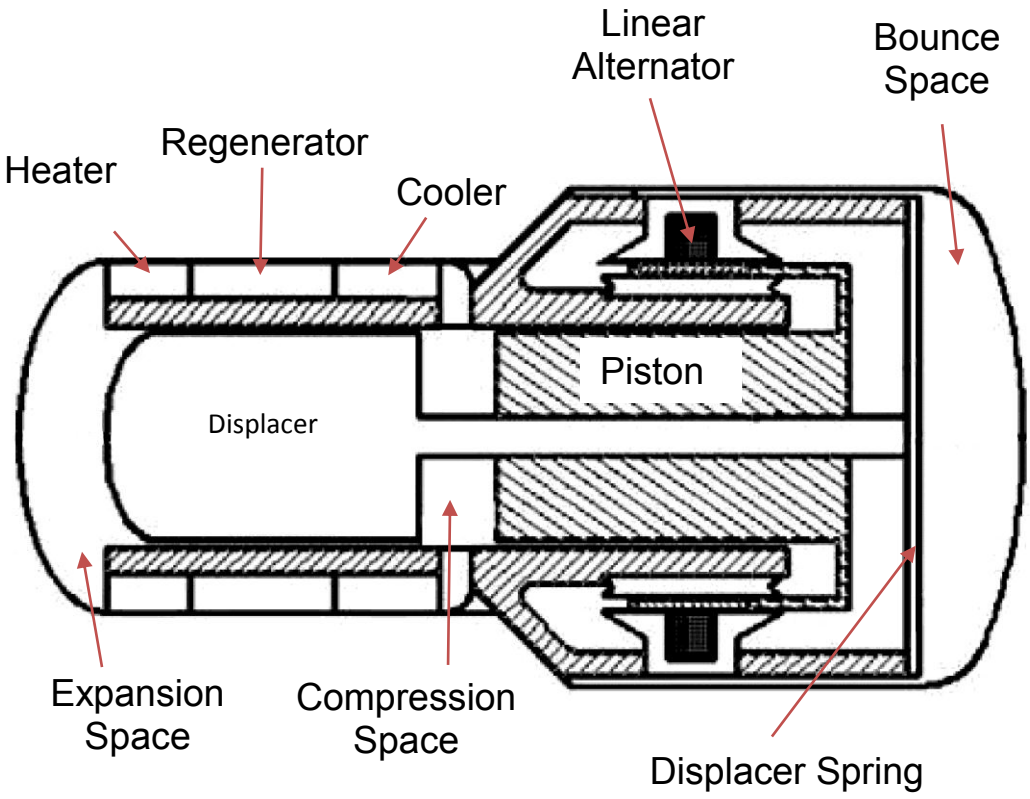

Figure 4 - Cross-section of a free-piston Stirling engine, beta config.

The ideal motion of the beta configuration differs from the ideal motion of the alpha configuration, in that constant volume processes are obtained by allowing the displacer to move while the piston remains fixed. Figure 5 shows a schematic of the

ideal piston motion of a Stirling engine in the beta configuration, as well as a plot of ideal piston and displacer position. Process 1-2 shows constant temperature compression, in which the displacer remains still, minimizing the expansion space volume and the piston compresses the gas as heat is removed through the cooler. Process 2-3 shows constant volume heat addition, in which the displacer moves gas from the cold side to the hot side, through the regenerator, while the piston remains still. Process 3-4 is a constant temperature expansion process, in which the expansion of the gas moves the piston and the displacer moves along with it to minimize volume of the compression space. The work done during the expansion process minus the work done during the compression process is the usable power of the Stirling cycle. In free-piston engines this power is typically extracted through the linear alternator. Process 4-1 is a constant volume heat removal process in which the displacer moves gas from the hot to the cold side, through the regenerator, while the piston remains still.

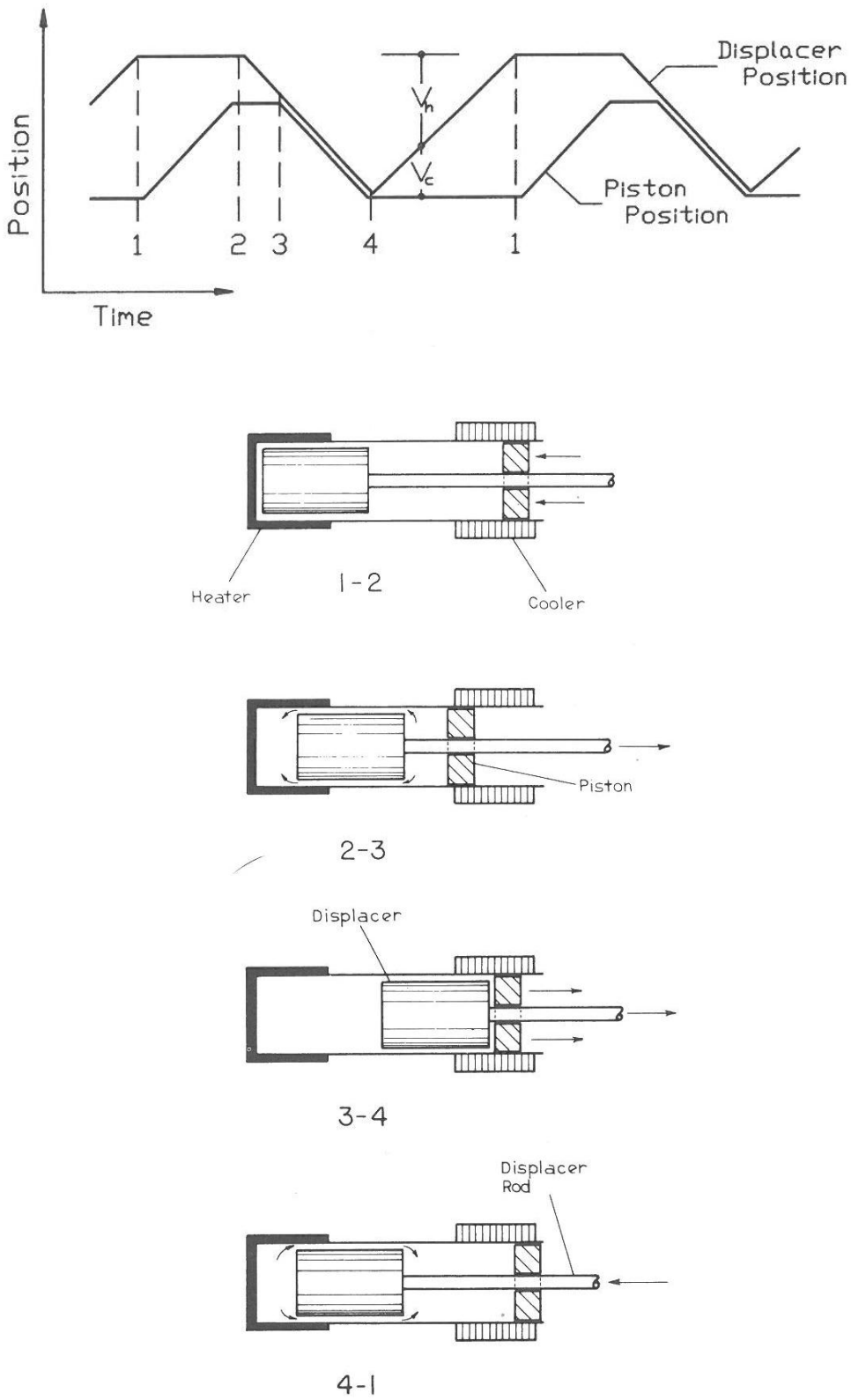

Figure 5 - Schematic and plots of ideal piston and displacer motion, beta config [26].

(Reprinted with permission from Oxford University Press)

The volume variations of the beta-configuration can always be converted to equivalent volume variations for the alpha configuration, so analysis of the two are equivalent.

Analysis

In this section, several analytical methods illustrate the potential benefits of optimizing piston and displacer motion. The results of these analyses illustrate the feasibility of improving engine performance using non-sinusoidal piston and/or displacer motion.

Isothermal Analysis - Ideal Motion vs. Sinusoidal Motion in Highly Idealized Stirling Engines

The classical analysis of Stirling convertors resulting in a closed-form solution assumes the following [3] [24]:

1. Gas volumes are isothermal at either the hot-end temperature or the cold-end temperature or the regenerator temperature
2. The instantaneous pressure is constant throughout the working space
3. Working fluid behaves as an ideal gas with constant specific heat
4. No leakage of working fluid between gas volumes
5. The regenerator has a linear temperature profile that is constant in time

The Schmidt analysis adds the additional assumption that the expansion and compression pistons move sinusoidally, with a phase shift, α, and also results in a closed form solution.

Imposing the following additional constraints allows for more straightforward comparisons to be made between engines operating with ideal and sinusoidal motion:

1. Perfect regeneration
2. No dead volume (All heat exchangers including regenerator have no volume)

This list of assumptions is idealistic and not representative of real engines. These shortcomings are addressed in later sections, but using closed form solutions on simplified engines provides a useful demonstration of the fundamentals of the problem.

A full version of the well-known ideal Stirling analysis and Schmidt analysis can be found in Appendix I. The work per cycle predicted by the ideal and Schmidt analyses for zero dead volume appears equations 1 and 2 respectively.

$$W_{Ideal} = mRT_{CS}\ln(r)(\tau - 1) \qquad (1)$$

$$\mathbf{W_{Schmidt} = 2\pi mRT_{CS}\left(\frac{\tau\kappa}{(\tau+\kappa)^2}\right)\left(\frac{1-\sqrt{1-b^2}}{b^2\sqrt{1-b^2}}\right)(\tau-1)\sin\alpha} \qquad (2)$$

Where m is the gas mass, R is the working fluid gas constant, T_c is the cold-end temperature, r is the ideal cycle working space volume ratio, τ is the temperature ratio, T_{ES}/T_{CS} (where ES is expansion space, CS is compression space), κ is the Schmidt cycle swept volume ratio, and α is the phase angle between the expansion and compression volumes. The constants required for evaluation are given by:

$$b = \frac{\sqrt{\tau^2+2\kappa\tau\cos(\alpha)+\kappa^2}}{K_t} \qquad (3)$$

$$K_t = \frac{2T_{ES}C_2}{V_{CS,sw}}$$

$$C_2 = \left(\frac{V_{CS,sw}}{2T_{CS}} + \frac{V_{CS,cl}}{T_{CS}} + \frac{V_C}{T_C} + \frac{V_R}{T_{Eff\,R}} + \frac{V_H}{T_H} + \frac{V_{ES,cl}}{T_{ES}} + \frac{V_{ES,sw}}{2T_{ES}}\right)$$

A choice must be made about how relate the sinusoidal piston motion of the Schmidt cycle to the ideal Stirling piston motion in a way that gives useful comparisons. This is not straight-forward because the appropriate choice of constraints depends on the operational constraints of an individual engine. One can argue that the ideal Stirling and Schmidt cycles should be constrained to have common maximum and minimum working space volumes, so that power differences are not the result of differences in working space amplitude. Using this method, increased power density of the ideal cycle is solely the result of holding the working space at constant volume during heat addition and removal. It does not take into account the fact that, for the same limits of piston motion, the ideal cycle can achieve higher working volume amplitudes and therefore higher volume ratios. Alternatively the cycles could be constrained to have common expansion volume amplitude and compression volume amplitude for both cycles, allowing the ideal cycle to achieve higher working space volume amplitude than the Schmidt cycle. Note that there are several other possible choices for constraints which are not considered (i.e. setting maximum pressure of the Schmidt and ideal cycles equal or constraining the out limits of piston and displacer motion and leaving the in limit unconstrained).

Using common values for the working volume amplitude gives the following relationship for the ideal working space volume ratio, r, in terms of k and α (See Appendix I for derivation):

$$\mathbf{r} = \frac{(\kappa+1) + \sqrt{\kappa^2+2\kappa\cos(\alpha)+1}}{(\kappa+1) - \sqrt{\kappa^2+2\kappa\cos(\alpha)+1}} \qquad (4)$$

Substituting equation 4 into equation 1 and taking the ratio of ideal cycle work to Schmidt cycle work gives the increase in power density for engines operating with ideal piston motion. These results are plotted in Figures 6-7 for several values of κ, τ, and α. Of specific interest is the behavior of these curves with swept volume ratio, κ equal to one and a phase angle of π/2, because these conditions maximize Schmidt cycle power and many practical engines operate near this condition. Stirling engine temperature ratio can range from nearly one for small demonstrators powered by body heat to three in high efficiency engines.

Figure 6 plots the ideal to Schmidt power ratio versus the ideal cycle volume ratio at a phase angle of π/2. In this case the ideal cycle volume ratio, r, is a function of only the Schmidt cycle expansion volume ratio, κ, which is varied from .05 to 20. The power ratio is a multivalued function with higher power density ratio corresponding to values of κ less than one and higher power density ratio corresponding to κ greater than one. The ideal cycle power is greater than the Schmidt power over the entire operating envelope. The minimum power ratio of 1.36 occurs at minimum ideal cycle volume ratio, which corresponds to κ equal to one.

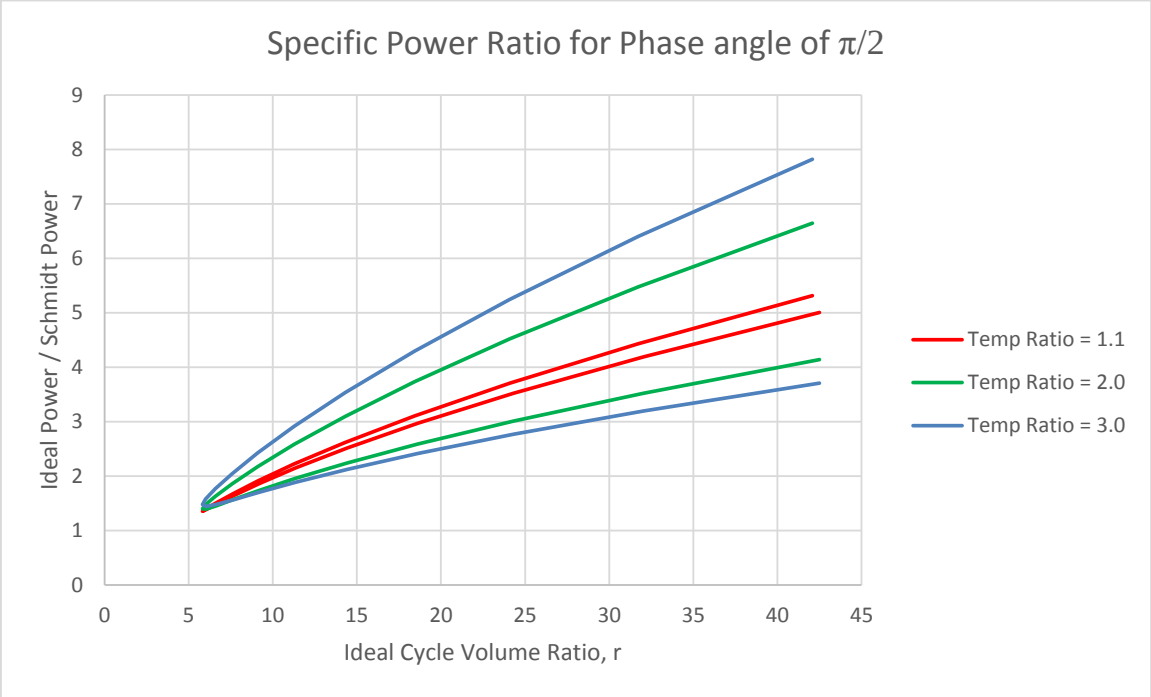

Figure 6 – Ideal to Schmidt Cycle Power Ratio vs. Ideal Cycle volume ratio for a phase angle of π/2.

Figure 7 plots the power ratio versus the ideal cycle volume ratio at a temperature ratio of 2.5. In this case the ideal cycle volume ratio, r, is a function of only the phase angle, α, which was varied from zero to π. These functions are not multivalued because κ is a constant in each curve. The minimum power density ratio of 1.34 occurs in the limit as r approaches one on the κ equal to one curve. This point is of little interest because Schmidt and ideal cycle power both approach zero at this condition. At the more realistic operating condition, where the phase angle is close to π/2 the ideal cycle volume ratio is near 6 corresponding to a power density ratio of 1.44. Appendix I includes an analysis of the limits of the work ratio as the phase angle approaches zero and π, and explains the difference in the trends between the cases of κ equal to one and κ not equal to one.

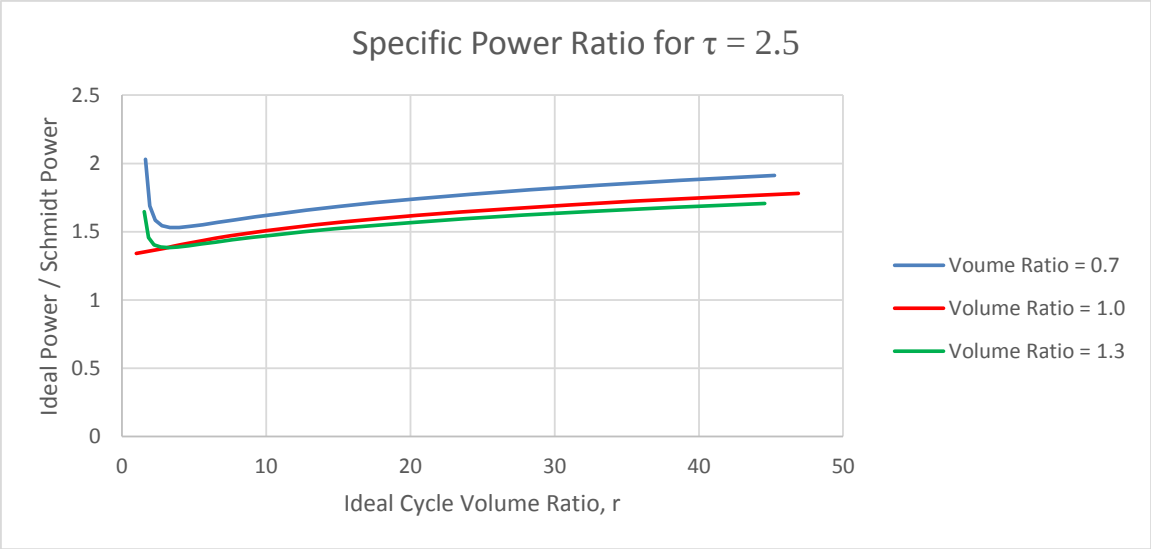

Figure 7 - Ideal to Schmidt Cycle Power Ratio vs. Ideal Cycle volume ratio for temperature ratio of 2.5 for Schmidt cycle swept volume ratios of 0.7, 1.0, and 1.3.

Figures 6 and 7 consider only ideal engines that are constrained to have the same minimum and maximum working space volumes as the Schmidt cycle. Under these conditions the ideal cycle achieves higher cyclic power than the Schmidt cycle throughout the entire operating envelope. The ratio of ideal work to Schmidt work is lowest when the Schmidt cycle swept volume ratio, κ, is equal to one. The power produced by the Schmidt cycle is maximized at a phase angle of π /2 and approaches zero as the phase angle approaches zero or π, so engines typically operate with a compression to expansion space phase angle near π / 2. For this reason the behavior of these curves at extreme phase angles (0 and π) is of less interest than the behavior of the curve in a range near $\pi/2$. Figures 6 and 7 show that the ideal cycle produces at least 34% more power than the Schmidt cycle, with larger improvements possible at higher ideal cycle volume ratios.

A less restrictive method of comparing power density is to require the ideal cycle expansion and compression volume amplitudes to be equal those of the Schmidt cycle,

and allowing the ideal cycle to run at higher working space amplitude. Under this set of constraints the swept volume ratio of the Schmidt cycle, κ, is forced to unity and the ideal working space volume ratio, r, remains an independent variable, so work ratio becomes:

$$\frac{\mathbf{W_{ideal}}}{\mathbf{W_{Schmidt}}} = \frac{\mathbf{\ln(r_{Ideal})}}{\mathbf{2\pi\left(\frac{\tau}{(\tau+1)^2}\right)\left(\frac{1-\sqrt{1-b^2}}{b^2\sqrt{1-b^2}}\right)\sin\alpha}} \quad (5)$$

This shows that the work ratio is proportional to ln(r), in theory ranging from negative infinity to positive infinity. However, running an ideal Stirling engine at a lower working space volume ratio than that of the equivalent Schmidt cycle would be counterproductive, so the Schmidt cycle working space volume ratio is the practical lower limit for ideal cycle volume ratio. Equation 6 is used to set a lower bound on the ideal cycle working volume ratio equal to the Schmidt cycle working volume ratio (Derivation in Appendix I).

$$\mathbf{r_{Ideal,lower\ bound}} = \mathbf{r_{Schmidt}} = \frac{\sqrt{2}+\left(\sqrt{1+\cos(\alpha)}\right)}{\sqrt{2}-\left(\sqrt{1+\cos(\alpha)}\right)} \quad (6)$$

Figures 8-10 show the ratio of ideal work to Schmidt work as a function of r for several values of τ and α with the minimum r value defined by equation 6.

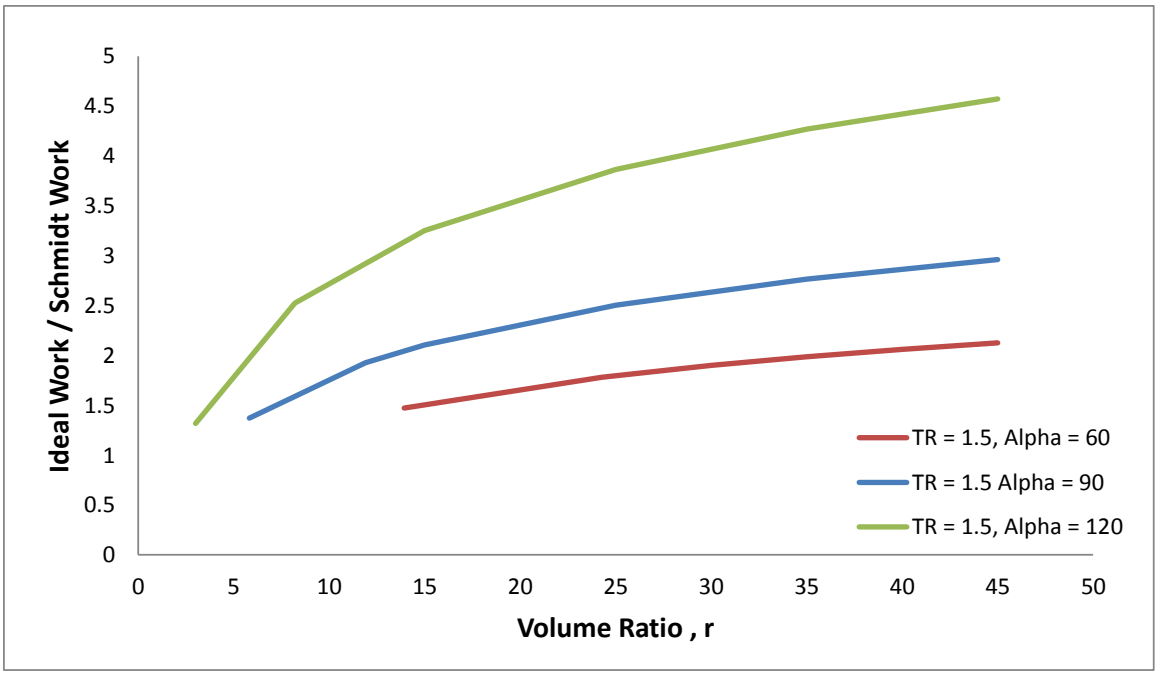

Figure 8 - Ratio of work produced by the ideal Stirling cycle to work produced by the Schmidt cycle assuming equal maximum expansion and compression space volumes and $\tau = 1.5$, for alpha equal to 60, 90 and 120 degrees

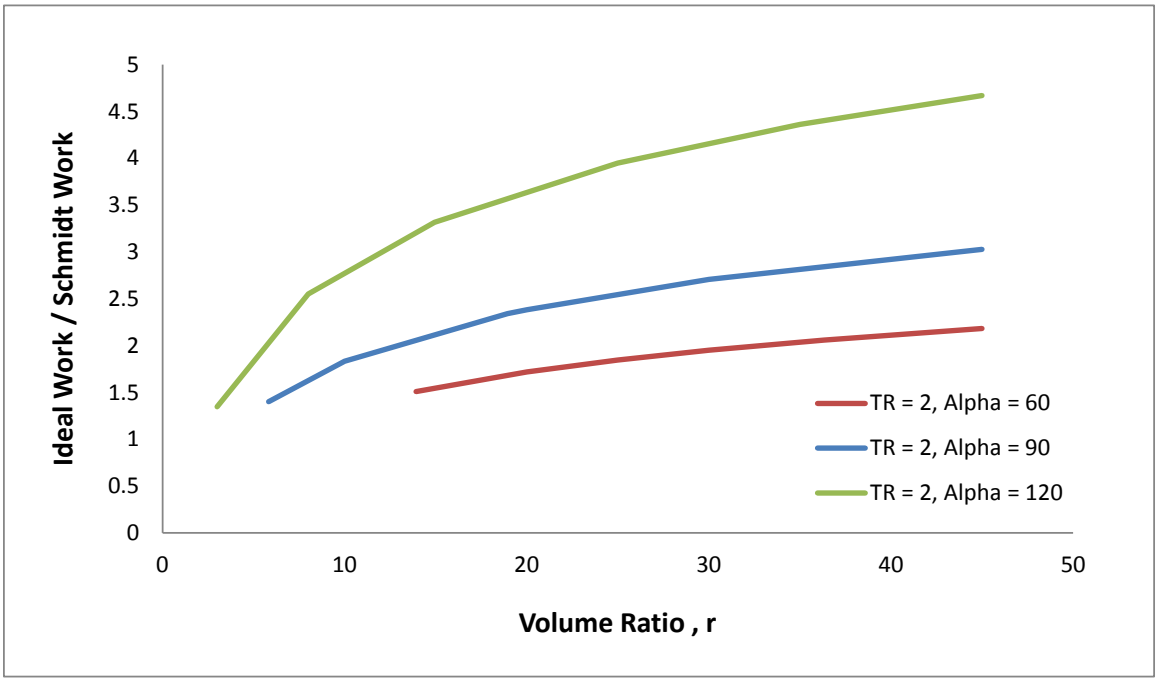

Figure 9 - Ratio of work produced by the ideal Stirling cycle to work produced by the Schmidt cycle assuming equal maximum expansion and compression space volumes and $\tau = 2.0$, for alpha equal to 60, 90 and 120 degrees

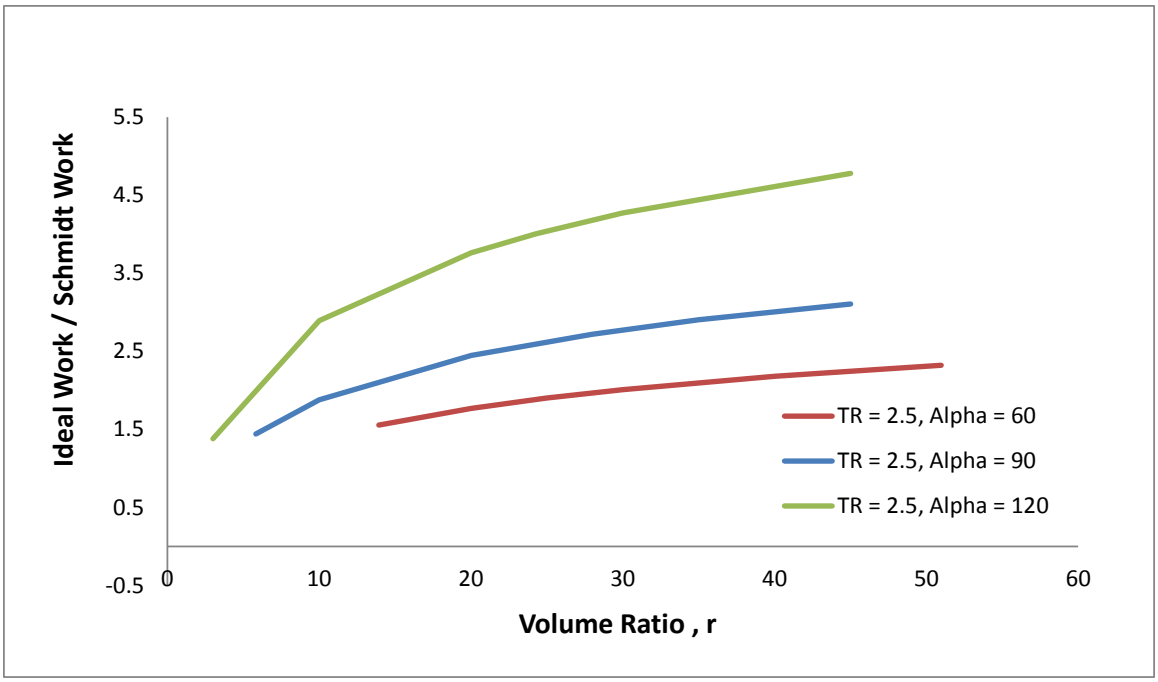

Figure 10 - Ratio of work produced by the ideal Stirling cycle to work produced by the Schmidt cycle assuming equal maximum expansion and compression space volumes and $\tau = 2.5$, for alpha equal to 60, 90 and 120 degrees

Considering only the case of swept volume ratio equal to one and a single temperature ratio of 2.5 allows the two sets of constraints examined above to be compared (Figure 11). Figure 11 shows that constraining the limits of piston motion to be equal for both the Schmidt and ideal cycles, allowing the ideal working space volume amplitude to be higher than the Schmidt cycle working space amplitude results in greater increases in power density than when both cycles are forced to have the same working space amplitude.

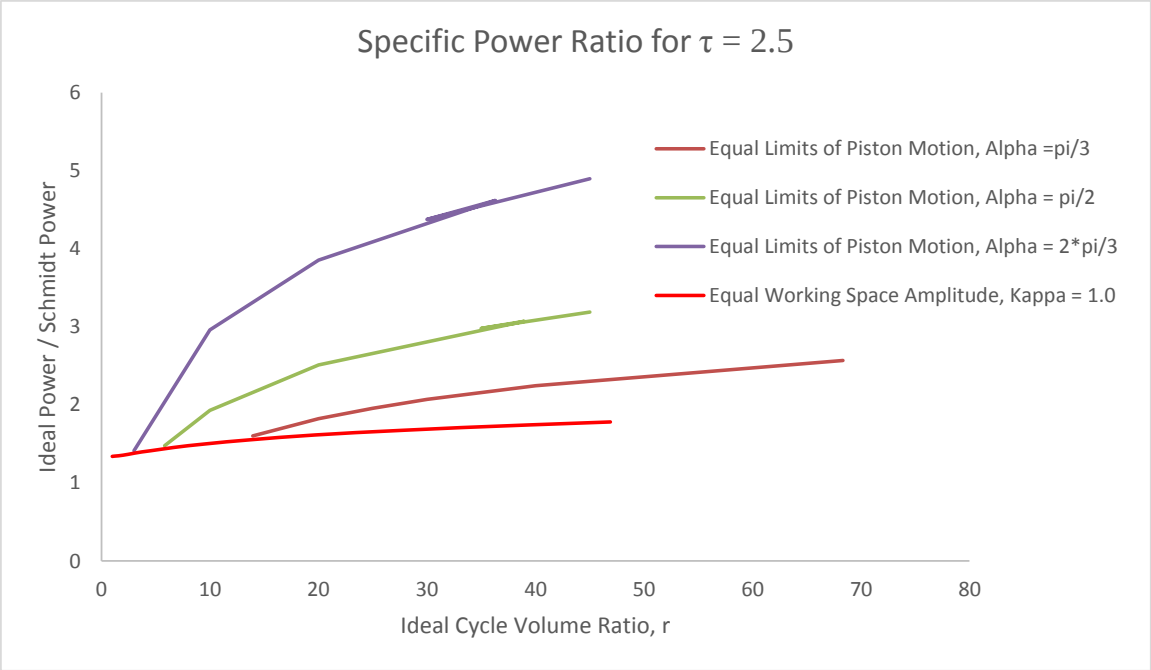

Figure 11 – Comparison of power density ratio for the cases of equal limits of piston motion and equal working space amplitudes

Figure 11 shows a minimum power density improvement of nearly 34% occurring for both sets of constraints. The power density ratio can be further increased in both cases by increasing the working space volume ratio. Increases in power density are more pronounced in cases when the ideal cycle is allowed to achieve higher working space volume ratios than the ideal cycle. In all cases increases in the working space volume ratio increases the power density according to ln r, until some practical limit is reached. The range of volume ratios shown in Figures 8-11 includes higher values than are typically seen in realistic Stirling engine operation because this analysis assumes zero dead volume. Cases that are more representative of real Stirling engine operation are considered in later analyses.

These two comparisons illustrate the differences in power density that result from approximating ideal piston motion with sinusoidal piston motion. The ideal cycle has

three advantages over the Schmidt cycle: 1) Constant volume heat addition/rejection in the ideal cycle increases the pressure ratio which increases power density: 2) Dwelling periods of the ideal cycle allow it to achieve larger working space strokes, even when operating within the same limits of piston motion as the sinusoidal cycle. 3) Dwelling pistons/displacer results in the minimum amount of hot gas being compressed and the minimum amount of cold gas being expanded. Using common working amplitudes for the ideal cycle and Schmidt cycle eliminates benefit number two, resulting in a power density improvement of at least 34% with larger increases possible depending on the operating conditions. Using common limits of piston motion, allowing the ideal cycle to achieve higher working space volume amplitudes than the Schmidt cycle allows the ideal cycle to take advantage of all three benefits. In this case the minimum predicted increase in power density is also 34% but the effect of increasing the working space volume ratio, r is more pronounced. In all of the cases analyzed in this section the efficiency of both the ideal and Schmidt cycles are equal to the Carnot efficiency due to the assumptions of isothermal gas spaces and perfect regeneration.

Isothermal Analysis - Ideal Motion vs. Sinusoidal Motion Engines with Dead Volume

The preceding analysis considers a general and highly idealized Stirling engine to illustrate the potential advantages of using piston motion that more closely approximates ideal piston motion. However, several of the assumptions used in the preceding section are unrealistic, calling into question the usefulness of the results. For example, the assumption of no dead volume allows the ideal cycle to achieve unrealistically high pressure ratios when the volume ratio is treated as an independent variable. Real Stirling

engines require large amounts of dead volume in the heat exchangers and regenerator to achieve the required heat transfer. This dead volume limits the pressure ratio and power density of the ideal cycle, but was neglected in the prior analysis.

In this section ideal Stirling analysis and Schmidt analysis are applied to a more realistic engine design, including dead volume. This analysis still assumes that the expansion and compression spaces are isothermal and that there are no loss mechanisms, and perfect regeneration; so it is still idealized, but it is used here to illustrate the potential benefits of ideal piston motion with dead volume included.

The engine chosen for analysis is a 1-kW free-piston engine in the beta-configuration. This engine is chosen because it has been on test at the Stirling Research Lab (SRL) at NASA GRC and is available for experimental validation testing, which is described in greater detail in the Experimental Testing section. Table I lists the relevant parameters for ideal and Schmidt analysis.

Table I - Parameters for a 1-kW engine

Parameter Name	Value	Units
Piston-Displacer Phase Angle	53.8	°
Piston Swept Volume	51.3	cm^3
Displacer Swept Volume	48.0	cm^3
Avg BS Volume	2000	cm^3
Avg CS Volume	104	cm^3
Avg ES Volume	140	cm^3
Cooler Volume	31.3	cm^3
Regenerator Volume	202	cm^3
Heater Volume	59.0	cm^3
Gas Mass	0.0101	kg
BS Temperature	350	K
CS Temperature	350	K
ES Temperature	779	K
Cooler Temperature	350	K

Heater Temperature	779	K
Gas Constant (Helium)	2077	J/kg-K

There are several different methods of comparing ideal and sinusoidal waveforms, which can lead to different conclusions. A decision must be made on how best to constrain the ideal piston motion to get useful comparisons with sinusoidal piston motion. Since the displacer in the beta-configuration has little effect on the working volume and real engines have dead volumes and clearance volumes, the choices of bounding constraints on the piston and displacer in the beta configuration differ from the constraints used on the compression and expansion pistons used during analysis of the ideal alpha-configuration. All of the cases studied below use common values for the maximum working volume and minimum expansion space volume which constrains the outmost positions of the piston and displacer to be common for both ideal and Schmidt cycles, guaranteeing that the engine does not have to increase in size to accommodate the prescribed motion.

One set of additional constraints is to force the ideal cycle and Schmidt cycle to share common values of minimum working volume and minimum compression space volume, forcing the ideal cycle to maintain a relatively large gas volume in the cold space throughout the cycle. This constraint forces the ideal piston and displacer to operate at lower amplitudes than the Schmidt piston and displacer. A less restrictive case is to allow the minimum compression space volume of the ideal cycle to approach zero during expansion allowing the ideal piston to travel further in than it does during the Schmidt cycle, resulting in a larger working space stroke. This constraint allows the ideal piston and/or displacer to travel further in than they do during the Schmidt cycle. Another

interesting set of constraints is to enforce common values for maximum and minimum expansion and compression space volumes, thus requiring the piston and displacer to have the same in *and* out limits of motion. Under this set of constraints the displacer must dwell at its inmost position rather than following the piston, as is typical in ideal Stirling analysis. This case does not represent truly ideal piston motion, but is included in the analysis as a case of interest. Table II shows the predicted ratio of ideal to Schmidt cycle power for the P2A engines at nominal operating conditions under these constraints. This analysis predicts a power density improvement between 50% and 315% depending on the method of constraint

Table II - Ideal vs. Schmidt cycle power for the 1-kW P2A convertors at nominal operating conditions.

Case	Constraints	Description / Notes	$\frac{W_{ideal}}{W_{Schmidt}}$
1	$V_{WS,max,ideal} = V_{WS,max,Schmidt}$ $V_{ES,min,ideal} = V_{ES,min,Schmidt}$ $V_{WS,min,ideal} = V_{WS,min,Schmidt}$ $V_{CS,min,ideal} = V_{CS,min,Schmidt}$	• Piston has same in and out limits • Displacer has same out limit • Same minimum clearance between piston and displacer. • Most restrictive case	1.5
2	$V_{WS,max,ideal} = V_{WS,max,Schmidt}$ $V_{ES,min,ideal} = V_{ES,min,Schmidt}$ $V_{WS,min,ideal} = V_{WS,min,Schmidt}$ $V_{ES,max,ideal} = V_{ES,max,Schmidt}$	• Piston has same in and out limits • Displacer has same in and out limits • Displacer dwells at in limit • Not truly an ideal Stirling motion	1.7
3	$V_{WS,max,ideal} = V_{WS,max,Schmidt}$ $V_{ES,min,ideal} = V_{ES,min,Schmidt}$ $V_{WS,min,ideal} = V_{WS,min,Schmidt}$ $V_{CS,min,ideal} = 0$	• Piston has same in and out limits • Displacer has same out limit • Displacer is allowed to travel further in than sinusoidal case	2.8
4	$V_{WS,max,ideal} = V_{WS,max,Schmidt}$ $V_{ES,min,ideal} = V_{ES,min,Schmidt}$ $V_{CS,min,ideal} = 0$ $V_{WS,min,ideal} = V_{ES,min,Schmidt}$	• Piston has same out limit • Displacer has same out limit • Piston travels inward until it meets the displacer	4.15

The power density of an engine in the beta-configuration achieves the same 3 power density benefits as the alpha configuration, by slightly different means:

1. The piston dwells as the displacer travels causing heat addition and removal to take place at constant volume increasing the pressure ratio.
2. The displacer dwells at its outmost position during compression, minimizing the gas inventory in the hot end. Similarly, it follows the piston during expansion, minimizing the amount of gas inventory in the compression space.
3. The ideal motion allows the piston and displacer to come arbitrarily close to each other without colliding, allowing the ideal cycle to achieve higher piston and displacer amplitudes than are achievable with sinusoidal motion.

Case 1 primarily takes advantage of constant volume heat addition and rejection, with some additional benefit coming from holding the compression space volume at the minimum during expansion and the expansion space volume at a minimum during compression, resulting in a 50% increase in power density. Case 2 achieves higher power density by reducing the gas inventory that remains stagnant in the compression space, which reduces the effective dead volume even though the piston and displacer have the same limits of motion as the Schmidt cycle. Case 2 is also interesting because it deviates slightly from ideal Stirling motion, but still achieves higher power density than the Schmidt cycle while achieving the Carnot efficiency. Ideal motion requires that the displacer and piston travel together during expansion in order to maximize the gas inventory in the expansion space. However, the constraint on the inmost limit on the displacer motion forces the displacer to dwell at its inmost position, preventing it from following the piston. The predicted power density increase for this case is 70%. Case 3 further increases power density by reducing the compression space volume to zero during expansion, eliminating the clearance volume in the compression space and increasing the

peak pressure, resulting in a 180% increase in power density. The analysis of Case 4 predicts a 315% improvement in power density due to an increase in the swept volume of the working space. Note that in all the above cases the predicted efficiencies of both the ideal Stirling and Schmidt analyses are equal to the Carnot efficiency because neither analysis takes into account non-isothermal gas volumes, irreversible processes, or imperfect regeneration. Figures 12 – 15 show P-V diagrams and a plot of their piston and displacer motion alongside the corresponding Schmidt cycle.

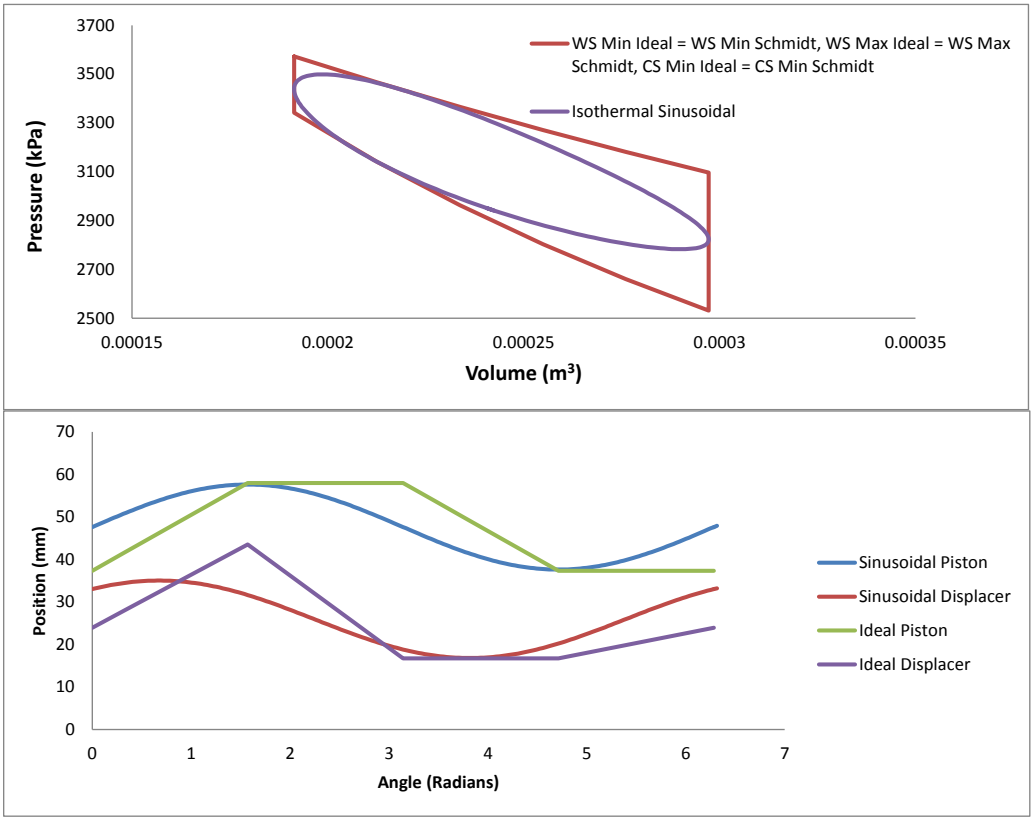

Figure 12 - Case 1 Piston and Displacer Motion and P-V Diagram

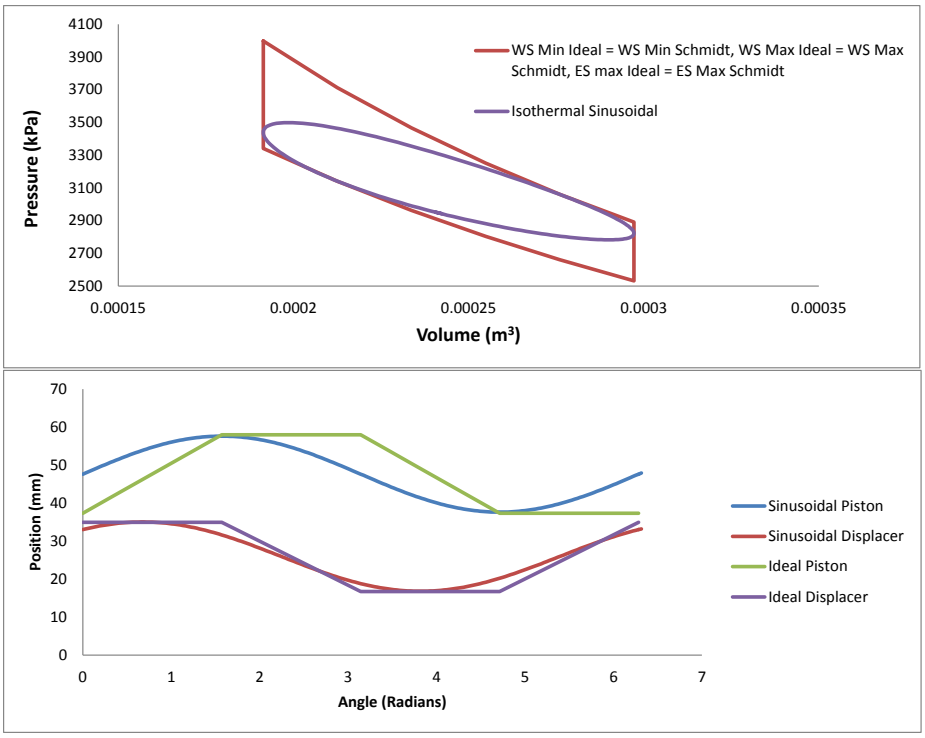

Figure 13 - Case 2 Piston and Displacer Motion and P-V Diagram

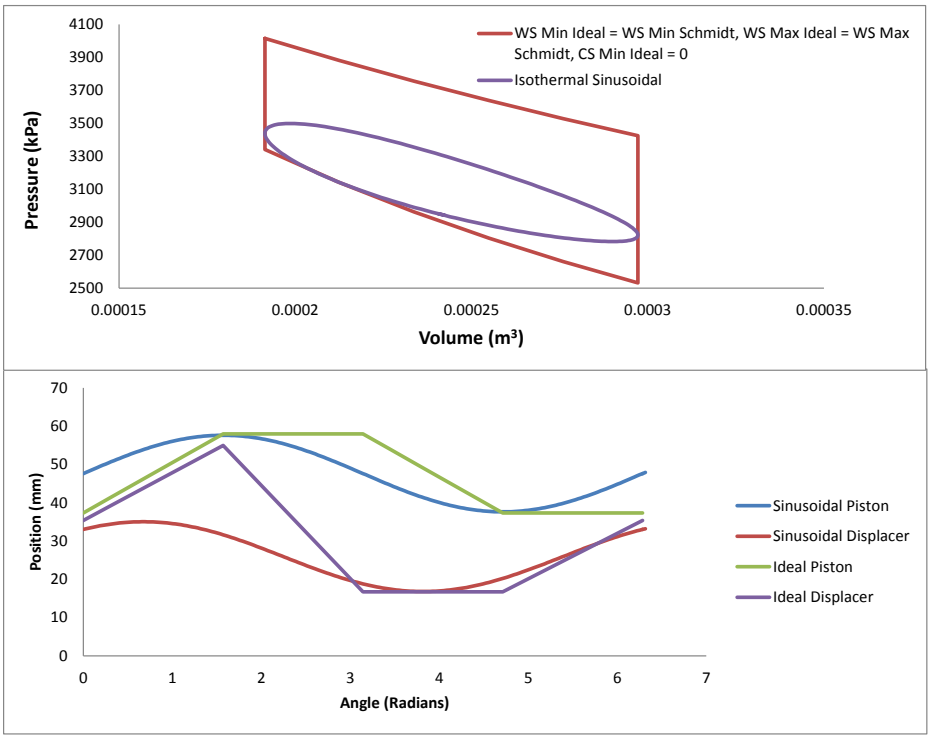

Figure 14 - Case 3 Piston Motion and P-V Diagram

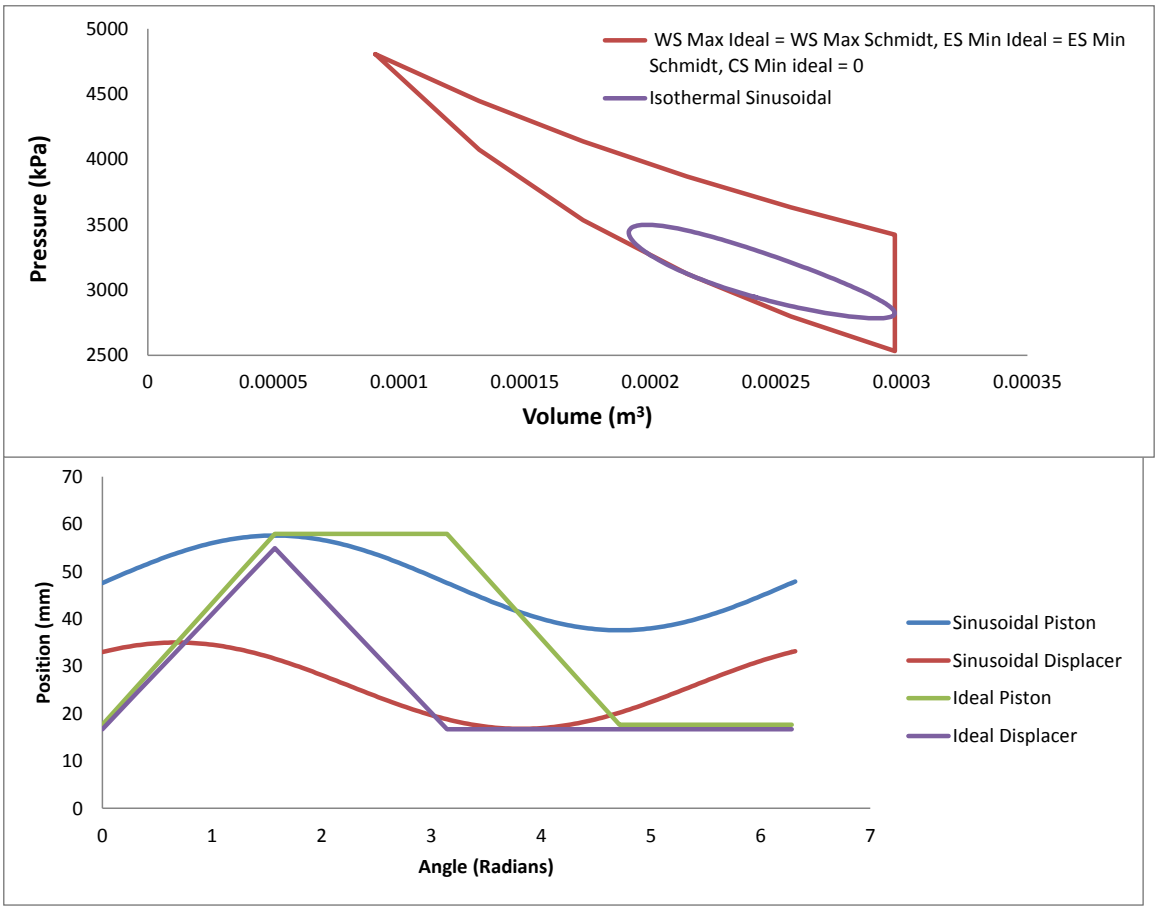

Figure 15 - Case 4 Piston Motion and PV Diagram

In thermodynamic analysis it is customary to include the temperature-entropy (T-S) diagram alongside the pressure-volume (P-V) diagram. In many thermodynamic cycles, such as the Otto and Diesel cycles, the entire working fluid mass is at approximately the same temperature and pressure at a given moment within the cycle, so the thermodynamic state of the entire working fluid is well defined. In many other cycles, such as the Brayton and Rankine cycles this is not true, but P-V and T-S diagrams can still be generated by following an individual element of fluid as it passes through the loop over one full cycle. In Stirling engines the pressure is assumed to be constant throughout the working volume, but when dead volume, clearance volume, or non-ideal motion is introduced, the different regions of the working volume are at different

temperatures. Furthermore, no single element of fluid passes through all of the engine components over a given cycle, so the typical methods used to generate T-S diagrams are not available to Stirling analysts. Therefore, most Stirling thermodynamic analyses do not include T-S diagrams unless they are considering highly idealized engines with no dead volume in which the entire working gas inventory is at either the expansion space or compression space temperature at a given point in the cycle.[1] For the purpose of this analysis the T-S diagram will remain omitted since it is not necessary to illustrate the effect of ideal motion on power density or efficiency.

The isothermal analysis presented above shows the potential improvement in power density for a realistic engine design operating under highly idealistic assumptions with ideal piston and displacer motion. Predicted increases in power density range from 50% - 315%, depending on the restrictiveness of the constraints used in the analysis. Isothermal analysis is a useful tool for making rough predictions about engine power output with an easily understandable closed form solution. However, isothermal analysis (assuming perfect regeneration) predicts cycle efficiency equal to the Carnot efficiency for both ideal and sinusoidal motion in all cases. This is an indication that isothermal analysis is too highly idealized and that predictions should be met with some skepticism. More sophisticated techniques are used in the following sections to more accurately predict both power density and efficiency of the 1-kW P2A engines.

[1] Since the thermodynamic state of any system is completely determined by any two of its thermodynamic variables, in theory, one can produce an "Effective T-S diagram" for the working space in which the entropy and "effective temperature" are calculated based on the pressure and volume of the working space, which are both well-defined. Since this concept is not directly relevant to the current study it is not explored further, but remains a point of interest for future work.

Numerical Analysis - Sage Stirling analysis software

Isothermal analysis assumes that heat transfer rates in the expansion and compression spaces are so high that the temperature of the gas within those volumes can be considered isothermal. Under these conditions there is no need for a heater or cooler, because all of the necessary heat transfer takes place in the expansion and compression spaces. Real engines lack sufficient surface area in the compression and expansion spaces to accomplish this, so high surface area heaters/acceptors and coolers/rejectors are added along with their associated dead volume. Figure 16 shows a schematic of a more accurate engine model. Adiabatic analysis is typically considered the next step in accuracy beyond isothermal analysis, especially in regards to engine efficiency. Adiabatic analysis assumes that the expansion and compression spaces are adiabatic and that the heater and cooler are isothermal.

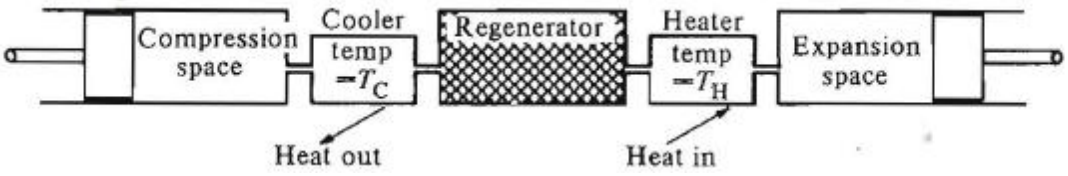

Figure 16 - Conceptual layout of an adiabatic Stirling convertor [24]

(Reprinted with permission from Oxford University Press)

Adiabatic Stirling analysis is a more accurate predictor of engine power output and efficiency than isothermal analysis, but requires an iterative numerical solution. Adiabatic analysis is still an oversimplification, because the expansion, compression, heating, and cooling processes are neither isothermal nor adiabatic, but lie somewhere in between and are governed by heat exchanger design of an individual engine. In addition, adiabatic analysis does not take into account several potentially substantial loss

mechanisms including pressure drop through the heat exchangers, leakage between gas volumes, and direct conduction from the hot-end to the cold-end through the cylinder. By not taking into account loss mechanisms, the displacer (in both isothermal and adiabatic analyses) acts as a forced mass spring system with no damping and therefore no loss mechanisms, so the work required to achieve ideal displacer motion is zero and the cycle work is equal to the work done by the piston. In reality, pressure drop and leakage create damping forces on the displacer which must be compensated for through P-V work on the displacer or work done by an external displacer forcing function. In either case, the power required to drive the displacer reduces the net power output of the engine, and is not taken into account in adiabatic or isothermal analyses, so they both produce optimistic predictions of power density and efficiency.

Improving model accuracy beyond what is achievable with adiabatic analysis requires nodal analysis and knowledge of the detailed engine design, including heat exchanger geometry, regenerator specifications, cylinder geometry, seal geometry, etc. One such nodal analysis tool is a commercially available program called Sage [27]. Sage is commonly used for Stirling engine optimization in the design phase. The Sage model of the1-kW engines is a nodal, one-dimensional, cyclic steady-state model that couples the equations of motion of the piston and displacer with the Navier-Stokes equations, and energy equations. Sage can also be used to calculate the reduction in available energy which is ignored by ideal, isothermal, and adiabatic analysis.

The Sage model of the 1-kW engines assumes an isothermal boundary condition on solid surface node within the engine, it then calculates temperature gradients in the rest of the solid and the gas based on solid conduction and calculated convection

coefficients. The axial temperature distribution along the base of the finned exchangers (acceptor and rejector) are set as an input. These temperature inputs typically come from heat transfer analysis done outside of Sage. Sage then iteratively solves for gas temperatures and pressure drops by guessing and checking fin temperature profiles and gas velocities, and the resulting displacer motion (piston motion is typically a user input). Figure 17 shows a P-V diagram generated by Sage for the 1-kW engines described in the Experimental Testing section. The P-V diagram generated from isothermal sinusoidal analysis is included for reference.

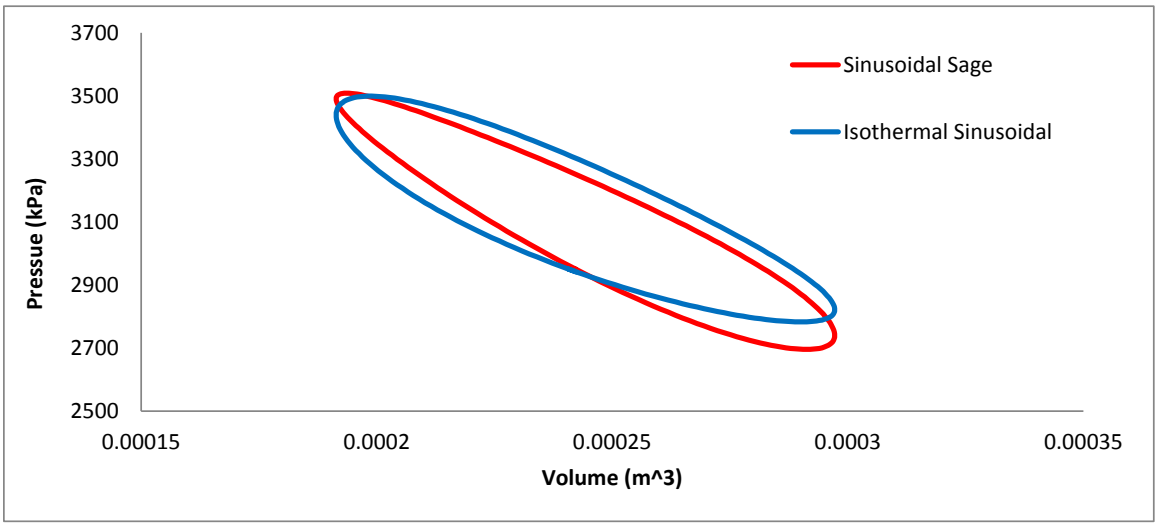

Figure 17 - P-V Diagram for the 1-kW P2A engines with isothermal and ideal P-V diagrams plotted for reference

The predicted power output for isothermal analysis is 36% larger than the Sage predicted power output. Isothermal analysis predicts an engine efficiency equal to the Carnot efficiency, which in this case is 0.550 (T_h = 779 and T_c = 350) which is 80% higher than the efficiency of 0.307 predicted by Sage, suggesting that isothermal analysis does a relatively poor job of predicting the heat transfer requirements in real engines.

Sage requires all non-sinusoidal time dependent inputs to be entered as sums of harmonic sinusoids. As higher harmonics are added, the solver time step must be reduced to resolve the higher frequencies, increasing computational time. Ideal piston and displacer motion was approximated using 7-term truncated Fourier series. Figure 18 shows an example of ideal piston motion plotted alongside sinusoidal motion, and the 7-term Fourier approximation. There is some overshoot (ringing) associated with using truncated Fourier series, but this effect was usually small since the quality of fit was high in all cases (R^2 values for all cases run were above 0.995).

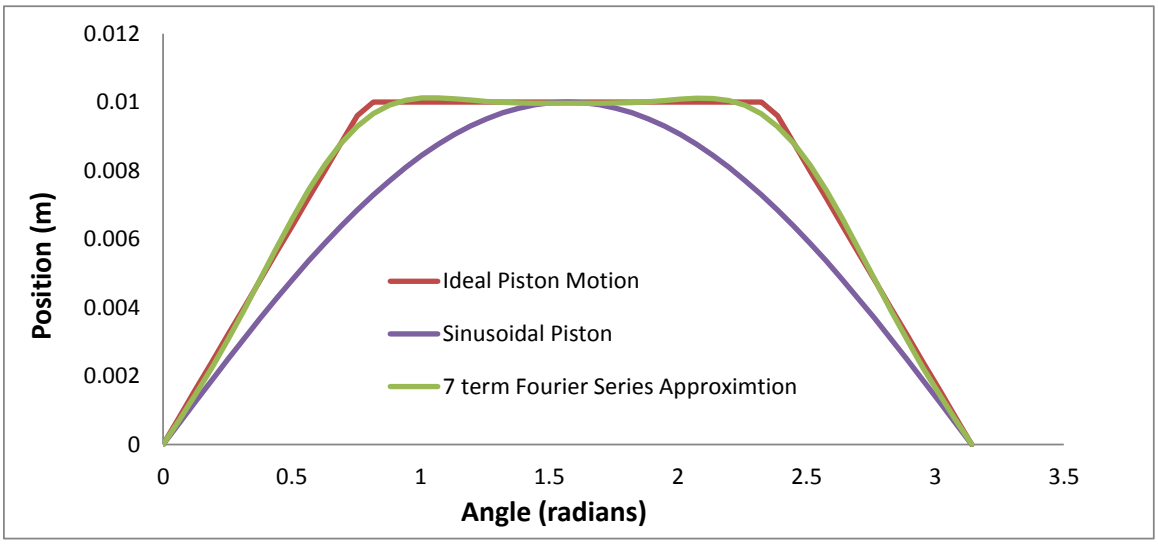

Figure 18 - Comparison of ideal piston motion with a single-term sinusoidal approximation and a 7-term Fourier Series approximation

One inherent problem in modeling ideal piston and displacer motion in Sage, or any other high fidelity Stirling model, is that there are in infinite combination of piston and displacer motions which are considered ideal. Figure 19 shows four different piston motions with varying piston dwell times, all of which satisfy the requirements of ideal piston and displacer motion.

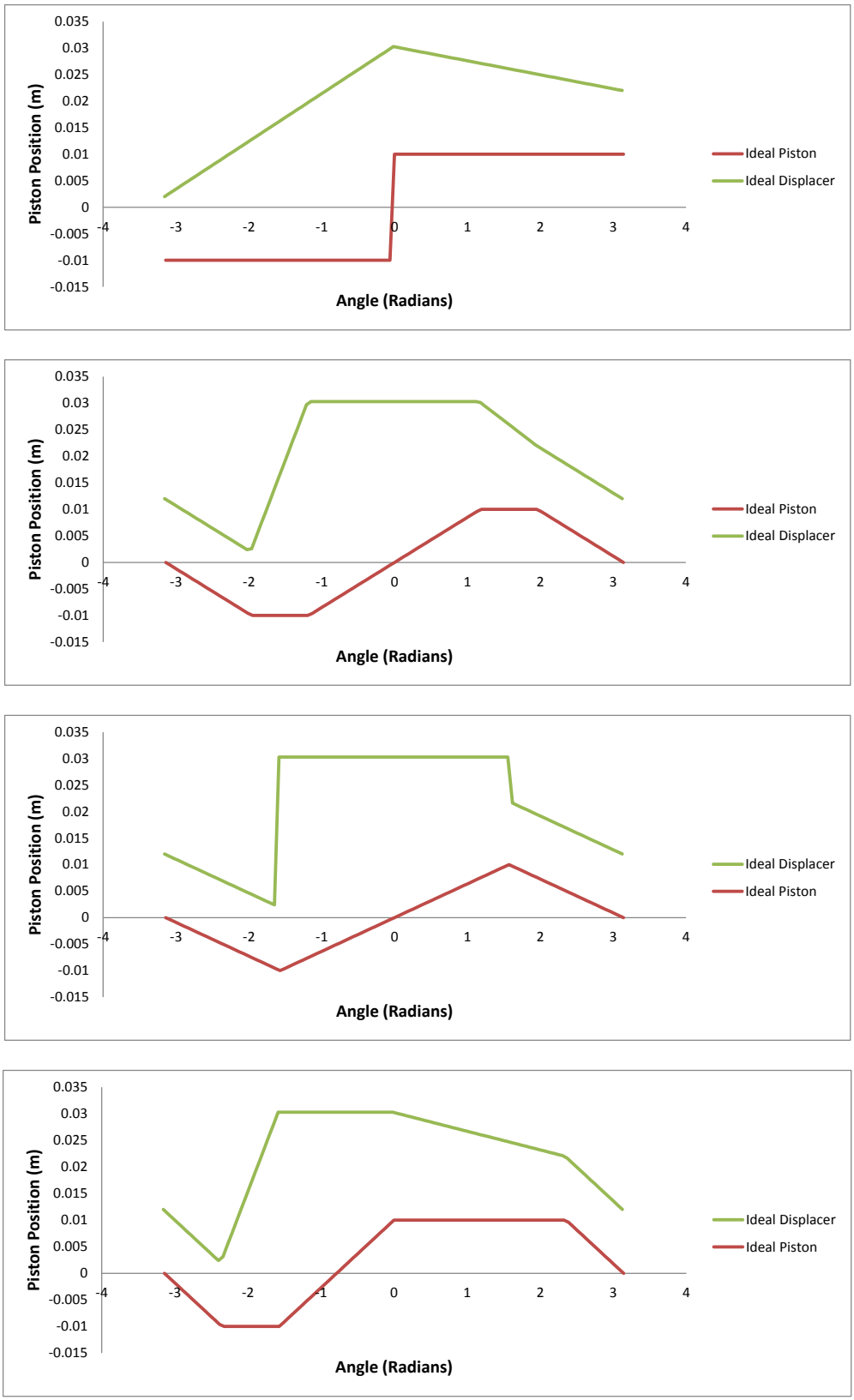

Figure 19 - Comparison of four ideal Stirling waveforms

The top graph shows an extreme case of symmetric piston motion with long piston dwell times and infinite piston velocities. The second graph shows a cycle with symmetric piston motion, moderate dwell times, and moderate piston velocities. The third graph shows another extreme case of symmetric piston motion with piston dwell times of zero and the lowest possible piston velocities. The bottom picture shows a case of asymmetric piston motion with moderate dwell times and moderate piston velocities. Each example of ideal motion presented in Figure 19 takes place under Case 1 constraints, namely ideal motion is constrained to have the same minimum expansion volume, minimum clearance between the piston and displacer, maximum working space volume, and minimum working space volume as the same engine operating with sinusoidal piston and displacer motion. This set of constraints was determined to be the most restrictive set of constraints using isothermal analysis. In addition to the waveforms shown in Figure 19 others can be generated using the constraints listed in Table II and even more can be generated if ideal displacer and piston velocities are not forced to be piecewise-constant, as they have been shown to this point. Since isothermal analysis assumes that heat transfer takes place instantaneously and does not take into account pressure drop or other loss mechanisms that are functions of piston and displacer velocity, predicted power output is equal for all ideal waveforms and the efficiency each of these waveforms are equal to the Carnot efficiency, regardless of dwell times or piston/displacer velocities. However, higher fidelity tools such as Sage consider the effect of insufficient dwell times on gas temperatures and higher mass flow rates on pressure drop through the regenerator and heat exchangers, so different versions of the ideal waveform have different power output and efficiency.

In order to keep computational times reasonable, no more than 7-terms were used to approximate ideal piston and displacer motion. Figure 20 shows the 7-term Fourier series approximation of the four ideal motions described in Figure 19.

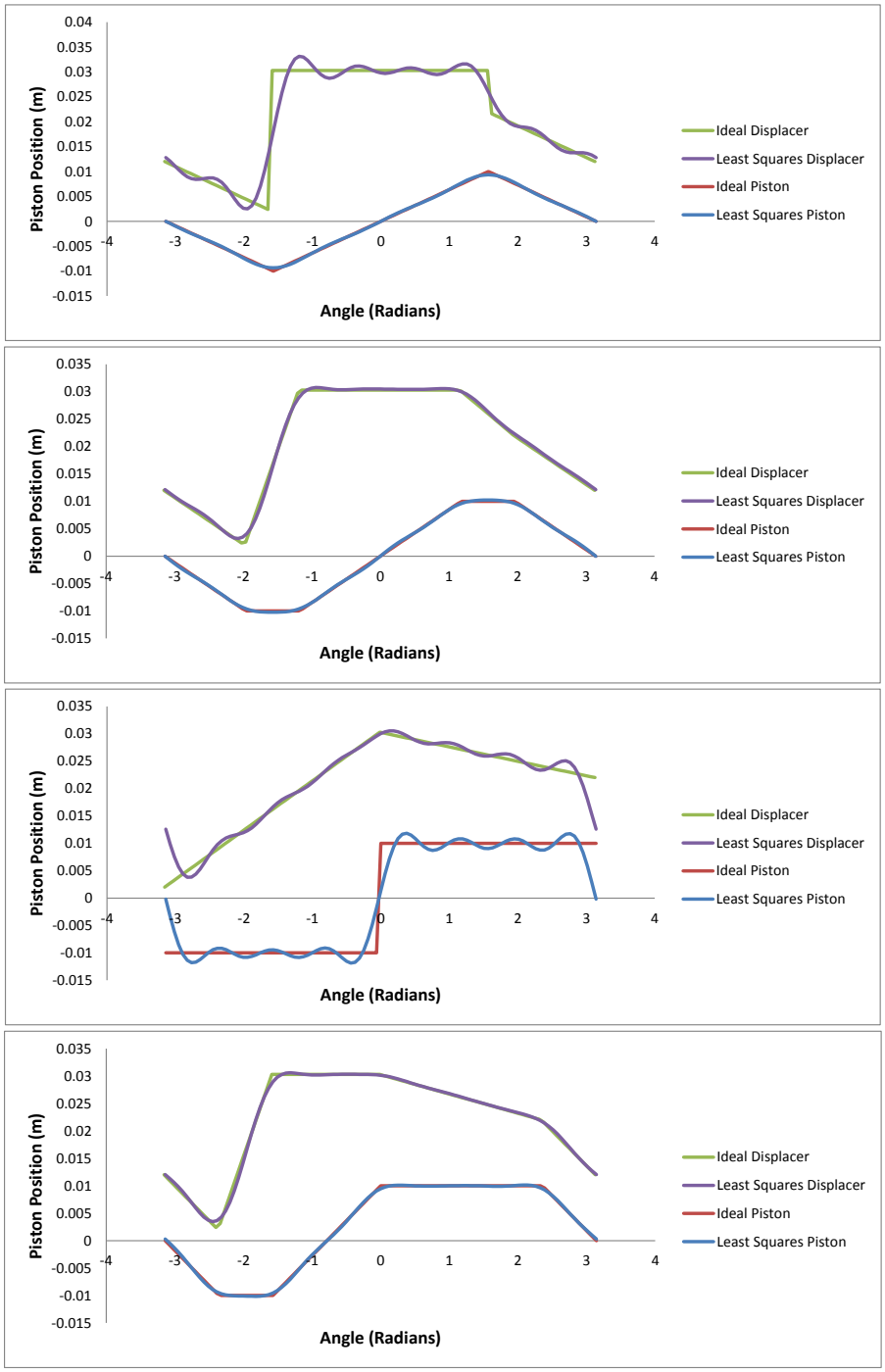

Figure 20 - Ideal piston and displacer motion with a 7-term least squares sine/cosine series approximation of ideal motion

For the extreme cases that require infinite piston or displacer velocities, 7-term approximations are relatively poor, typically achieving R^2 values for displacer motion no larger than 0.94. In cases with moderate piston velocities and dwell times typical R^2 values are on the order of 0.999. A minimum R^2 value of 0.995 was arbitrarily selected as the cut-off point for adequate approximation in subsequent analysis; the most extreme cases are not analyzed.

Nodal Analysis – Comparing Sinusoidal Motion, Ideal Motion, and Optimized Motion with Realistic Engine Geometry

For both ideal piston motion and the optimized piston motion examined in this section the piston and displacer are both forced to achieve the desired waveform. In reality, most free-piston Stirling engines have a free displacer attached to a linear spring which resonates at the convertor operating frequency. These engines have no mechanism to impose a non-sinusoidal waveform on the displacer. However, kinematic Stirling engines and some low TRL free-piston designs do have mechanisms to impose non-sinusoidal displacer waveforms. The analysis in this section is intended to show the possible performance benefits of altering piston and displacer motion in engines designed with capability to do so. Engines operating with non-sinusoidal piston and displacer motion are compared to an engine operating with a sinusoidal piston and a free displacer. The performance benefits of altering piston motion alone will be addressed separately.

Ideal piston and displacer motion result in maximum power density and efficiency in *ideal* Stirling engines. In *real* engines increased piston and displacer velocities inherent to ideal waveforms can adversely affect engine performance by increasing pressure drop through heat exchangers and/or adversely affecting heat transfer. The

following analysis shows that the optimal piston and displacer motions are not necessarily a close approximation of ideal motion, and typically lie somewhere in between the ideal and sinusoidal waveforms.

Analysis of Ideal Waveforms under Case 1 Constraints

Analysis of ideal waveforms in this section, are done under Case 1 constraints. Case 1 constraints set the maximum and minimum working volume, minimum expansion volume, and minimum compression volume to the same values as sinusoidal motion, which are the most limiting set of constraints for ideal piston motion. These constraints limit the inward travel of the piston and displacer leaving a stagnant gas volume in the compression space and limiting the working space stroke. Isothermal analysis predicts that under these constraints the power density of an engine operating with ideal piston and displacer motion is 50% higher than the same engine operating with sinusoidal piston and displacer motion, with no change in efficiency. Sage-based nodal analysis of ideal motion under these constraints is more pessimistic, predicting *lower* power density and efficiency than predicted for sinusoidal motion in most cases. Optimized piston and displacer motion results in increased power density at lower efficiency.

The isothermal analysis shown in previous sections uses the working space P-V diagram to show the increase in power density that results from ideal piston motion. This is useful when pressure drop is not considered so no work is required to drive the displacer and the working space P-V work is equal to the cycle work. Since nodal analysis takes into account pressure drop through the heat exchangers and the displacer is not simply resonating at the operating frequency the displacer work requirement is non-zero and must be accounted for. Instead of using the working space P-V diagram, which

would only account for piston work, a combination of instantaneous power and force-displacement (F-D) diagrams for both the piston and displacer are used to show the effect of ideal piston and displacer motion on performance.

Figure 21 shows motion, instantaneous power, and F-D diagrams for both the piston and displacer for Case 1 constraints with symmetric piston dwell times of $\pi/4$ radians. This motion results in 1680 W of piston power, compared to 1320 W for sinusoidal motion. However, short piston dwell times result in high displacer velocities during the cooling phase causing large pressure drops in the heat exchangers and large damping forces on the displacer. The result is 1630 W of power required to drive the displacer motion. The increased displacer power not only negates the increase in piston power output, but it nearly negates all of the work done by the piston, so the predicted net power of the engine is low (50 watts) compared to 1170 watts predicted for sinusoidal motion. The engine operating under these conditions produces little more than entropy.

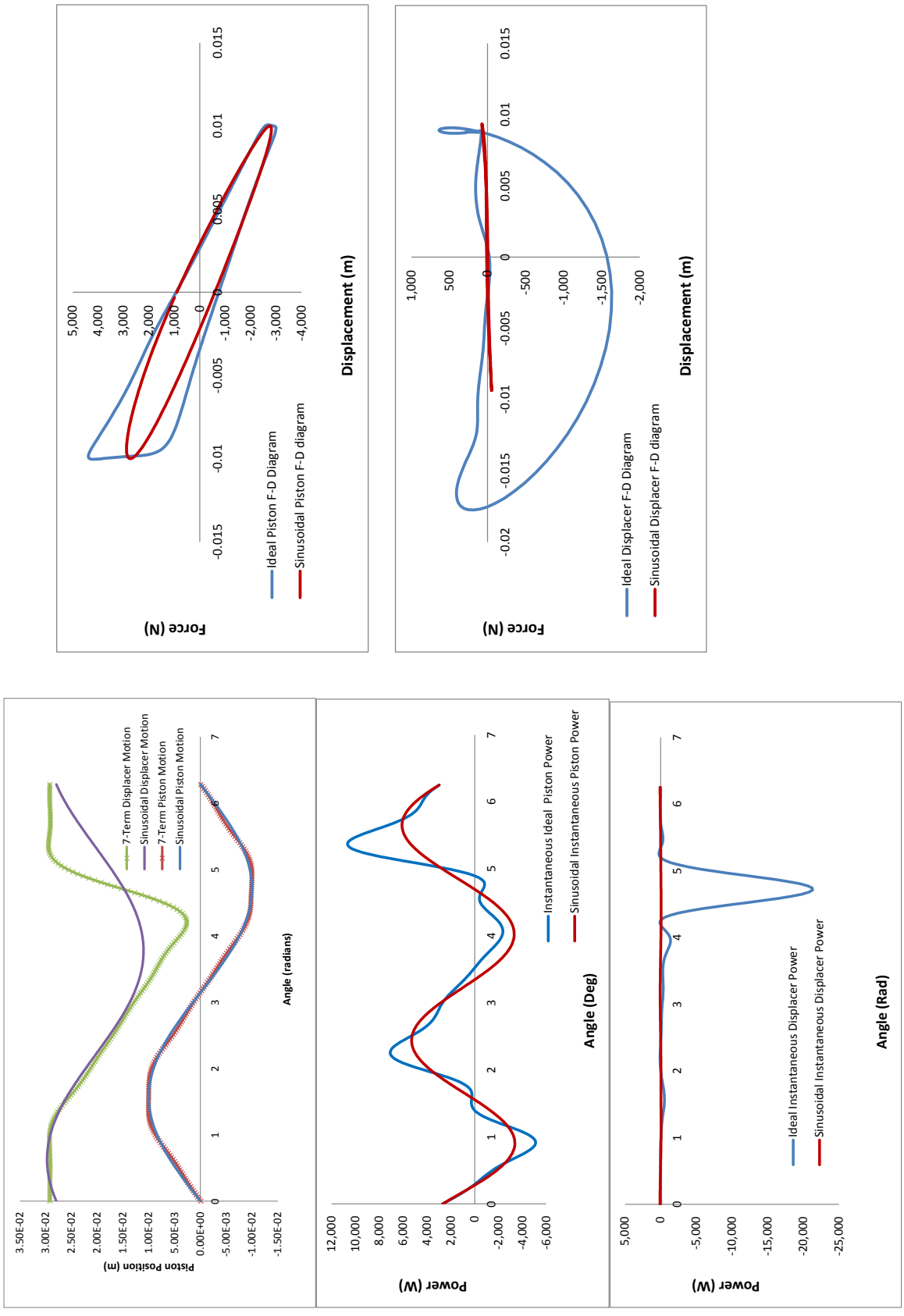

Figure 21 - Piston/Displacer motion, cumulative work, and F-D diagrams for Case 1 with short piston dwells

The displacer instantaneous power and F-D diagrams illustrate the profound negative effect of high displacer velocities, showing a substantial increase in the displacer work requirement during cooling as the displacer goes from its most negative position to its most positive. In this case the large displacer velocity causes pressure drop across the displacer to be orders of magnitude higher than the pressure drop resulting from sinusoidal motion, resulting in large viscous losses. Under Case 1 constraints the displacer is allowed to travel further inward than corresponding sinusoidal motion, but the large amount of viscous dissipation that occurs during this additional travel negates the potential advantage of maintaining minimum gas inventory in the compression space during expansion.

Figure 22 shows motion, instantaneous power, and F-D diagrams for both the piston and displacer for Case 1 constraints with symmetric piston dwell times of $\pi/2$ radians. Lengthening the dwell time reduces the displacer velocity and pressure drop during cooling from those seen in the short dwell case, but they are still higher than the sinusoidal case. In the medium dwell case the piston power was 1580 W with 760 W of power required to drive the displacer, resulting in a net power of 820 W at an efficiency of 16.5%. These are both improvements over the short dwell case, but they offer no advantage over the sinusoidal case which predicted a net power output of 1170 W at an efficiency of 30.7%.

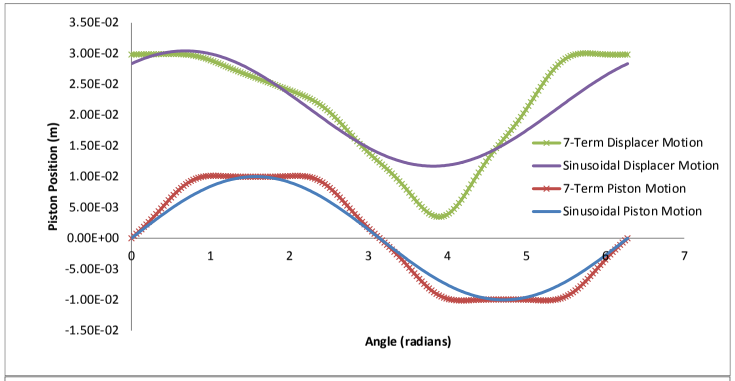

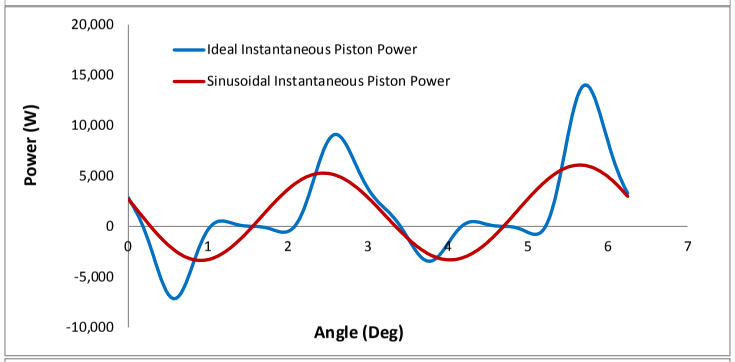

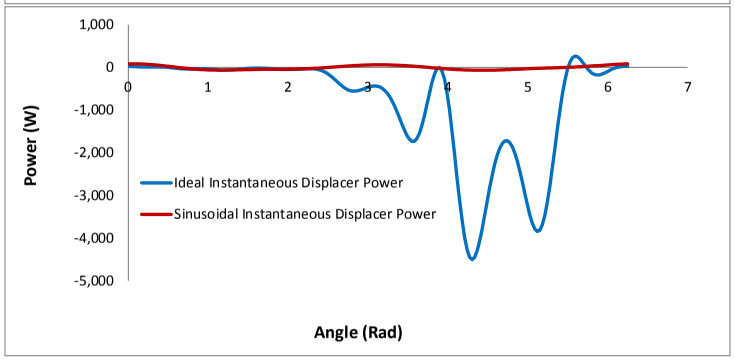

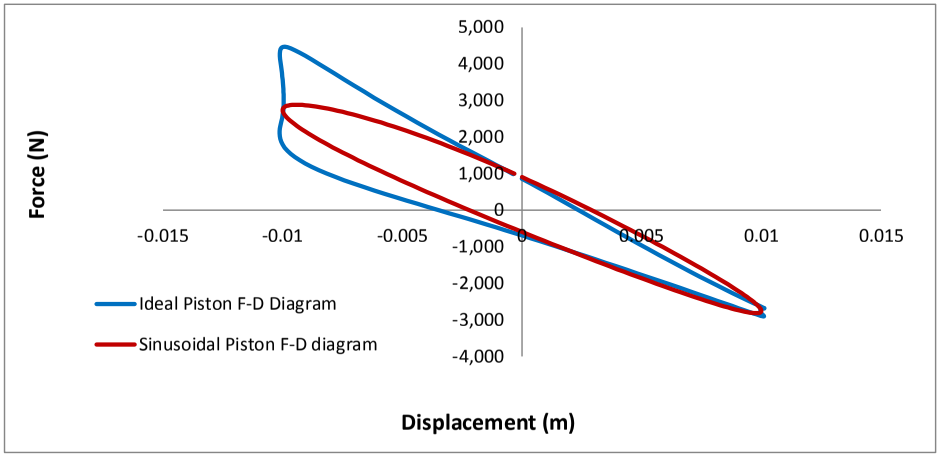

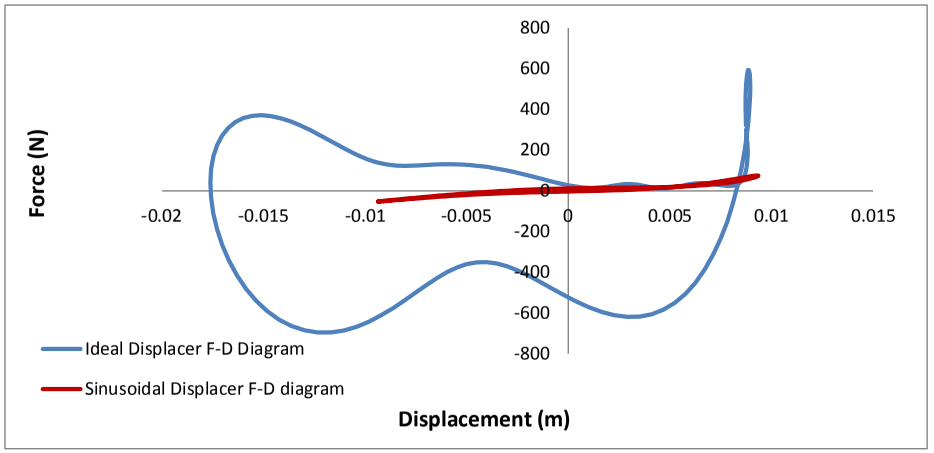

Figure 22 - Piston/Displacer motion and instantaneous work for Case 1 with medium piston dwell times

Figure 23 shows motion, instantaneous power, and F-D diagrams for both the piston and displacer for Case 1 constraints with symmetric piston dwell times of $3\pi/4$ radians. Increasing dwell times further decreases displacer drag but increases piston velocity and piston drag, resulting in 1320 W of piston power, a relatively small improvement over the 1170 W predicted for sinusoidal motion. Lower displacer velocities in the long dwell case reduce the displacer power requirement to 690 W, which is lower than the short and medium dwell cases, but still high enough to reduce the net power output to 630 W at an efficiency of 12.7%, offering no improvement over sinusoidal motion.

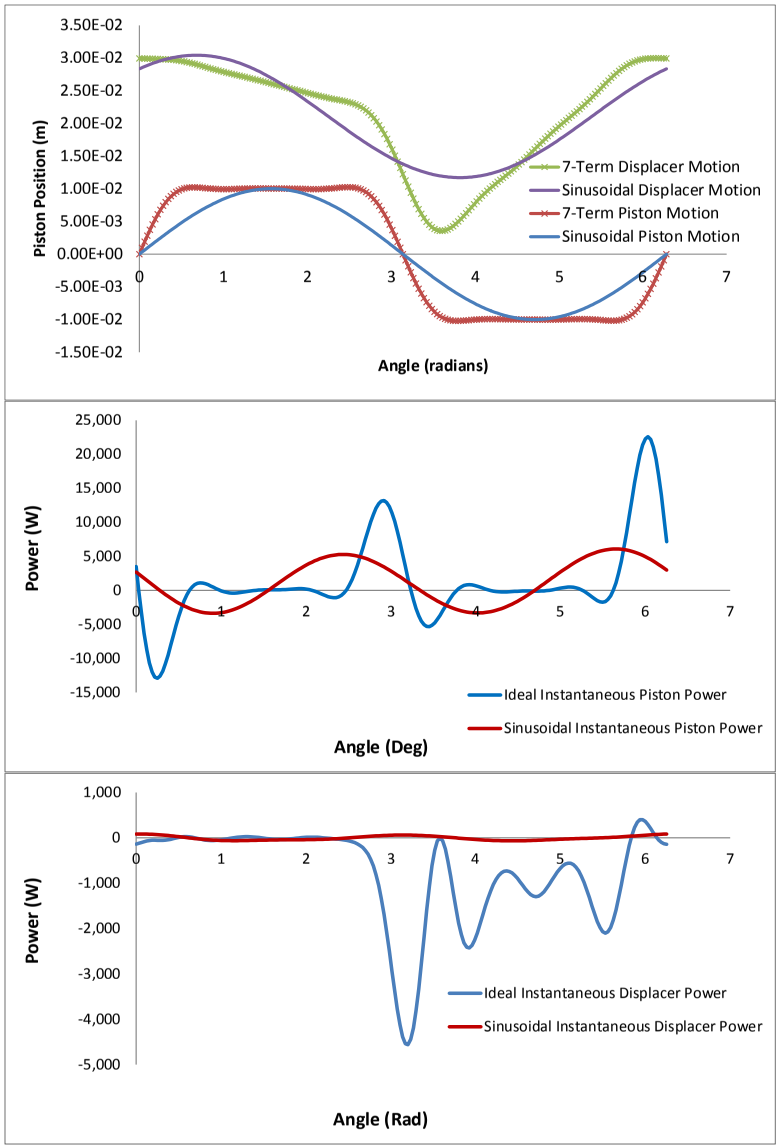

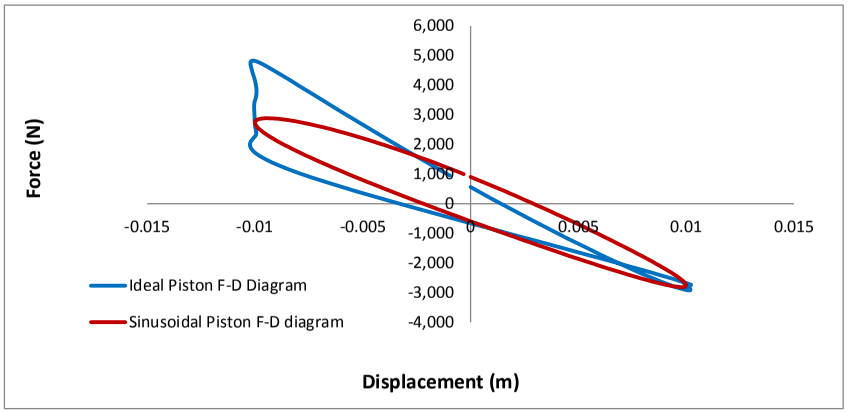

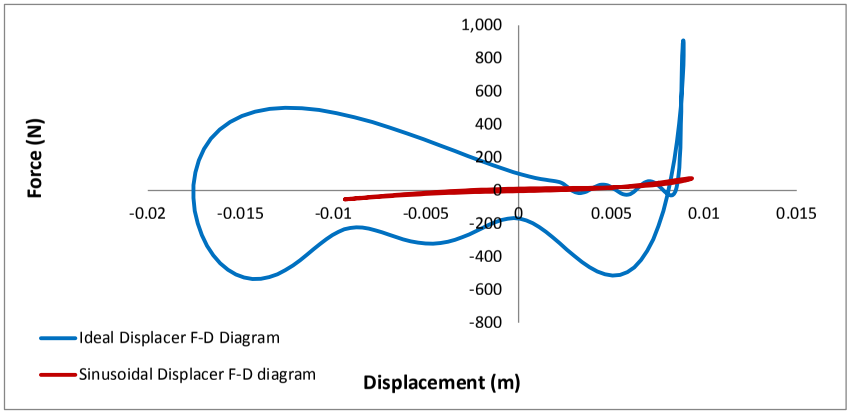

Figure 23 - Piston/Displacer motion and instantaneous work for Case 1 with long piston dwell times

Regardless of dwell time, symmetric ideal waveforms operating under the constraints of Case 1 produce less power and are less efficient than an engine operating with sinusoidal piston with a free displacer motion. This is due to the increased viscous dissipation in the regenerator and heat exchangers incurred by increasing piston and/or displacer velocity. The medium dwell case is the best of the three cases examined but it offers no improvement over sinusoidal motion. This is a coarse analysis of the dependence of engine performance on piston dwell time, and it is likely that the optimum dwell time lies between the points chosen for analysis above, but since the three cases examined above are far from improving on sinusoidal motion, no attempt is made to find the true optimum.

Removing the symmetry constraint on ideal waveforms allows the piston and displacer to achieve ideal motion with lower velocities, allowing for improved engine performance. Figure 24 shows motion, instantaneous power and F-D diagrams for both the piston and displacer for Case 1 constraints with asymmetric piston dwell times. Dwell times for this analysis are selected using an optimization routine to minimize the greater of the piston and displacer RMS velocities, in an effort to minimize pressure drop. In this scenario the piston power is 1580 W with a displacer power requirement of 430 W resulting in a net power output of 1150 W at an efficiency of 21.8%. This provides no increase in power density over the sinusoidal case and reduces efficiency. The long piston dwell and asymmetry makes it difficult to create smooth waveforms using a 7-term approximation. It is possible that higher order approximations could improve results, but is unlikely that these improvements would offer substantial benefits over sinusoidal motion.

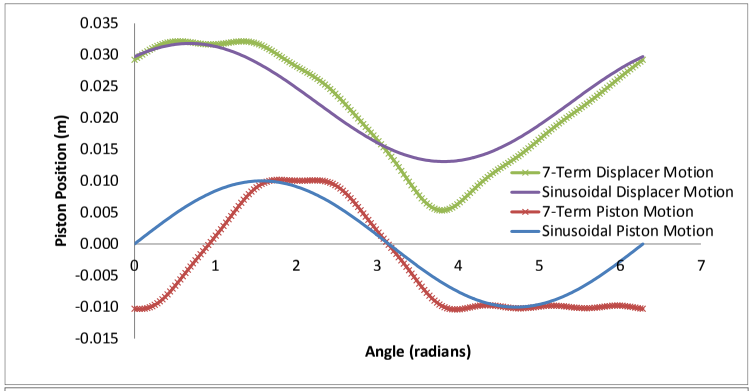

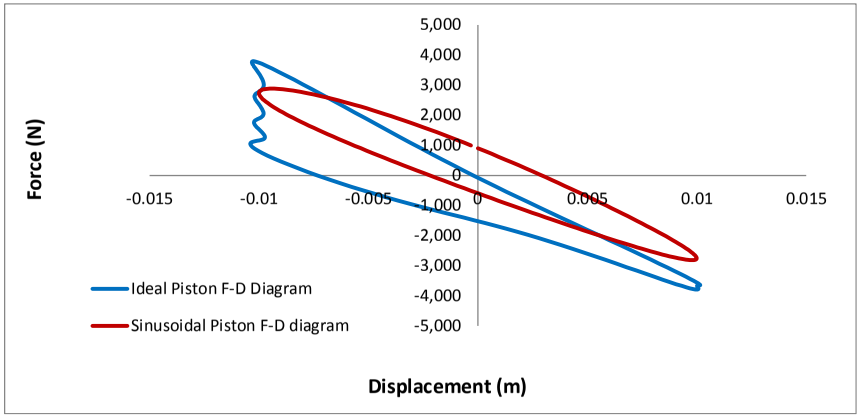

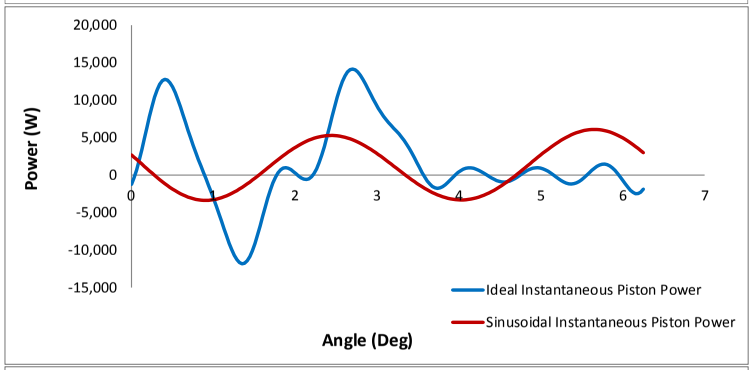

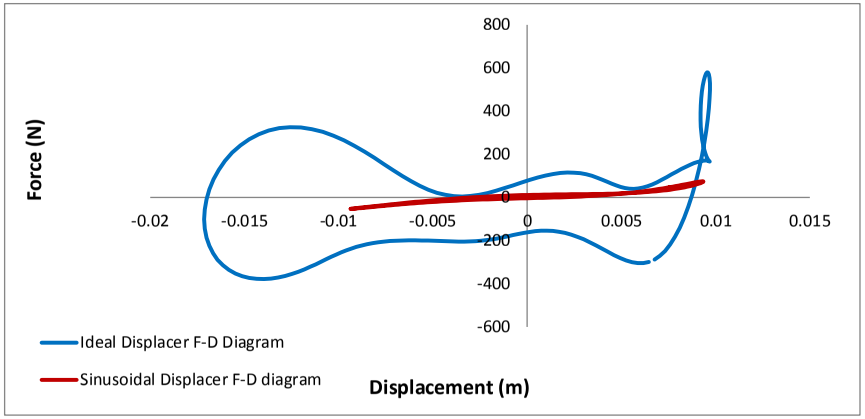

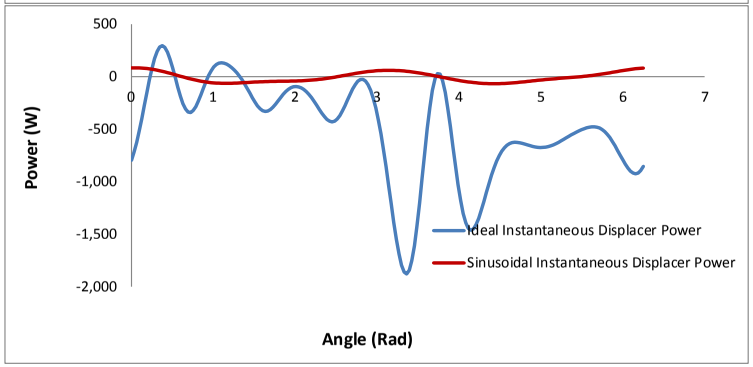

Figure 24 - Piston/Displacer motion, power, and F-D diagrams for Case 1 with asymmetric piston dwell times

Optimized Waveforms under Case 1 Constraints

It may seem discouraging that, at least for Case 1 constraints, there is no benefit to achieving ideal motion for this engine design. However, seeing that ideal motion results in increased piston power in all cases suggests that there may exist some optimal motion that takes advantage of the increased piston power without incurring large penalties due to increased viscous losses through the regenerator and heat exchangers. Determining this optimum motion requires the use of non-linear constrained optimization. This is achieved using the *fmincon* function in Matlab, using net power, as predicted by Sage, as the objective function and non-linear constraints defined by Case 1. Independent variables passed to the solver include all seven piston amplitudes, six piston phase angles (the phase angle of the fundamental frequency was pinned to zero), all seven displacer amplitudes, and all seven displacer phase angles for a total of 27 independent variables. Using single term sinusoidal motion as starting point, optimization requires hundreds of iterations and thousands of function evaluations. Each function evaluation requires a converged Sage solution, making the optimization a computationally intensive process.

Figure 25 shows motion, instantaneous power, and F-D diagrams for the piston and displacer for optimized motion under Case 1 constraints. Figure 26 shows the optimal motion as a compromise between ideal motion and sinusoidal motion, using asymmetric dwell times on the piston to take advantage of increased power and minimizing piston and displacer losses as much as possible by keeping velocities moderate. Optimal motion results in 1580 W of piston power and a displacer power requirement of 150W, resulting in an increase in net power from 1170W for sinusoidal

motion to 1430 W for optimized motion. The efficiency decreases from 30.7% for sinusoidal motion to 27.9% for optimized motion. Optimized piston and displacer motion under Case 1 constraints can offer system level benefits in applications that favor power density over efficiency.

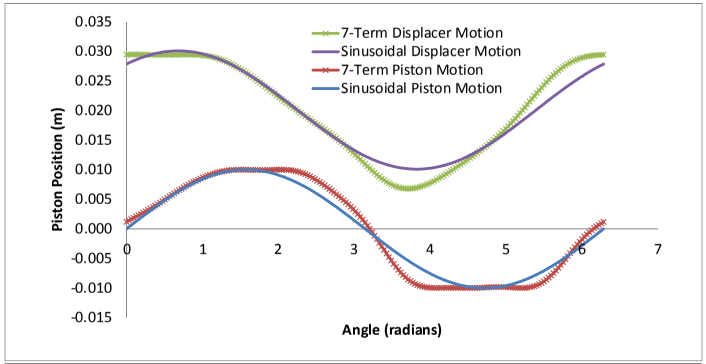

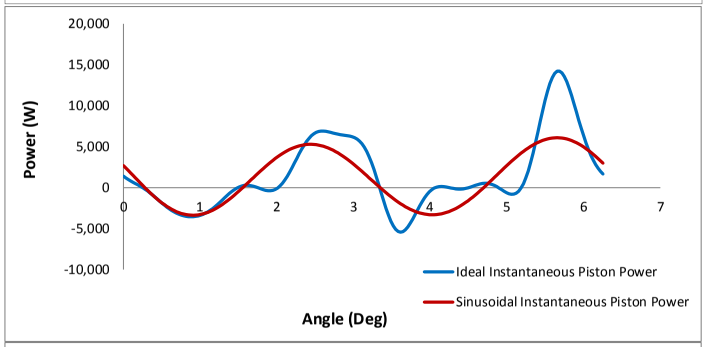

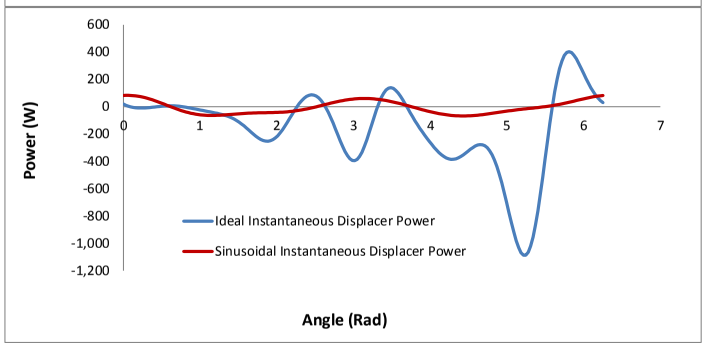

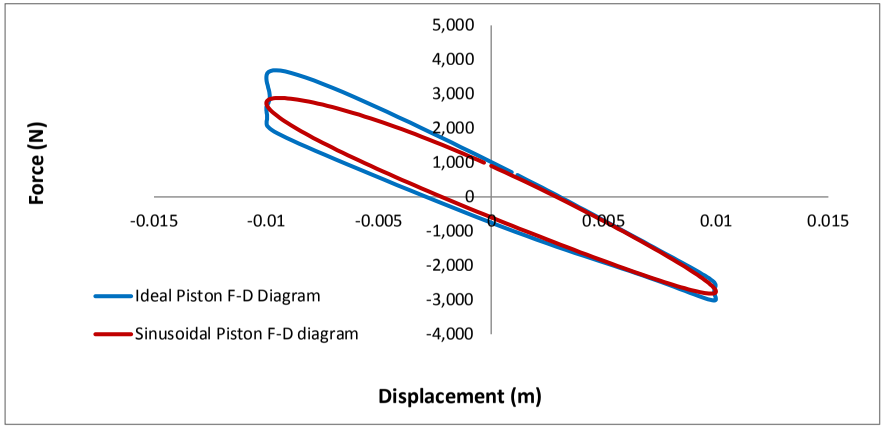

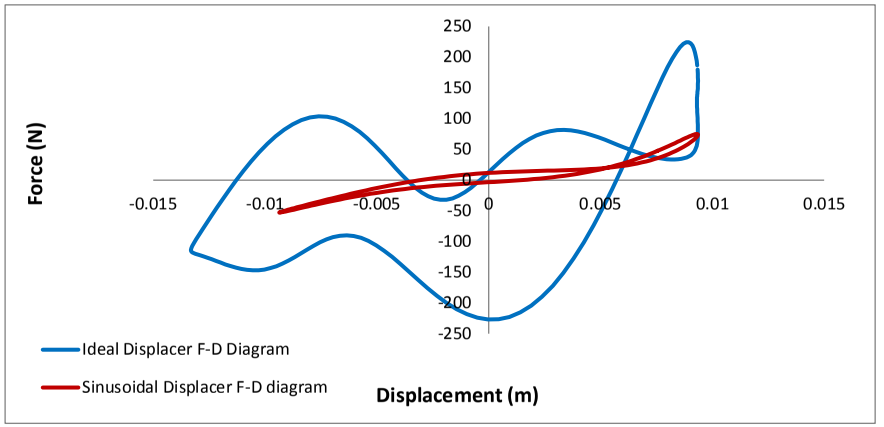

Figure 25 - Piston/Displacer motion, power, and F-D diagrams for optimized Case 1 motion

Sage analysis shows that ideal piston motion reduces engine performance regardless of the choice of dwell times or symmetry of the ideal waveform. Three symmetric waveforms of varying dwell times and an asymmetric waveform optimized to reduce piston and displacer RMS velocity are studied. Although piston power output increases by as much as 44%, the predicted net power output and efficiency in all cases are less than the power output predicted for sinusoidal motion. Non-linear constrained optimization is used to determine piston and displacer waveforms that maximize power density. The optimal displacer waveform is a compromise between sinusoidal and ideal motion, displacing a larger gas volume than sinusoidal motion without incurring the high viscous losses of ideal motion. The difference between sinusoidal, ideal, and optimal power density motion is illustrated in Figure 26.

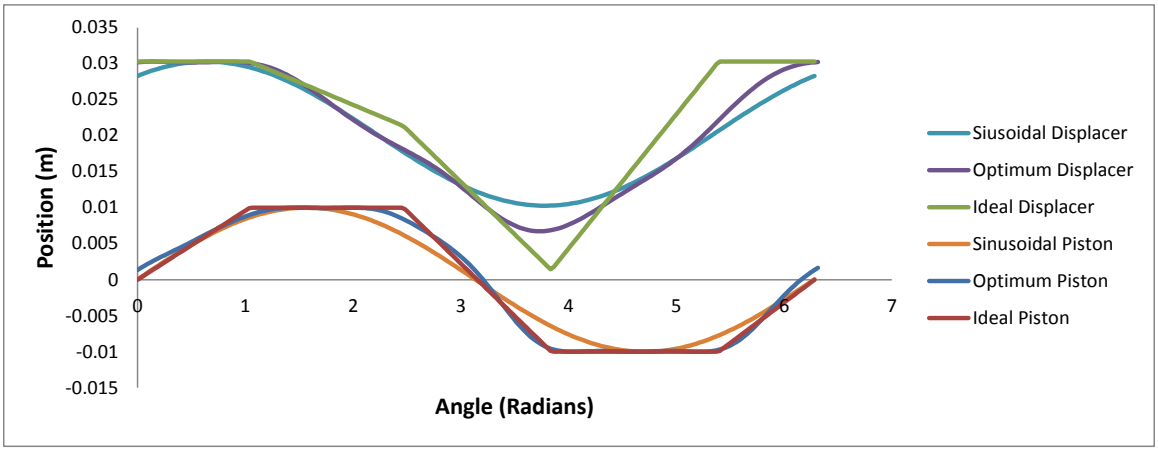

Figure 26 - Sinusoidal, ideal, and optimal piston and displacer motion

The results in this section are specific to this engine design and should not be interpreted as broad conclusions. Roughly 90% of the viscous dissipation in the cases analyzed comes from the regenerator. If other engine designs use less effective regenerators with less pressure drop, or find a method of achieving equal effectiveness while increasing porosity, it may be possible to benefit from ideal waveforms, and the

optimal waveforms will likely change from those presented in the analysis above. In a more general sense, the optimum piston and displacer waveforms are functions of temperature and pressure gradients within the regenerator and heat exchangers and seal leakage, and should be determined on a case by case basis.

The objective function in the optimization presented above does not consider efficiency. Designers could perform optimizations with different objective functions, weighing both power density and efficiency and arriving at a different solution. However, the analysis in this section shows that power density optimization of the piston and displacer waveforms have the potential to increase power density under Case 1 constraints, which were the most restrictive constraints considered in the prior isothermal analysis. Table III summarizes the results of the Sage analysis of ideal motion under Case 1 constraints.

Table III - Summary of Sage predictions for ideal and sinusoidal motion under Case 1 constraints

	Ideal Heating Dwell (Rad)	Ideal Cooling Dwell (Rad)	Piston Power (W)	Displacer Power Requirement (W)	Net Power (W)	Eff (%)
Symmetric Short Dwell	$\pi/4$	$\pi/4$	1680	1630	50	1.2
Symmetric Medium Dwell	$\pi/2$	$\pi/2$	1580	760	820	16.5
Symmetric Long Dwell	$3\pi/4$	$3\pi/4$	1320	690	630	12.7
Asymmetric Min RMS Velocity	2.82	0.91	1580	430	1150	21.8
Maximum Power density	N/A	N/A	1580	150	1430	27.9
Sinusoidal Piston Free-Displacer	N/A	N/A	1170	0	1170	30.7

Optimized Waveforms under Case 2 Constraints

Since constrained optimization identifies piston and displacer motion that improves Stirling engine power density and since ideal piston and displacer waveforms result in reduced power and efficiency, further analysis focuses on optimized waveforms which do not necessarily attempt to approximate the ideal piston and displacer waveforms. The optimized waveforms typically lie somewhere in between the sinusoidal and ideal waveforms, taking advantage of low losses associated with sinusoidal motion while also benefiting from the increased power output of ideal motion.

Under Case 2 constraints the limits of piston and displacer motion are set equal to those of an engine operating with sinusoidal motion, forcing the displacer to dwell at its inmost position during the expansion process rather than following the piston as under Case 1 constraints. The power density predicted by isothermal analysis for Case 2 constraints is higher than those predicted in Case 1 because the Case 2 constraints allow the engine to reach a lower minimum compression space volume than is achievable in Case 1. The difference between ideal motion under Case 1 and Case 2 constraints is illustrated in Figure 27 for a symmetric medium dwell case.

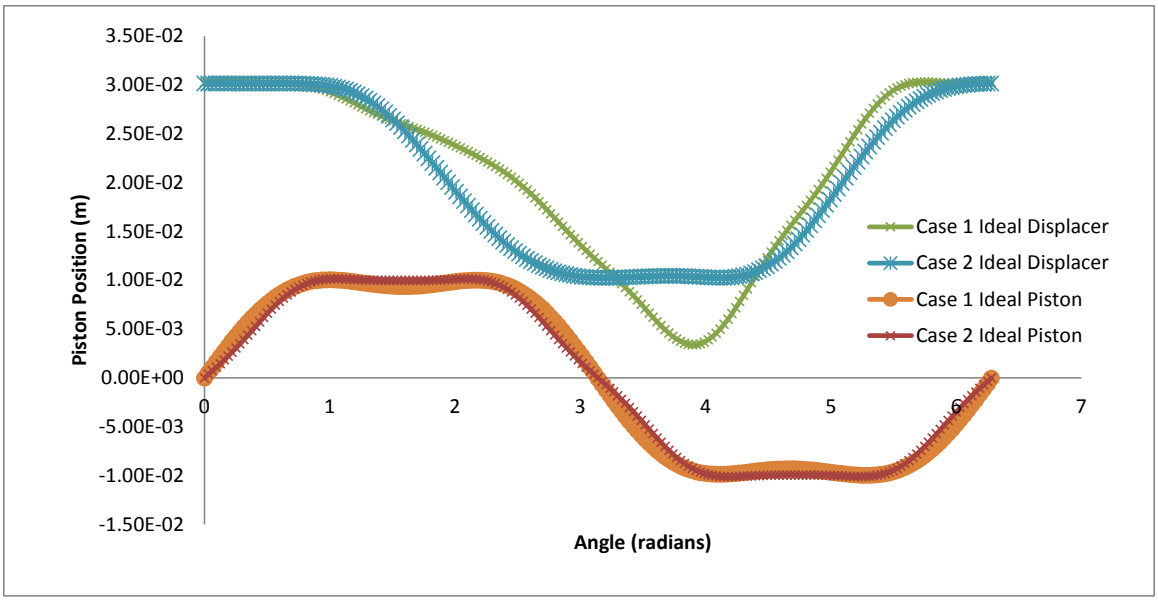

Figure 27 - Case 1 & Case 2 Ideal Piston and Displacer Motion for the medium dwell case

Figure 28 shows motion, instantaneous power, and F-D diagrams for the piston and displacer for optimized motion under Case 2 constraints. Case 2 optimal motion results in a piston power of 1730 W with 100 W on the displacer, for a net power of 1630 W at an efficiency of 26.6%. This is a power density improvement of 39% and an efficiency reduction of 13%. Optimized piston and displacer motion under Case 2 constraints could be preferable to sinusoidal motion in applications that give higher weight to power density.

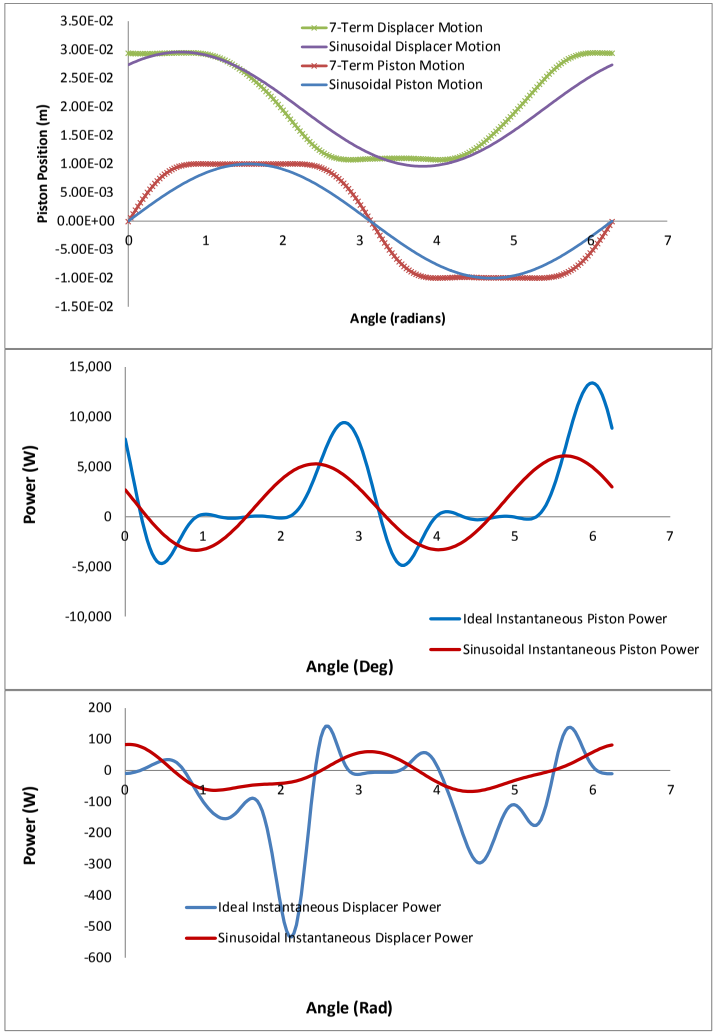

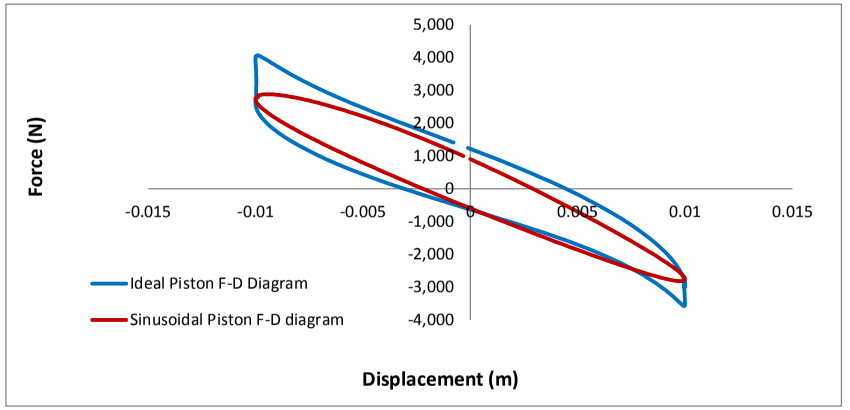

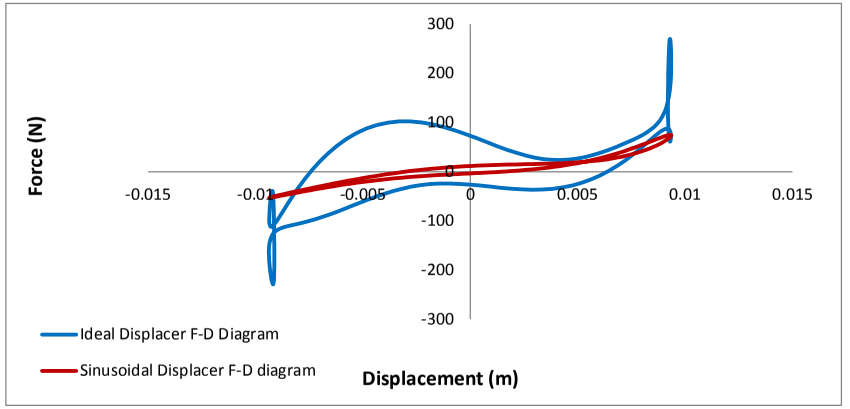

Figure 28 - Piston/Displacer motion, power, and F-D diagrams for optimized Case 2 motion

Optimized Waveforms under Case 3 and Case 4 constraints

Cases 3 and 4 both constrain the out-limits of piston and displacer motion. Case 3 constrains the in-limit of piston travel leaving the in-limit of the displacer unconstrained. Case 4 constrains the in-limit of displacer travel leaving the in-limit of the piston unconstrained. When analyzing ideal motion these cases are treated separately. Focusing on optimal motion allows these cases to be treated as a single case in which neither in-limit is constrained and an optimum solution can be found. In other words, the solver is free to choose either the Case 3 or Case 4 solution, or any intermediate solution in which both the piston and displacer travel further inward than they do in the sinusoidal case.

Figure 29 shows motion, instantaneous power, and F-D diagrams for the piston and displacer for optimized motion under Case 3/4 constraints. This case takes advantage of the inward travel of both the piston and displacer, resulting in a reduced piston dwell time at the in-limit. Case 3/4 optimal motion results in a piston power of 1853 W with 3 W required to drive the displacer, for a net power of 1850 W at an efficiency of 25.3%. This is a power density improvement of 58% and an efficiency reduction of 17.6%. Again, this opens a viable trade between power density and efficiency that could improve system level performance in applications that value power density over efficiency.

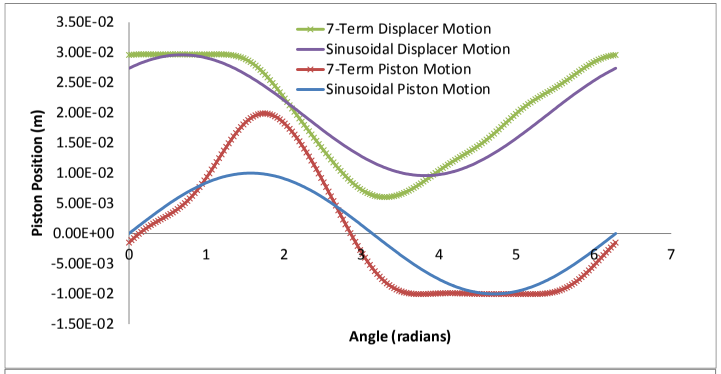

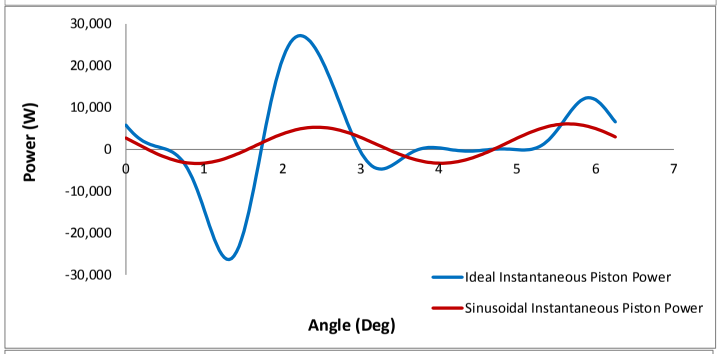

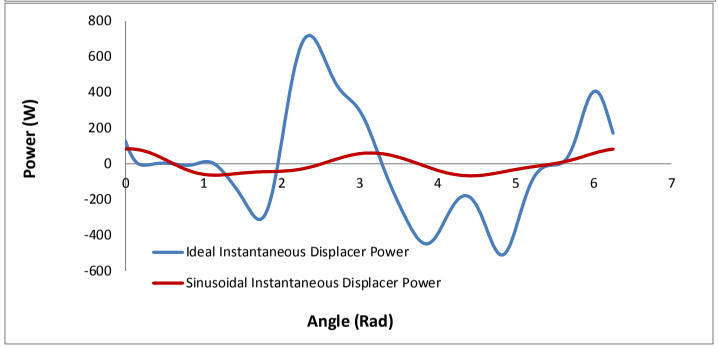

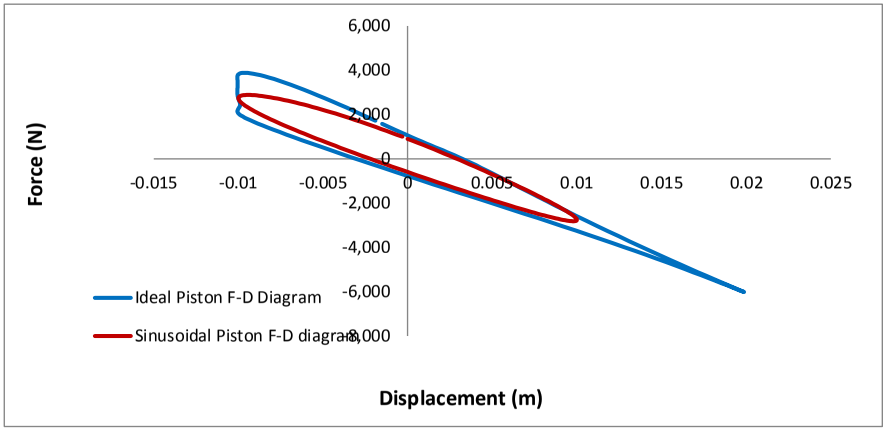

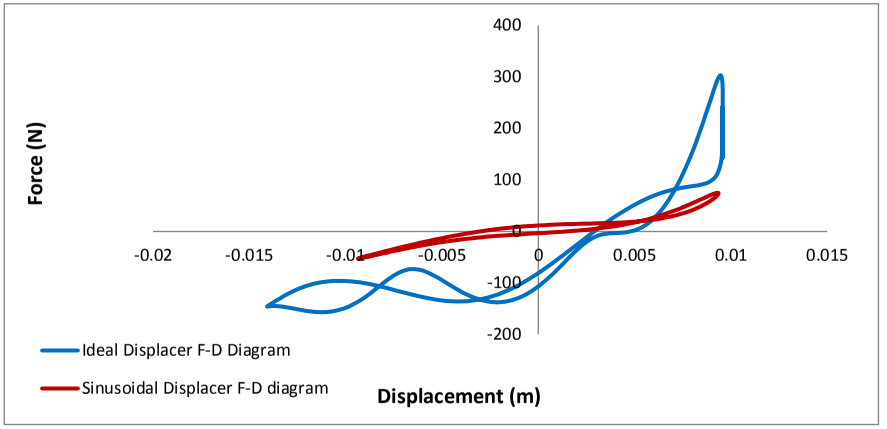

Figure 29 - Piston/Displacer motion, power, and F-D diagrams for optimized Case 3/4 motion

Optimized Piston Waveform with a Free Displacer

The cases analyzed above may be unrealistic for some free-piston engine designs. Optimized displacer motion can only be achieved if the displacer is designed to resonate with the prescribed motion or if an external forcing function is applied to achieve the prescribed motion. Typical free-piston Stirling engines use a single degree of freedom displacer with a nearly linear spring that is incapable of achieving the multi-harmonic motion. Typical free-piston designs also have no mechanism (i.e. linear alternator) capable of imparting a forcing function on the displacer, so it cannot be forced to achieve ideal motion. If engine designers want to take advantage of the potential benefits of ideal displacer motion on free-piston engines they have to consider design changes such as non-linear springs, multi-degree of freedom displacers, and/or displacer alternators. These modifications may be impractical, so it is useful to determine the benefits of optimizing piston motion while allowing the displacer to remain free.

In this analysis displacer motion is not driven, instead it is an output of the model, calculated by balancing pressure forces, spring forces, and drag forces on the displacer and requiring a net zero work input. Under these conditions the displacer motion is not necessarily sinusoidal, since the pressure wave and drag forces can be non-sinusoidal, but the high stiffness of the linear displacer spring results in displacer motion that is nearly sinusoidal.

Optimized piston waveforms achieve higher power at the same limits of motion by increasing the amplitude of the first harmonic, which carries real power, and adding additional harmonics that return the limits of piston motion to their original levels. The higher harmonics typically do not carry or require very much real power, resulting in a

net increase in power. Increasing the magnitude of the first piston harmonic also increases the amplitude of the pressure wave. The increased pressure wave results in an increase in the displacer amplitude unless there is a mechanism to control/limit this amplitude. In the case of a free displacer there is no external force available to limit the out-displacer position, so this constraint can only be achieved by limiting the magnitude of the first harmonic of the pressure wave and piston motion, which also limits the maximum achievable power.

Figure 30 shows motion, instantaneous power, and F-D diagrams for the piston and displacer for optimized piston motion under Case 3/4 constraints using a free displacer. The resulting optimized piston motion is rather close to sinusoidal motion, with a slight deviation to take advantage of the potential increase in working space volume allowed under Case 3/4 constraints. Optimal piston motion, under these constraints results in 1230 W with 0 W required to drive the displacer at an efficiency of 29.4%. This is a power density improvement of 5% and an efficiency reduction of 4%. Although it is theoretically possible for this case to be of benefit in some applications, with the power density improvement being relatively modest, it is not clear whether this would offer any system level advantages once designers take into account the additional complexity of achieving the higher harmonics required to achieve this motion. This case demonstrates that, for the engine analyzed, optimizing piston motion in the absence of optimized displacer motion produces significantly less power density benefit than optimizing both.

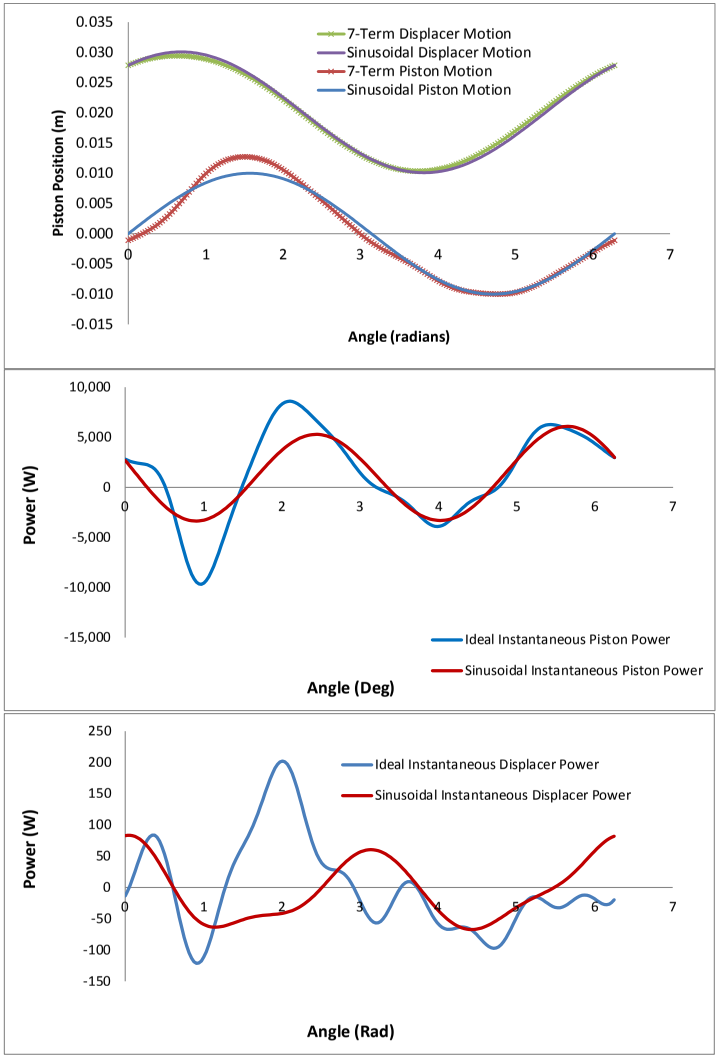

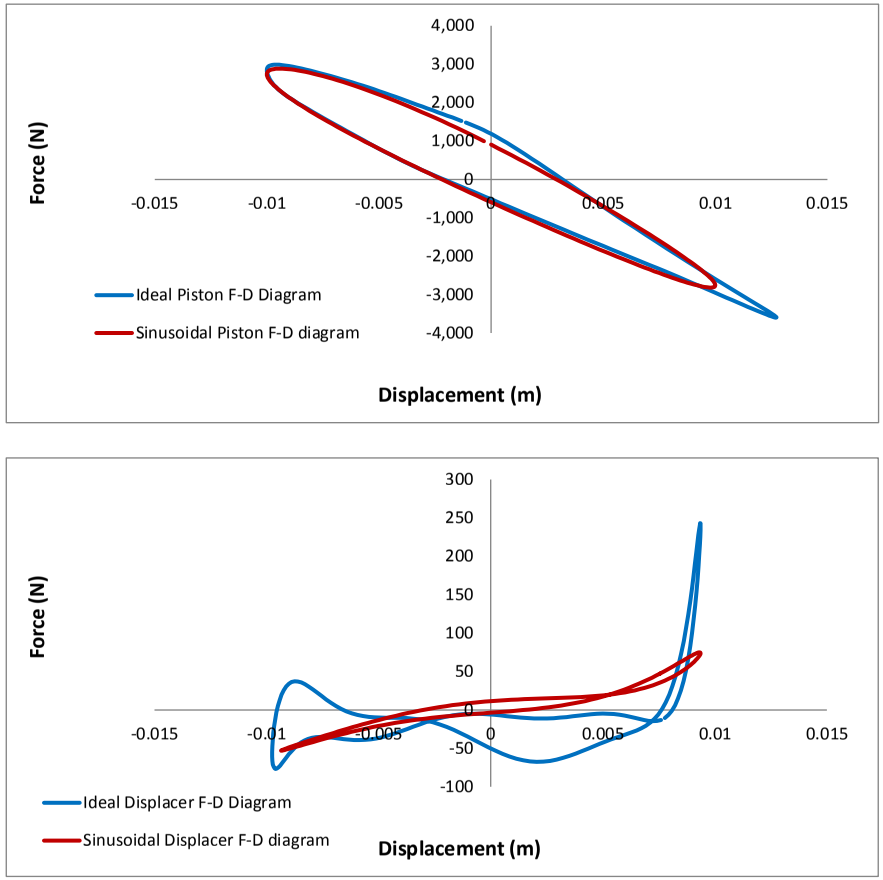

Figure 30 - Piston/Displacer motion, power, and F-D diagrams for optimized Case 3/4 with and optimized piston and free displacer

Optimized Displacer Waveform with a Sinusoidal Piston

Keeping a sinusoidal piston waveform guarantees single frequency sinusoidal voltage, which can simplify control electronics. Since the displacer is typically lighter than the piston, imposing non-sinusoidal waveforms on the displacer could be easier and more practical in some cases than imposing non-sinusoidal waveforms on the piston. This configuration requires some mechanism to enforce non-sinusoidal motion on the displacer and the possibility of external work input/extraction.

Optimal displacer motion, under these constraints results in 1550 W with 190 W required to drive the displacer giving a net power of 1360 W at an efficiency of 27.0%. This is a power density improvement of 16% and an efficiency reduction of 12%. Optimization of displacer motion using a sinusoidal piston results in more power density improvement that the optimized piston with a free displacer, but both of these cases fall well short of the power density improvements that occur when both the piston and displacer motions are optimized. Furthermore, the efficiency penalty that is paid in these cases is greater than what is seen when both the piston and displacer are optimized, as shown in Figure 32. Figure 32 illustrates the differences in the performance benefits of the various types of constraints considered in this analysis. It should not be interpreted as a comprehensive view of the trade space between power density and efficiency for a given engine. For example, one could generate a curve of power density versus efficiency for each case by including both power density and efficiency in the objective function during optimization and varying the weight given to each, generating a new data point for each combination of weights. Figure 32 shows the special case of power density being weighted 100% and efficiency being weighted 0%. Such a chart would

certainly be interesting, but detailed analysis of the power density / efficiency trade space is outside the scope of this analysis and is left to future work.

This analysis reveals that displacer-only optimization is more effective than piston-only optimization at increasing power density. This analysis also shows that the power density improvement seen with simultaneous optimization of the piston and displacer is greater than the sum of independent piston and displacer optimization.

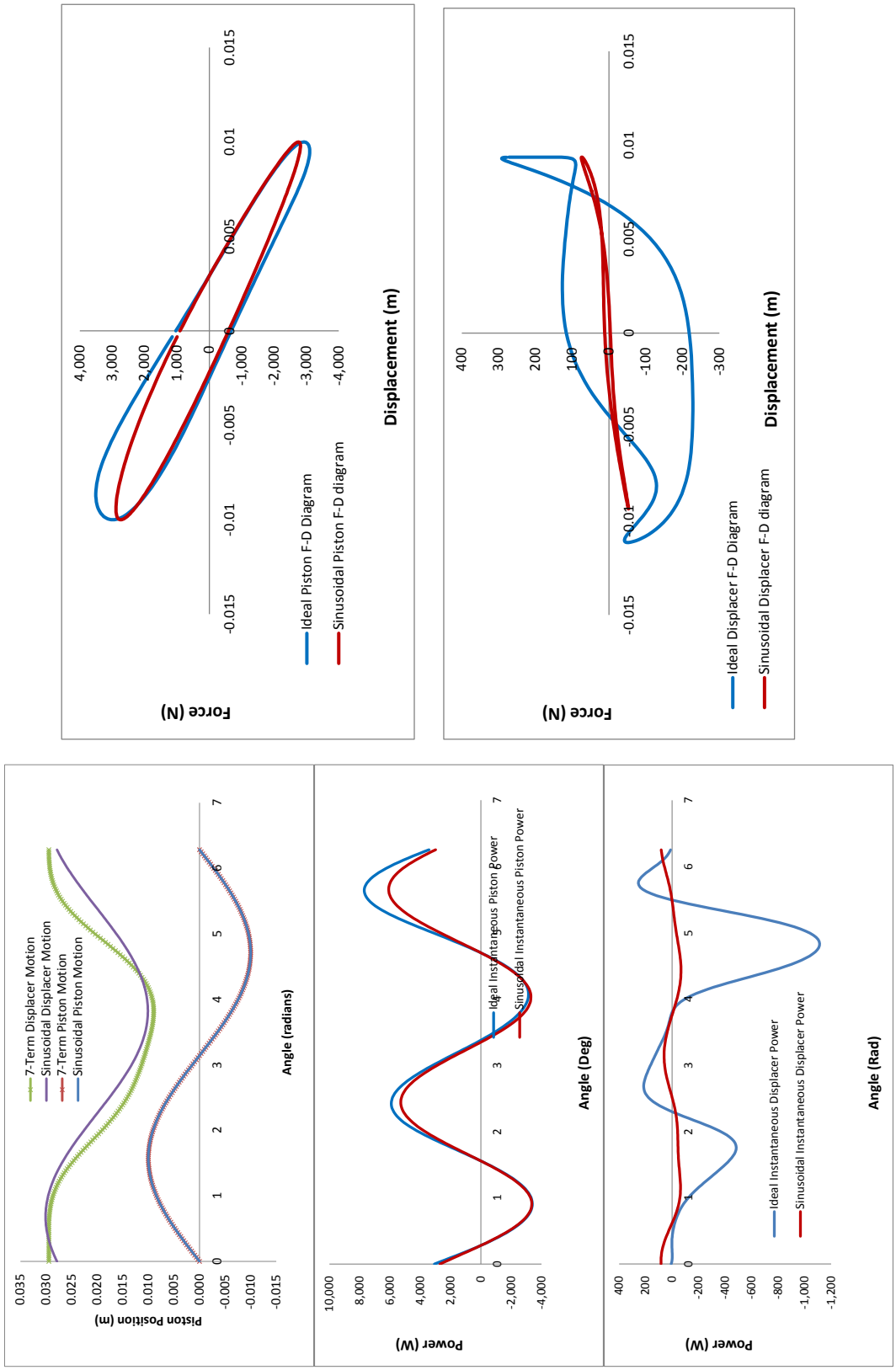

Figure 31 - Piston/Displacer motion, power, and F-D diagrams for optimized Case 3/4 with and sinusoidal piston and optimum displacer

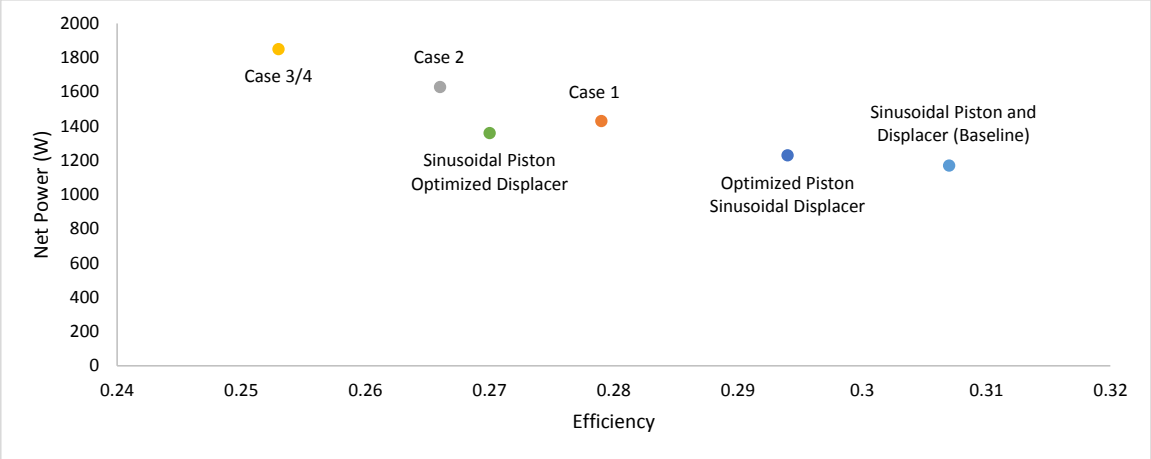

Figure 32 - Power density versus efficiency under various constraints

Experimental Testing

The numerical analysis above suggests that Stirling engine power density and efficiency can be traded against each other and specified to the designer's needs. This section describes a test performed in the NASA Glenn Stirling Research Lab intended to verify that non-sinusoidal piston motion is achievable and that the Sage nodal analysis tool accurately predicts the performance of engines with non-sinusoidal pistons.

The engines chosen for testing use a stiff linear spring on the displacer and have no alternators/actuators to apply an external forcing function, so none of the cases involving optimized displacer motion can be tested. Since there is no method of constraining the displacer in this test setup the displacer is free to travel beyond the out-limit measured during sinusoidal piston testing. For this reason, this experiment does not necessarily validate predictions of increased power density, because in some cases the

engine cylinder would be forced to grow to accommodate the displacer motion. However, the experiment does show that non-sinusoidal piston waveforms are achievable and allows nodal analysis predictions to be compared to experimental data.

Since the engines are not designed to resonate at higher harmonics, higher harmonic motion must be imposed by the alternator, increasing the spring force provided by the alternator and the alternator current. The current required to run non-sinusoidal piston waveforms at the nominal operating amplitude of 10 mm saturates the alternator before the waveforms can be substantially altered. However, measurable changes in piston motion and engine performance can be achieved when operating at reduced amplitude. The Stirling engines chosen for experimental testing use hydrostatic gas bearings to support the piston and displacer as they move relative to the cylinder. These gas bearings are charged using the cyclic pressure of the engine which is a function of the piston/displacer amplitude. Six millimeters is the minimum recommended piston amplitude for charging the bearings, and is chosen as the baseline for the experiment. The out-limit of piston motion for all tests is set equal to the value measured during sinusoidal testing. The first harmonic of the piston amplitude is then increased and additional harmonics are added until the out-limit of piston motion returns to the value measured during 6 mm baseline testing. The non-sinusoidal piston waveforms are allowed to exceed the in-limit of piston motion, consistent with constraint Case 4.

Facility

Testing was conducted in the Stirling Research Lab (SRL) at the NASA Glenn Research Center. Currently, the primary purpose of the SRL is life testing and system integration of the 80 Watt Advanced Stirling Convertor (ASC), which was intended as a

replacement for the Multi-Mission Radioisotope Thermoelectric Generator (MMRTG) in low power science missions. Previous work done at the SRL includes several Stirling technology development efforts, such as advancing the Technology Readiness Level (TRL) of the ASC, sub-scale testing of engine concepts for Fission Surface Power (FSP), testing of a 25 kW Stirling engine for space power, and testing of a 40 kW Stirling engine for automotive applications.

Since designing an engine and controller from scratch to meet the unique requirements of this test is costly, hardware was chosen from the existing and available Stirling engine test stands at the SRL with a focus on reducing cost by minimizing the amount of modification required to the engine and support hardware (including the control system). Stirling engines are commonly tested in pairs so that the vibration forces of one cancel each other. The engines chosen for testing were a pair of 1-kW engines previously used to test a sodium-potassium (NaK) heat exchanger [28] and to test the feasibility of operating two engines with a common expansion space [29] for the Fission Surface Power project. The 1 kW engines were selected for the following reasons:

1. Having completed their originally intended test sequence these engines are of little value to the FSP project and are available for relatively high risk tests.
2. They are integrated with a fully functional test stand, reducing infrastructure costs (data acquisition, instrumentation, power, plumbing, etc.). Figure 33 shows the High Power Stirling Test Rig in the SRL, configured for common expansion space testing with a dashing young man at the controls.
3. These engines were designed for commercial/residential use and have a robust alternator capable of handling higher forces (current). ASC engines designed

for space applications have less alternator margin to reduce mass, limiting the scope of achievable waveforms.

4. System level trade studies of ASC applications favor high efficiency over engine power density. Comparatively, system level trade studies of fission power systems weight power density of the engines higher, making the study of non-sinusoidal piston motion more relevant to higher power fission applications.

Figure 33 - High Power Stirling Test Rig at the Stirling Research Lab

Using an engine and control system designed for sinusoidal motion has several drawbacks which are outlined below and described in more detail in the Background subsection:

1. Free-displacer on a linear spring

a. No ability to control displacer motion

b. Linear spring results in nearly sinusoidal displacer motion

2. Piston designed to resonate only at the fundamental engine frequency

    a. Large alternator forces are required to impose higher harmonic motion

    b. Large alternator forces require large alternator currents

        i. Increases resistive losses

        ii. Large deviations from sinusoidal motion result in alternator saturation.

        iii. Large currents at higher harmonics increase the terminal voltage because of the alternator inductance, requiring higher voltage ratings for the control system.

3. Tuning capacitors can only cancel alternator inductance at a single frequency

    a. In single harmonic systems the entire alternator inductance can be canceled using a tuning capacitor, resulting in relatively low control system voltages.

    b. In multiple harmonic systems, only one of the harmonics can be canceled. Higher harmonic voltages are not canceled, so the control system AC Bus must be sized to handle the higher harmonic voltages.

        i. This problem could potentially be mitigated by making changes to the circuit layout between the alternator and AC bus.

4. AC Bus control scheme allows for a maximum of 3 harmonics

    a. It is advantageous to build the control system in harmonic stages in which synchronized AC Buses provide one harmonic per stage.

b. Per the manufacturer's specification, a maximum of three AC buses may be synchronized.

The list above could be interpreted as an argument that the increased complexity of using higher harmonics and optimized waveforms outweighs the potential benefit. This would be true if adding higher harmonics necessarily elicited all of these problems. However, the problems stated above are not inherent to higher harmonic motion; they are the result of applying such motion to engines that are not designed to do so. For example, if the prescribed motion is achievable using nonlinear springs on the piston and/or displacer, then the desired waveforms would not require large alternator currents, which would decrease the terminal voltage, decrease resistive losses, reduce voltage requirements on the control system, and might allow for additional harmonics beyond the third.

The methods used in this experiment are not ideal for demonstrating system level benefits of using non-sinusoidal waveforms on Stirling engines. However, the intent of this experiment is to achieve a proof-of-concept on existing and available hardware and provide an experimental database for comparison to model predictions. Sophistication and optimization of the overall engine and control system is left to future work.

Background

In free-piston engines, the electromotive force (EMF) of the alternator is proportional to the piston velocity (the constant of proportionality is the motor constant or voltage constant and is a function of the number of alternator windings and wire geometry). The alternator current is proportional to the force imparted to the piston by

the alternator (the constant of proportionality is equal to the force constant, which is equal to the inverse of the voltage constant in ideal alternators). When the piston EMF waveform is composed solely of the piston resonant frequencies, no spring force is required from the alternator to achieve the desired waveform. In this case the alternator supplies a pure damping force, proportional to piston velocity, to harvest the piston power. Since the alternator EMF is also proportional to velocity, running at resonance results in the alternator current and EMF being in phase. When running a piston off of resonance, the alternator provides a spring force in addition to the damping force to achieve the prescribed waveform. This increases alternator force and alternator current, resulting in lower power factor and increased resistive losses. Large alternator forces (current) can saturate the alternator, limiting the variety of waveforms that can be tested. Modifying the engine to include non-linear springs on the piston and/or adding additional degrees of freedom to the piston would reduce the spring force required from the alternator and increase the variety of waveforms that could be tested. However, this level of engine modification is beyond the scope and budget of this project.

Alternator inductance causes the voltage measured at the alternator terminals to be larger than the EMF and out of phase with the alternator current (even when the engines are operated at resonance). In single harmonic engines, a tuning capacitor can be used to cancel the alternator inductance so that the controller voltage is reduced to the level of the EMF and the current and "post-capacitor" voltage are once again in phase. However, when additional harmonics are introduced, the tuning capacitor cannot cancel the alternator inductance of the higher harmonics so the voltage required of the control system is higher than the EMF seen by the piston. The alternator inductance and tuning

capacitor act as a band pass filter, passing the fundamental frequency with a gain of one and phase shift of zero, and reducing the amplitude of all other frequencies. Adding higher harmonics to the piston motion introduces frequencies that are well off of the fundamental frequency, so adding a relatively small harmonic voltage to the EMF requires a much larger voltage input from the control system. There may be an alternative solution to this problem involving changes to the control system electronics, but this experiment used the "brute force" approach, in which the AC buses used as the control system supply relatively large voltages in order to impose relatively small piston EMF. For example, a peak-peak third harmonic voltage of 420 V resulted in an estimated peak-peak EMF of 30 V (estimated EMF based on piston velocity measurements times the motor constant). The Chroma 61605 power supplies procured for this test are 4 kVA units limited to 300 V. Two of these units were wired in series and to a step-up transformer to allow a maximum of 850 Vrms at either the second or third harmonic. However, engine/alternator limitations were reached well before the 850 Vrms limit was reached. The higher harmonic power supplies are synchronized with each other and with the 50 Hz power supply to guarantee proper phasing. The manufacturer limits the number of Chroma 61605 power supplies that may be synchronized to three, which in turn limits the scope of this test to adding a maximum of two additional harmonics beyond the fundamental. The second and third harmonics (100 Hz and 150 Hz) are chosen because analysis shows that these provide measurable power density benefit at voltages and currents that are within the specifications of the engine and control system power supplies.

In the case of a free-displacer there is no mechanism to externally drive displacer motion. Displacer motion is determined by the pressure wave of the engine and any internal springs (gas springs or linear springs). The displacers on the 1 kW engines are attached to stiff linear springs and the resulting motion is very nearly sinusoidal, even when the piston motion and pressure wave are non-sinusoidal, reducing the maximum achievable power density as shown in the previous piston-only optimization. The amplitude of the displacer motion is primarily a function of the magnitude of the first harmonic of the pressure wave, which is a strongly correlated to the magnitude of the first harmonic of the piston motion. Unfortunately, the engine power output is also a strong function of the first harmonic of the piston motion, so it is difficult to increase the power output of the engine without increasing the out-limit of displacer motion in free-displacer engine designs. Since there is no mechanism available to control displacer motion the out-limit of displacer motion is not forced to remain the same as in the sinusoidal case, so the results of these experiments do not necessarily prove that non-sinusoidal waveforms increase power density. The experiments do, however, demonstrate the feasibility of tailoring non-sinusoidal waveforms in free-piston engines to achieve performance benefits, and provide an experimental database for comparison with model predictions. Higher fidelity testing requires engine modification and is left to future work.

Test Setup

Stirling Engines

The engines chosen for testing are a pair of 1-kW engines procured from Sunpower Inc. in 2007. These engines, referred to either as the P2A or EG-1000 engines, were originally designed for commercial operation in European cogeneration systems,

and are therefore intended for use at 50 Hz with a natural gas burner for heat addition, but were modified for electric heating prior to delivery. In 2007 the engines were baseline tested using electric heating elements and then modified to include a liquid metal heat exchanger and tested in a liquid metal loop at the NASA Marshall Space Flight Center as part of a pathfinder effort in support of the Fission Surface Power (FSP) Technology Demonstration Unit (TDU) [28] [30]. The two separate engines were then combined into a single engine with a common expansion space as part of ongoing support of the FSP TDU (Figure 34). These tests show no power degradation as a result of combining the expansion spaces [29]. Combining expansion spaces produced small periodic power oscillations, but this issue is easily mitigated by changing controller layout [31]. Having completed their test sequence in support of the FSP TDU, the engines were available and had existing infrastructure in place to support testing. The complexity of combined expansion spaces is perceived as a minor issue, making the P2A engines the most viable candidates for testing non-sinusoidal waveforms.

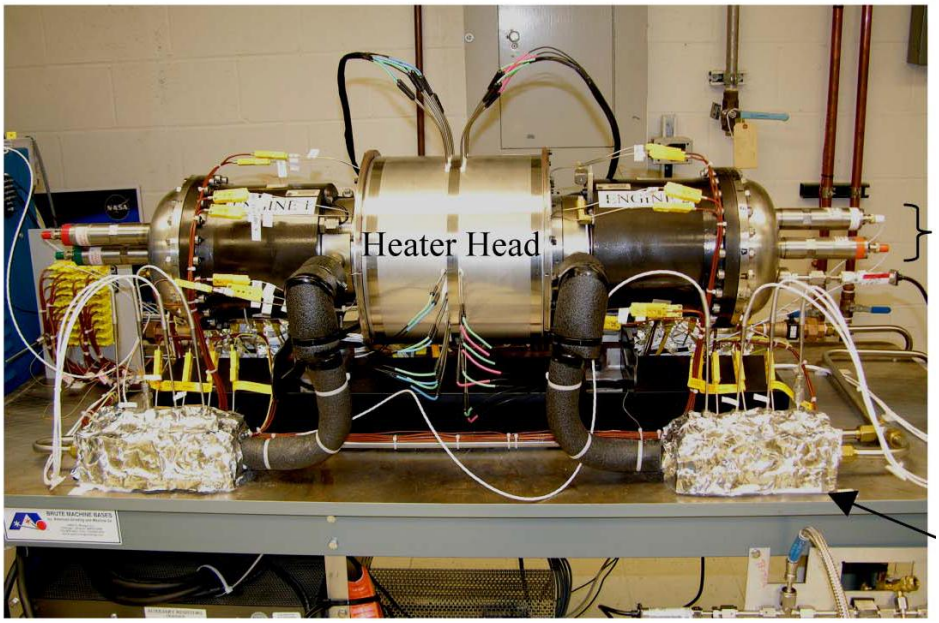

Figure 34 - P2A Engines in the Thermodynamically Coupled Configuration in the Stirling Research Lab

Control System

The control system consists of 3 synchronized AC power supplies, a step-up transformer, load resistors, and tuning capacitors (Figure 35). All three AC power supplies are Chroma 61605's capable of 4 kVA and 300 Vrms. During prior P2A testing each engine used a dedicated power supply and synchronization of the power supplies was used to synchronize the engines. In the common expansion space configuration, small drifts in power supply synchronization resulted in small power oscillations [31]. This issue was resolved by using a single power supply to control both engines, guaranteeing that both engines operate on a common waveform. The single power supply configuration has been used on several other test stands in the Stirling research lab and is not considered a risk. Analogously, the configuration shown in Figure 35 will result in the same waveform being imposed on both engines. Small drifts in power

supply synchronization can result in small changes in the waveform, but the same waveform will be imposed on both engines. The two drawbacks of using a single power supply are that the current requirement for the power supply increases, increasing size and cost and it is not possible to match baseline conditions of both engines simultaneously. For this reason, one engine was selected as the matched engine and all data is reported from that engine. For the purposes of this test, the other engine can be thought of as a balancer.

The Chroma 61605 can be programmed to accept arbitrary waveforms. Which contain multiple harmonics. In theory, this feature could be used to impose the desired waveform on the piston with a single power supply. However, the capacitors C3-C8 shown in Figure 35 are used to reduce the current required from the Chroma and must be sized for a specific frequency. The current required to operate a single Chroma at multiple frequencies without the aid of capacitors sized for a specific frequency is prohibitive, so a staged approach is used instead. In the staged approach, Chroma 1 operates at the fundamental frequency of 50 Hz. The series capacitors C1 and C2 are tuned to the fundamental frequency and reduce the voltage required from Chroma 1. Chromas 2 and 3 operate at either the second or third harmonic and the parallel capacitors C3-C8 reduce the current required from the power supplies. The series Chromas 2 and 3 are capable of producing a combined 600 VRMS. The original intent of the experiment was to reach a maximum voltage of 850 VRMS, so the Chromas 2 and 3 were wired to a step-up transformer, which also electrically isolates the Chroma 1 from the others.

Even when the piston is forced to operate at higher harmonics, the vast majority of the true power produced by the engine is carried by the first harmonic. Therefore the

load resistors R1 and R2 (32 ohms each) are sized to dissipate the majority of the power. The Chroma power supplies have no ability to sink power, so the resistors R3 – R6 are sized to limit the current requirement, but also ensure that Chromas 2 and 3 always operate as a source, never as a sink (5000 ohms).

The relays K1 and K2 depicted in Figure 35 are part of the safety system and are designed to open if the engine reaches an overstroke condition. Additional connections depicted in Figure 35 include voltage monitoring, connections for stall loads, and a bypass connector used when operating the engines at the fundamental frequency only.

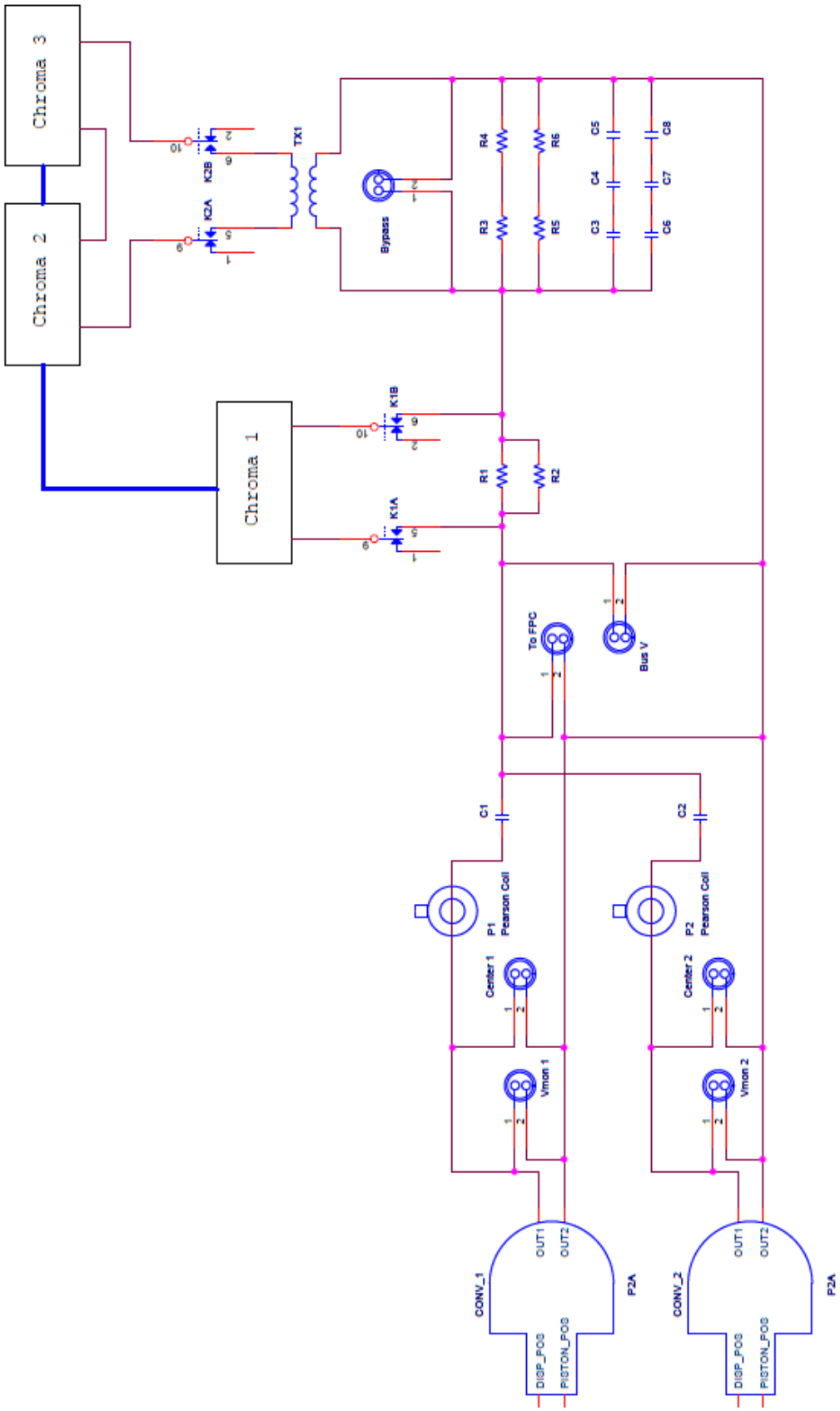

Figure 35 – P2A control system schematic

Auxiliary Systems

Heat input is provided using cartridge heaters capable of delivering 4 kW of power to each engine. Voltage to each of these heaters are regulated using a Variac. Each engine uses a separate Variac so that the average hot-end temperature of the engines can be made equal despite heater cartridge variability and differences in thermal resistance between the cartridges and the engines. Heater power is measured and is used to calculate gross engine efficiency.

The cold end of the engine is water cooled using a recirculating water chiller. Water flow rate and temperature are measured, allowing for the heat rejected to the water to be calculated. However, due to the relatively small temperature difference across the engine the heat rejection typically has a larger uncertainty than the gross electrical heat input and is not used as the primary method of calculating engine efficiency.

Data Acquisition

Piston and displacer motion are measured using Fast Linear Displacement Transducers (FLDT). Alternator current is measured using a Pearson coil on each engine. The FLDT signals are read into Tektronix DPO 70404 oscilloscope to capture the waveform in real time. A Yokagawa WT 1600 high percision power meter, which is also capable of recording waveforms, is used to measure alternator current and pre-capacitor voltage. The post-capacitor voltage and alternator current are read by a Tektronix TDS 3014C oscilloscope. Both scopes and the power meter are synchronized using the Engine 2 piston FLDT signal to guarantee proper phasing during post-processing.

Hot-end temperature on the engine is measured using eight type K thermocouples. Cooling water temperature on each engine is measured using eight platinum RTDs (four each on inlet and outlet). Housing temperature and bounce space gas temperature are also measured using 4 thermocouples on each engine. Heater power is measured using a Yokagawa WT 230 power meter.

Steady-state measurements are taken at a rate of 1 Hz, using a Labview data acquisition system which is standard for all test stands in the Stirling Research Lab. Higher speed data, on the order of kHz are taken using the oscilloscopes power meter described above.

Methodology

Each test begins by establishing a steady-state baseline at 6 mm amplitude, 550 ºC hot-end temperature and 50º C Cold-end temperature. The baseline point uses only the first harmonic power supply, producing sinusoidal piston motion, which is the typical operating mode of free-piston Stirling engines. This point is used to establish both the baseline power measurement and the out-limit of piston motion which is matched by all non-sinusoidal waveforms. At the conclusion of baseline testing the AC Bus voltage of the second or third harmonic is increased by 45 V at a phase angle of 180 º relative to the 50 Hz AC Bus voltage. This results in a decrease in the out-limit of piston motion as the bottom of the waveform flattens. The out-limit of piston motion is then returned to the baseline value by increasing the voltage of the 50 Hz AC Bus. Heater power is then increased to maintain a hot-end temperature of 550 ºC. This process is then repeated until some limit is reached. While the AC Bus increment of 45 V results in a relatively coarse test matrix, it was chosen because this increment resulted in a measurable change

in the out-limit of piston motion for both the second and third harmonic. Smaller increments could be used if the piston position measurement was made more precise and/or repeatable from cycle to cycle. Periodically throughout testing the baseline point was revisited to establish repeatability and to verify that the lower limit of piston motion had not changed. The phase angle of 180º was chosen for both the second and third harmonic waveforms because it produced piston waveforms that most closely matched the desired piston phasing as determined from optimization using nodal analysis. Exploration of phase angle sensitivity and influence on other parameters such as efficiency is left to future work.

Although the control system is capable of providing 850 Vrms to the alternator, engine and/or alternator limits were reached well before these voltages were achieved. Testing beyond 160 Vrms on the second harmonic AC Bus results in unbalanced current between engines, erratic power measurement, and eventually an overstroke protection circuit trip, resulting in engine stall. It is not clear why these operating conditions cause the engines to become unstable, since it is well below the engine manufacturer's prescribed limits on the alternator voltage and current, but the instability is repeatable, resulting in an abbreviated second harmonic test matrix. Testing beyond 295 Vrms on the third harmonic results in an audible, and abnormal noise coming from the engine. This noise was not consistent with any type of impact, whether piston-displacer or piston-endstop, and could be benign. However, testing beyond 295 Vrms on the third harmonic is avoided in an effort to preserve the engines. When operating with both the second and third harmonics simultaneously, a similar noise is heard when the third harmonic voltage increased beyond 105 Vrms. These engine/alternator/control constraints provided the

operational limits for non-sinusoidal testing. Table IV summarizes the control inputs for the points tested. AC Bus voltages shown in the Point Description column describe nominal values input by the operator during testing. The alternator and post-cap voltage columns are measured values.

Table IV - Test Matrix

Point Description (Based on AC Bus Voltage)	50 Hz Alternator Voltage (Vrms)	100 Hz Alternator Voltage (Vrms)	150 Hz Alternator Voltage (Vrms)	50 Hz Post-Cap Voltage (Vrms)	100 Hz Post-Cap Voltage (Vrms)	150 Hz Post-Cap Voltage (Vrms)
Baseline	177	0	0	145	0	0
45 V 2nd Harmonic	190	96	0	152	66	0
90 V 2nd Harmonic	202	192	0	159	133	0
110 V 2nd Harmonic	207	236	0	161	162	0
45 V 3rd Harmonic	183	0	82	148	0	73
90 V 3rd Harmonic	187	0	166	151	0	147
135 V 3rd Harmonic	192	0	250	153	0	221
180 V 3rd Harmonic	197	0	333	156	0	295
45 V 2nd Harmonic 45 V 3rd Harmonic	194	96	83	154	66	74
45 V 2nd Harmonic 90 V 3rd Harmonic	199	96	166	157	66	147
90 V 2nd Harmonic 45 V 3rd Harmonic	207	192	84	160	132	74
90 V 2nd Harmonic 90 V 3rd Harmonic	212	193	167	162	131	145
110 V 2nd Harmonic 45 V 3rd Harmonic	213	235	83	163	161	73

This experiment aims to compare the thermodynamic power output of free piston engines operating with several different piston waveforms. Unfortunately, the engines could not be modified for dynamic pressure measurement within budget and time constraints, so it is not possible to produce true P-V diagrams based on direct measurements. However, there are several methods of calculating thermodynamic power output based on measured parameters such as alternator power, alternator voltage, alternator current, alternator resistance, and piston position. The most direct power measurement is taken by time averaging of the instantaneous alternator voltage (pre-capacitor) multiplied by the instantaneous current at the alternator terminals. This measurement was made using the internal algorithms of the Yokagawa WT 1600 power meter as well as through post-processing of the voltage and current waveforms. This power measurement has the advantage of being taken as close to the alternator as possible, but has the disadvantage of having low power factor since voltages are taken before the tuning capacitor. An alternative power measurement was taken using the current waveform and the post-capacitor voltage. Both of these measurements include alternator inefficiency, which is dominated by the resistive losses of the coils (alternator resistance is 2.98 ohms). The most direct method of calculating thermodynamic power is to add these resistive losses to the measured alternator power.

Measuring alternator voltage and current to determine alternator power and adding resistive losses is useful for determining the cyclic average and time average power output of the engines, and is used as the figure of merit in the results section. However, this method does not give very much information about the instantaneous performance of the engines, making it less useful for the purposes of model comparison

or potential engine modification. Since instantaneous piston position is measured directly, force displacement diagrams can be generated by calculating instantaneous piston forces as shown below:

$$F_{alt} = i_{alt} K_{Force}$$

$$F_{Net\ Pressure} = (P_{WS} - P_{BS}) A_p$$

$$m_p a_p = (P_{WS} - P_{BS}) A_p + F_{alt}$$

$$F_{Net\ Pressure} = (P_{WS} - P_{BS}) A_p = m_p a_p - i_{alt} K_{Force}$$

$$a_p = \frac{\Delta v_p}{\Delta t} \qquad v_p = \frac{\Delta x_p}{\Delta t}$$

Where F_{alt} is the force imposed on the piston by the alternator, i_{alt} is the instantaneous alternator current, K_{Force} is the measured motor constant based on force, $F_{net\_Pressure}$ is the net pressure force on the piston, P_{WS} and P_{BS} are the instantaneous working space and bounce space pressures, A_p is the piston area m_p is the mass of the piston, a_p is the piston acceleration, and v_P is the piston velocity.

Calculating the net pressure force on the piston requires taking two derivatives of the piston position signal. The piston position is first curve fit using the first 7 harmonic components. Any terms that contribute less than one percent of the fundamental are set to zero, filtering high frequency noise which is magnified by the numeric differentiation process. Central differences are then taken based on the position curve fit to determine piston velocity and acceleration. Force-displacement diagrams are then generated for both net pressure forces and alternator forces and compared to baseline data as well as

model predictions. Both the net pressure force and alternator force F-D diagrams can be integrated to determine thermodynamic power, and these numbers are included in the Results section for reference. However, this method is sensitive to the filtering methods used, and is dependent on a motor constant measurement made at room temperature using a single harmonic, so it is considered less reliable for determining cycle average power than the more direct electric measurements.

Yet another measure of alternator power can be made by multiplying the alternator current by the alternator EMF using the following equations:

$$Power = \frac{1}{2\pi}\oint_0^{2\pi} i_{alt} \mathrm{V}_{EMF}$$

$$\mathrm{V}_{EMF} = \mathrm{v_p} \mathrm{K}_{Vel}$$

Where V_{EMF} is the electromotive force induced by the piston moving through the alternator windings and K_{Vel} is the measured motor constant based on velocity. Since the current is proportional to the force motor constant, and the EMF is proportional to the velocity motor constant and these two motor constants are reciprocals, this method is equivalent to taking the cyclic average of the alternator force times the velocity on the piston. This method is also sensitive to the filtering method and methods used to take derivatives of the piston position, so was not used as the figure of merit for reporting power output. Still, it provides useful information on the instantaneous power output of the engines and is reported for reference.

Calculated instantaneous power and force-displacement diagrams for the displacer are not considered because these diagrams require measurement of the

differential pressure between the compression and expansion spaces. However, since the displacer is free, the displacer net power over a cycle is zero. This allows the engine net thermodynamic power to be calculated directly from piston measurements.

Measured and calculated values are compared to analytical predictions from nodal analysis. Initially, the Sage nodal analysis model was run if free-displacer mode, in which the piston waveform is an input to Sage and the displacer position is an output. However, the Sage predicted piston-displacer phase angles were consistently off by roughly 10º from measured values. This difference is likely the result of differences between the as-designed values of the displacer mass and spring constant from those of the as-built engine. To correct for this, Sage was instead run with a constrained displacer, accepting both the measured piston *and* displacer waveforms as inputs. This typically made little difference in the cyclic steady-state power output, but did change the phasing of the F-D and instantaneous power plots, bringing them into closer agreement with measurements.

Results

Electric power output, cyclic average thermodynamic power, F-D diagrams, instantaneous power, and gross efficiency for each of the points in Table IV are reported in this section. These results are compared to the baseline sinusoidal case, as well as to the predictions of nodal analysis.

The operating conditions for the baseline case are 550 ºC hot-end temperature, 50 ºC cold-end temperature, and 6 mm piston amplitude. The out-limit of piston motion under these conditions is 6.06 mm. The measured out-limit of piston motion was kept

constant throughout higher harmonic testing. Table V below summarizes the various power measurements and calculations described in the Methodology section as well as efficiency. The gross efficiency measured during testing is calculated by dividing the piston power (alternator power plus resistive losses), by the gross heat input (electric power supplied to the cartridge heaters). The gross heat input includes heat that is lost through the engine insulation package, so it underpredicts thermodynamic efficiency. The efficiency calculated by Sage is based on the net heat input, including only the heat that enters the acceptor of the engine. These values are not directly comparable, so they are called out separately.

Table V - Cyclic steady-state data for the baseline case.

	Alternator Power (W)	Post-Cap Power (W)	Alt Power + Resistive Loss (W)	Net Pressure Power (W)	Alternator Force Power (W)	$I*V_{EMF}$ Power (W)	Gross Eff (%)	Net Eff (%)
Measured	411	411	435	463	463	467	26.2	
Sage	422	422	457	457	457	457		33.2
% Diff	2.3	2.3	5.1	1.3	1.3	2.2		

Figure 36 shows the measured piston position, instantaneous power, and F-D diagrams based on both net pressure forces and alternator forces alongside analytical predictions from nodal analysis.

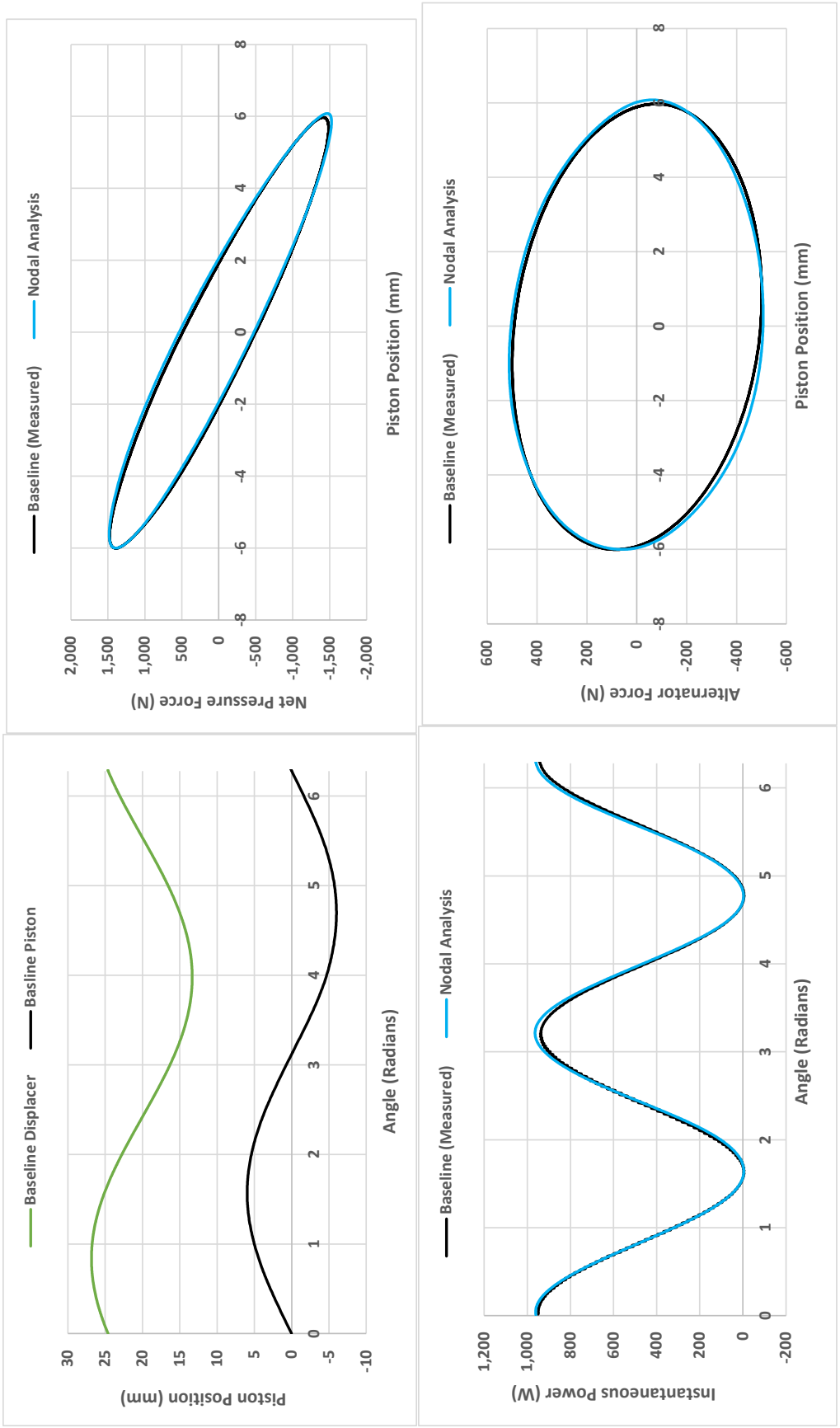

Figure 36 – Measured and predicted piston position, instantaneous power, and F-D diagrams for the baseline case (6 mm no harmonics)

Figure 36 shows that Sage slightly overpredicts the piston power based on alternator force, net pressure force, and instantaneous power output. However, the net power output of the engine reported in Table V shows a slight underprediction of thermodynamic/piston power output. This is due to the fact that the model is being run using displacer position as an input, requiring a small amount of power to achieve the prescribed displacer motion. When the displacer power is subtracted from the piston power the result is a slight underprediction of power output. There is a discrepancy of 6.4 % between the measured electric power and the calculated thermodynamic power (464 W calculated vs. 435 W measured). This could be the result of neglecting all alternator losses other than resistive losses, neglect of motor constant change with temperature, neglect of alternator resistance change with temperature, or inaccuracy introduced by filtering the position signal prior to calculating piston velocity and acceleration.

Figure 37 shows the piston position, instantaneous power, and force-displacement diagrams for the case of a 45 V 2nd harmonic on the AC bus. In this case the piston increases its inward travel and travels more slowly near its out-limit. The change in displacer motion is not clearly visible in Figure 37 but an increase in the out-limit of displacer motion was measured as 0.2 mm. The net pressure force chart shows that nodal analysis predicts increased power as a result of increased inward piston travel *and* higher net pressure force during compression. Measured data also shows an increase in piston power resulting from an increase in inward piston travel, but shows no measureable increase net pressure force during compression. Table VI shows the cyclic steady-state values of the 45 V 2nd harmonic point alongside the baseline point and Sage

predictions. The data shows a 6% increase in measured thermodynamic power output over the baseline case as measured by alternator electric power plus resistive losses, it also shows a 5% increase in usable electric power measured at the alternator leads. The gross efficiency was reduced from 0.262 in the baseline case to 0.258. There is again good agreement between power output predicted by Sage and those calculated from experimental values, but there remains a discrepancy between calculated values and the more direct electric power measurements.

Table VI - Cyclic steady-state data for the 45 V 2nd harmonic, nodal analysis (Sage), and baseline data

	Alternator Power (W)	Post-Cap Power (W)	Alt Power + Resistive Loss (W)	Net Pressure Power (W)	Alternator Force Power (W)	$I*V_{EMF}$ Power (W)	Gross Eff (%)	Net Eff (%)
Baseline	411	411	435	463	463	467	26.2	
45 V 2nd Harmonic	432	434	463	493	498	502	25.8	
Sage	473	473	504	504	504	504		33.6

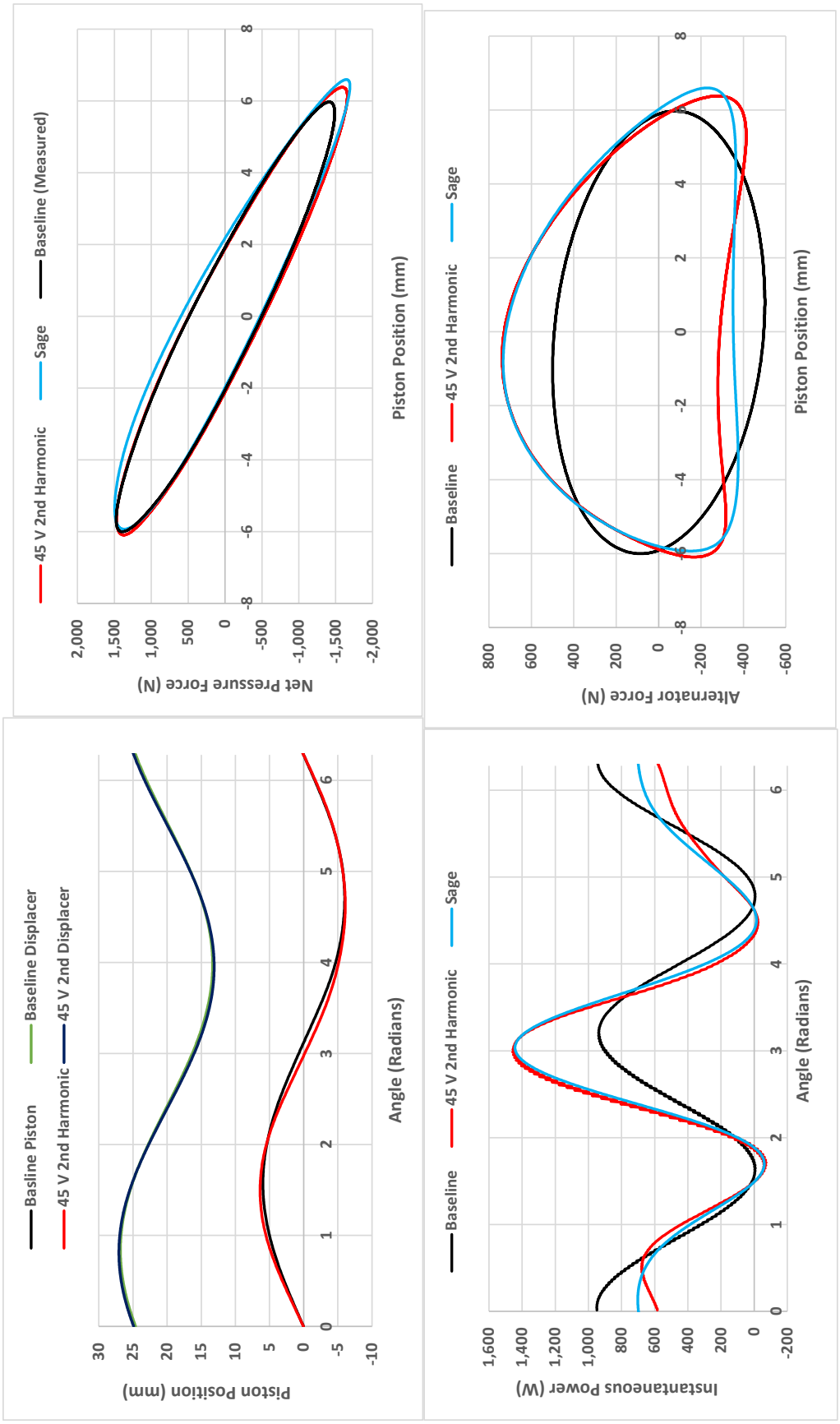

Figure 37- Piston position, instantaneous power, and F-D diagrams for a 45 V 2nd harmonic. Nodal analysis (Sage) and Baseline data included for comparison.

Figure 38 shows the piston position, instantaneous power, and force-displacement diagrams for the 90 V second harmonic case. In this case the piston increases its inward travel toward the displacer and continues to slow toward its out-limit. The increase in displacer amplitude can now be seen, as the out-limit of displacer motion increases 0.5 mm compared to the baseline case. The net pressure F-D diagram shows a slight increase in net pressure force during compression, but not to the extent predicted by nodal analysis. Table VII shows the cyclic steady-state values of the 90 V 2nd harmonic point alongside the baseline point and Sage predictions. This point shows a 12% increase in thermodynamic power output compared to the baseline case. The increased current required to produce the waveform increases the resistive losses, resulting in a 6% increase in usable power measured at the alternator. The gross efficiency decreased was reduced from 0.262 in the baseline case to 0.250.

Table VII - Cyclic steady-state data for the 90 V 2nd harmonic, nodal analysis (Sage), and baseline data

	Alternator Power (W)	Post-Cap Power (W)	Alt Power + Resistive Loss (W)	Net Pressure Power (W)	Alternator Force Power (W)	$I*V_{EMF}$ Power (W)	Gross Eff (%)	Net Eff (%)
Baseline	411	411	435	463	463	467	26.2	
90 V 2nd Harmonic	437	438	488	550	550	549	25.0	
Sage	506	506	552	552	552	552		33.7

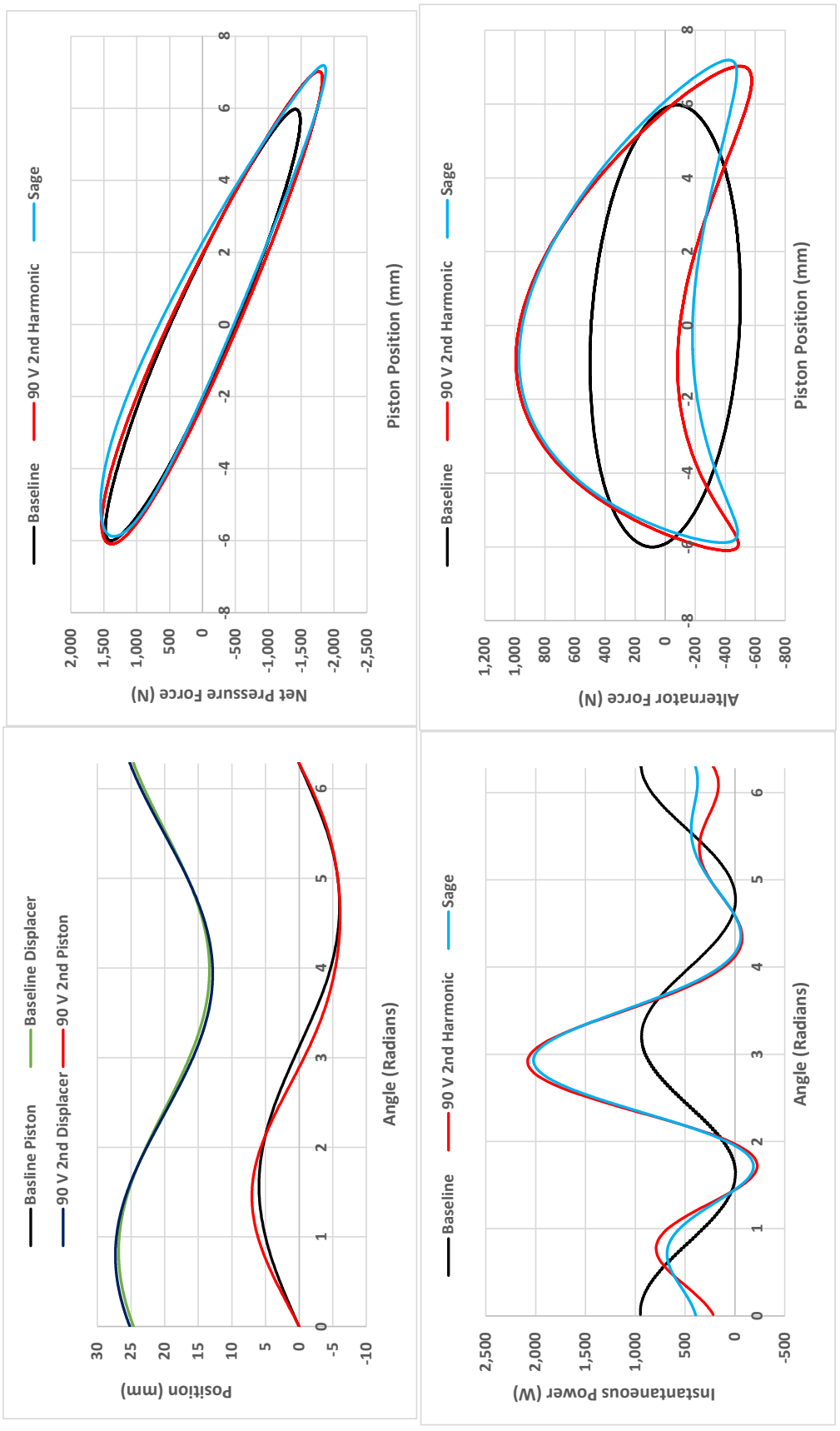

Figure 38 - Piston position, instantaneous power, and F-D diagrams for a 90 V 2nd harmonic. Nodal analysis (Sage) and Baseline data included for comparison.

Figure 39 shows the piston position, instantaneous power, and force-displacement diagrams for the 110 V second harmonic case. The piston travels further inward and slows more toward the out-limit of travel. The displacer amplitude again increases resulting in an out-limit of piston motion that is 0.65 mm further out than the baseline case. The net pressure F-D diagram shows a more substantial increase in the net pressure force during cooling along with an increase in power from further inward travel of the piston. Table VIII shows the cyclic steady-state values of the 110 V 2nd harmonic point alongside the baseline point and Sage predictions. This point shows little improvement over the 90 V second harmonic point, also increasing thermodynamic power output 12% over the baseline point. The increased current required to produce the waveform further increases the resistive losses, resulting in only a 3% increase in alternator power, which is lower than the 90 V 2nd harmonic case. The gross efficiency decreased was reduced from 0.262 in the baseline case to 0.243. In this case, nodal analysis overpredicts even the more optimistic thermodynamic power calculations by about 2%. The discrepancy between calculated and measured thermodynamic power reaches 17% in this case.

Table VIII - Cyclic steady-state data for the 110 V 2nd harmonic, nodal analysis (Sage), and baseline data

	Alternator Power (W)	Post-Cap Power (W)	Alt Power + Resistive Loss (W)	Net Pressure Power (W)	Alternator Force Power (W)	$I*V_{EMF}$ Power (W)	Gross Eff (%)	Net Eff (%)
Baseline	411	411	435	463	463	467	26.2	
110 V 2nd Harmonic	425	421	487	569	569	567	24.3	
Sage	592	592	580	580	580	580		33.9

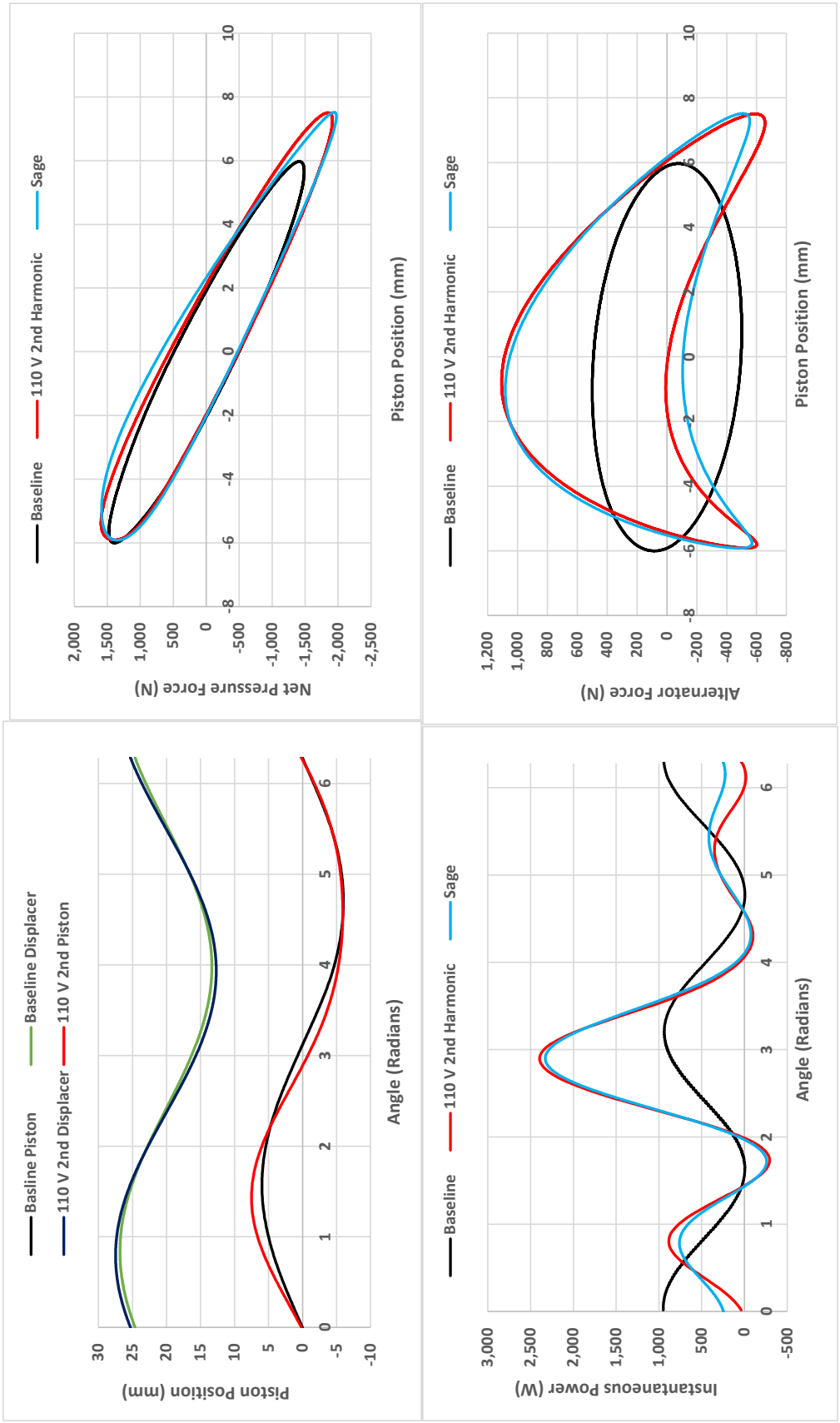

Figure 39 - Piston position, instantaneous power, and F-D diagrams for a 110 V 2nd harmonic. Nodal analysis (Sage) and Baseline data included for comparison.

Figure 40 shows the piston position, instantaneous power, and force-displacement diagrams for the 45 V third harmonic case. Since the tuning capacitors used in the control system are tuned to the first harmonic, the third harmonic is attenuated more than the second harmonic, so AC bus voltage increments of 45 V at the third harmonic produce less distortion of the waveform than 45 V increments on the second harmonic. As can be seen in Figure 40, this case deviates only slightly from sinusoidal motion. Despite the rather small distortion in the waveform, the alternator force F-D diagram shows substantial distortion from the baseline case, indicating that substantial spring force are required from the alternator to impose even modest third harmonic motion. The displacer outmost position increased .05 mm from the baseline case. Table IX shows the cyclic steady-state values of the 45 V third harmonic point alongside the baseline point and Sage predictions. Thermodynamic power, as measured by the alternator power plus resistive losses in the alternator increased 3.2%. The current required to produce this waveform is low enough to allow the increase in thermodynamic power to be seen at the alternator, resulting in an alternator power increase of 2.9%. Gross efficiency is reduced slightly, from 0.262 to 0.261.

Table IX - Cyclic steady-state data for the 45 V 3rd harmonic, nodal analysis (Sage), and baseline data

	Alternator Power (W)	Post-Cap Power (W)	Alt Power + Resistive Loss (W)	Net Pressure Power (W)	Alternator Force Power (W)	$I*V_{EMF}$ Power (W)	Gross Eff (%)	Net Eff (%)
Baseline	411	411	435	463	463	467	26.2	
45 V 3rd Harmonic	423	421	449	481	481	482	26.1	
Sage	449	449	476	476	476	476		33.4

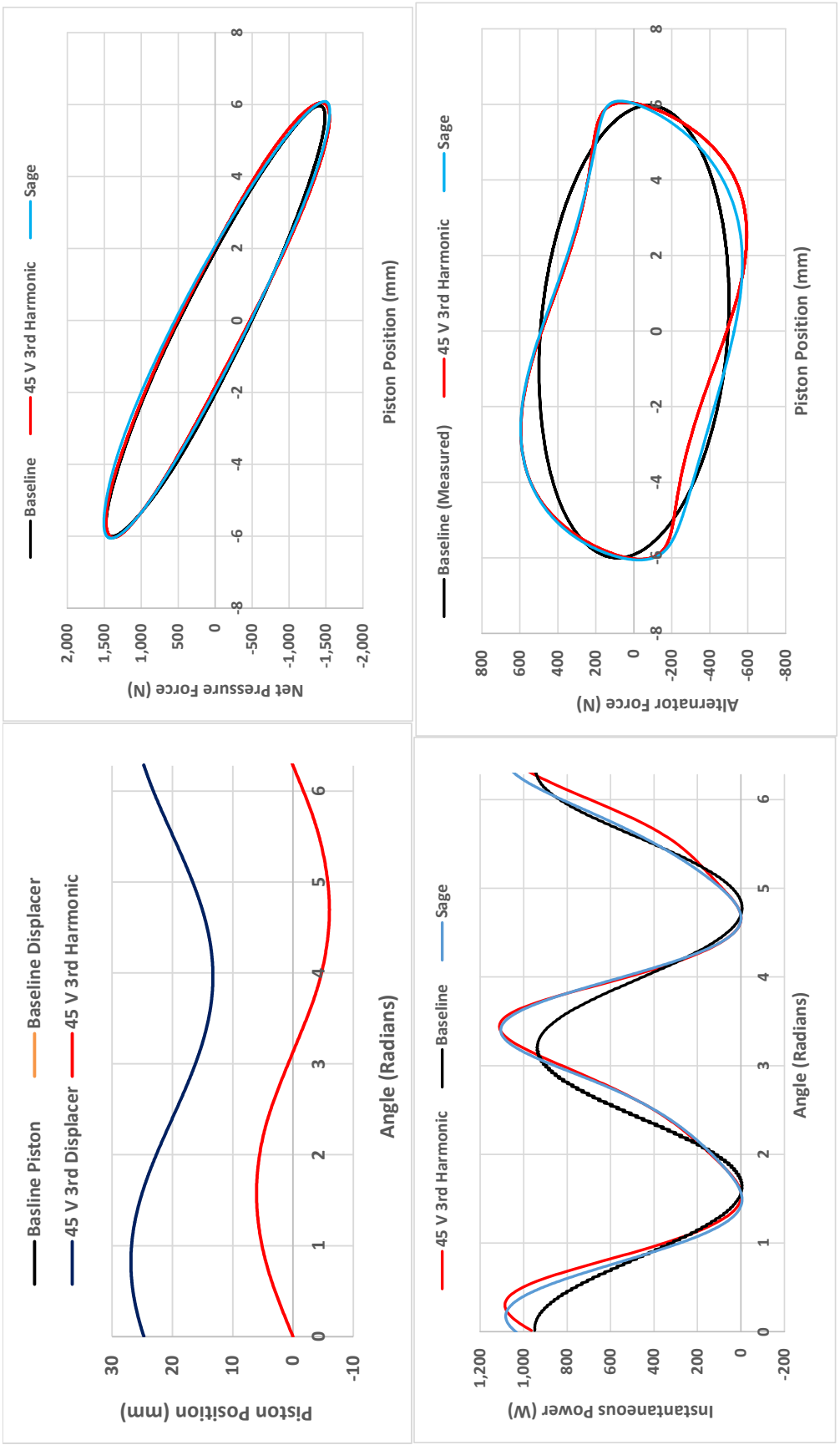

Figure 40 - Piston position, instantaneous power, and F-D diagrams for a 45V 3rd harmonic. Nodal analysis (Sage) and Baseline data included for comparison.

Figure 41 shows the piston and displacer position, instantaneous power, and force-displacement diagrams for the 90 V third harmonic case. The 90 V third harmonic case again produces small but measurable deviations from sinusoidal piston and displacer waveforms. The first harmonic of piston motion increases 0.2 mm from the baseline case and the displacer amplitude increases 0.12 mm. This relatively small change in the piston motion results in larger distortions in the force-displacement and instantaneous power plots, and measurable changes in power output. Table X shows the cyclic steady-state values of the 90 V third harmonic point alongside the baseline point and Sage predictions. This relatively small distortion in the waveform results in a 4% increase in the thermodynamic power and a 2% increase in the available electric power. Gross efficiency is reduced slightly, from 0.262 to 0.257

Table X - Cyclic steady-state data for the 90 V 3rd harmonic, nodal analysis (Sage), and baseline data

	Alternator Power (W)	Post-Cap Power (W)	Alt Power + Resistive Loss (W)	Net Pressure Power (W)	Alternator Force Power (W)	$I*V_{EMF}$ Power (W)	Gross Eff (%)	Net Eff (%)
Baseline	411	411	435	463	463	467	26.2	
90 V 3rd Harmonic	421	420	452	496	496	501	25.7	
Sage	460	460	491	491	491	491		33.5

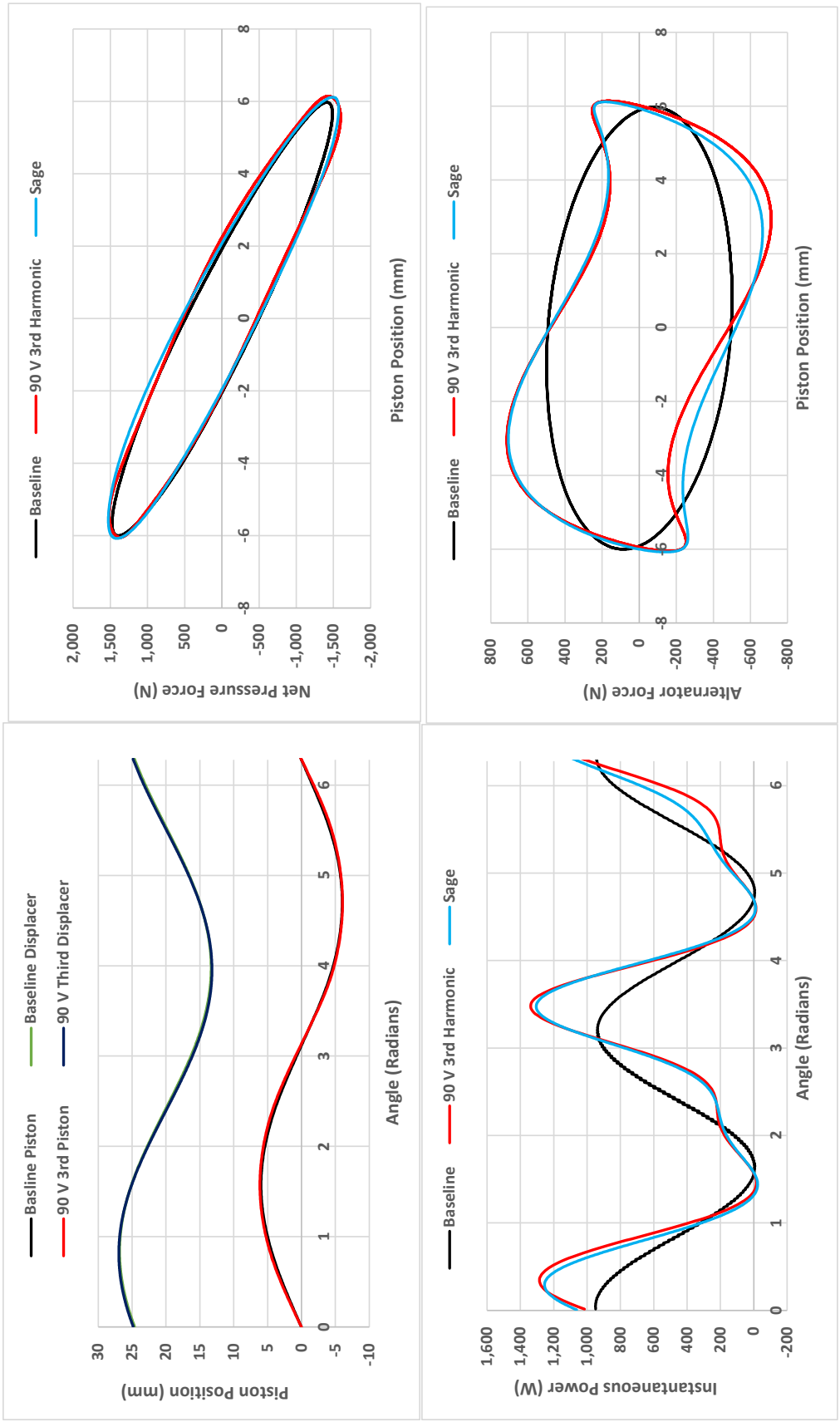

Figure 41 - Piston position, instantaneous power, and F-D diagrams for a 90 V 3rd harmonic. Nodal analysis (Sage) and Baseline data included for comparison.

Figure 42 shows the piston and displacer position, instantaneous power, and force-displacement diagrams for the 135 V third harmonic case. Table XI shows the cyclic steady-state values of the 135 V third harmonic point alongside the baseline point and Sage predictions. Indirect thermodynamic power calculation methods continue to indicate increasing power, but the direct method of adding resistive losses to the alternator power indicates a slight decrease in power output from the 90 V third harmonic case. The reduction in measured power output combined with an increase in the heat input requirement drives the gross efficiency down to 0.249. The discrepancy between the measured electric power and the calculated thermodynamic/piston power reaches 13%, compared to 5% in the baseline case.

Table XI - Cyclic steady-state data for the 135 V 3rd harmonic, nodal analysis (Sage), and baseline data

	Alternator Power (W)	Post-Cap Power (W)	Alt Power + Resistive Loss (W)	Net Pressure Power (W)	Alternator Force Power (W)	$I*V_{EMF}$ Power (W)	Gross Eff (%)	Net Eff (%)
Baseline	411	411	435	463	463	467	26.2	
135 V 3rd Harmonic	409	400	448	509	509	510	24.9	
Sage	468	468	505	505	505	505		33.7

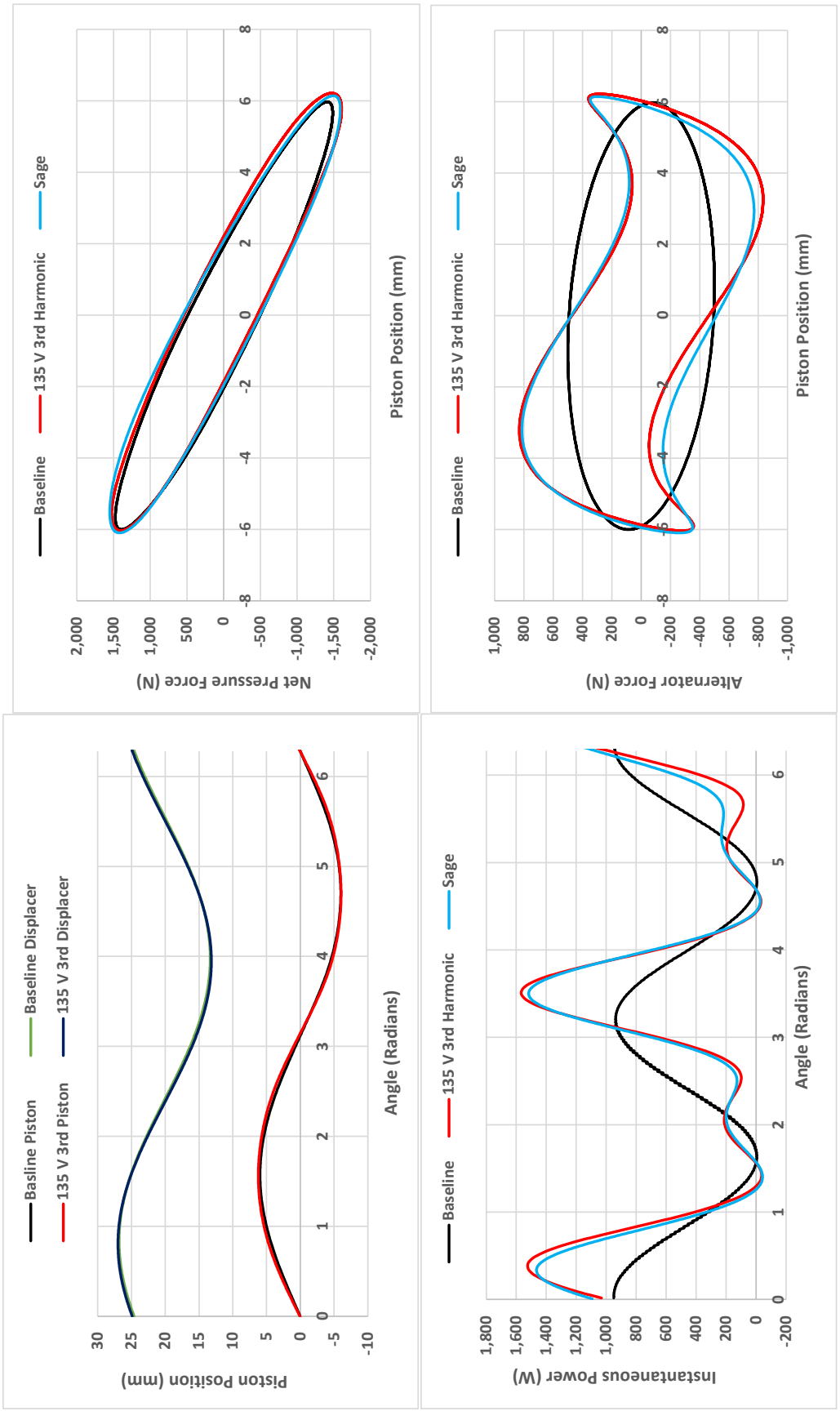

Figure 42 - Piston position, instantaneous power, and F-D diagrams for a 135 V 3rd harmonic. Nodal analysis (Sage) and Baseline data included for comparison.

Figure 43 shows the piston position, instantaneous power, and force-displacement diagrams for the 180 V third harmonic case. Table XII shows the cyclic steady-state values of the 180 V third harmonic point alongside the baseline point and Sage predictions. Indirect thermodynamic power calculation methods continue to show an increase in power output, while direct methods show decreasing power compared to the 90 and 135 V third harmonic cases. The reduction in measured power output combined with an increase in the heat input requirement drives the gross efficiency down to 0.239. The audible noise that stopped testing at a third harmonic voltage of 225 V could also be hear at the 185 V, although it was not recognized until after the 225 V point was attempted. Although the root cause of the noise remains unknown, it is a possible indication of additional loss mechanisms, not being taken into account in this analysis. Whatever the cause, it is clear that measured power diverges from analytically predicted power and calculated power this operating condition.

Table XII - Cyclic steady-state data for the 180 V 3rd harmonic, nodal analysis (Sage), and baseline data.

	Alternator Power (W)	Post-Cap Power (W)	Alt Power + Resistive Loss (W)	Net Pressure Power (W)	Alternator Force Power (W)	$I*V_{EMF}$ Power (W)	Gross Eff (%)	Net Eff (%)
Baseline	411	411	435	463	463	467	26.2	
180 V 3rd Harmonic	389	385	439	529	529	530	23.9	
Sage	473	473	519	519	519	519		33.7

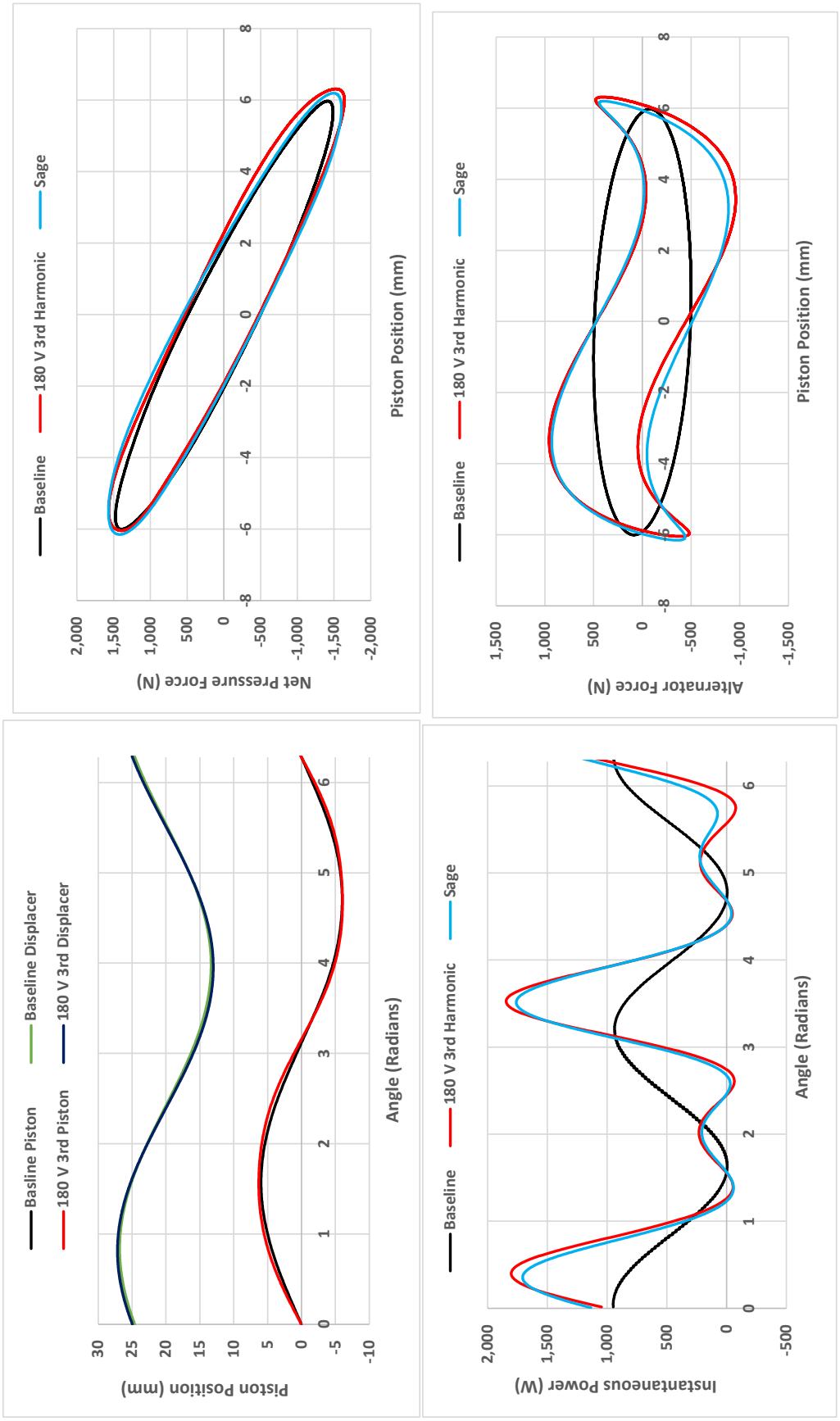

Figure 43 - Piston position, instantaneous power, and F-D diagrams for a 180 V 3rd harmonic. Nodal analysis (Sage) and Baseline data included for comparison.

Figure 44 shows the piston and displacer position, instantaneous power, and force-displacement diagrams for the 45 V 2nd harmonic and a 45 V 3rd harmonic case. Table XIII shows the cyclic steady-state values of the alongside the baseline point and Sage predictions. At these operating conditions thermodynamic power increases 9.9%, the usable electric power increases 8.2% with a small increase in gross efficiency to 0.263 from 0.262 in the baseline case. Displacer amplitude increase 0.3 mm.

Table XIII - Cyclic steady-state data for the 45 V 2nd harmonic and a 45 V 3rd harmonic case, nodal analysis (Sage), and baseline data

	Alternator Power (W)	Post-Cap Power (W)	Alt Power + Resistive Loss (W)	Net Pressure Power (W)	Alternator Force Power (W)	$I*V_{EMF}$ Power (W)	Gross Eff (%)	Net Eff (%)
Baseline	411	411	435	463	463	467	26.2	
45 V 2nd 45 V 3rd	445	444	478	519	519	519	26.3	
Sage	551	551	518	518	518	518		34.1

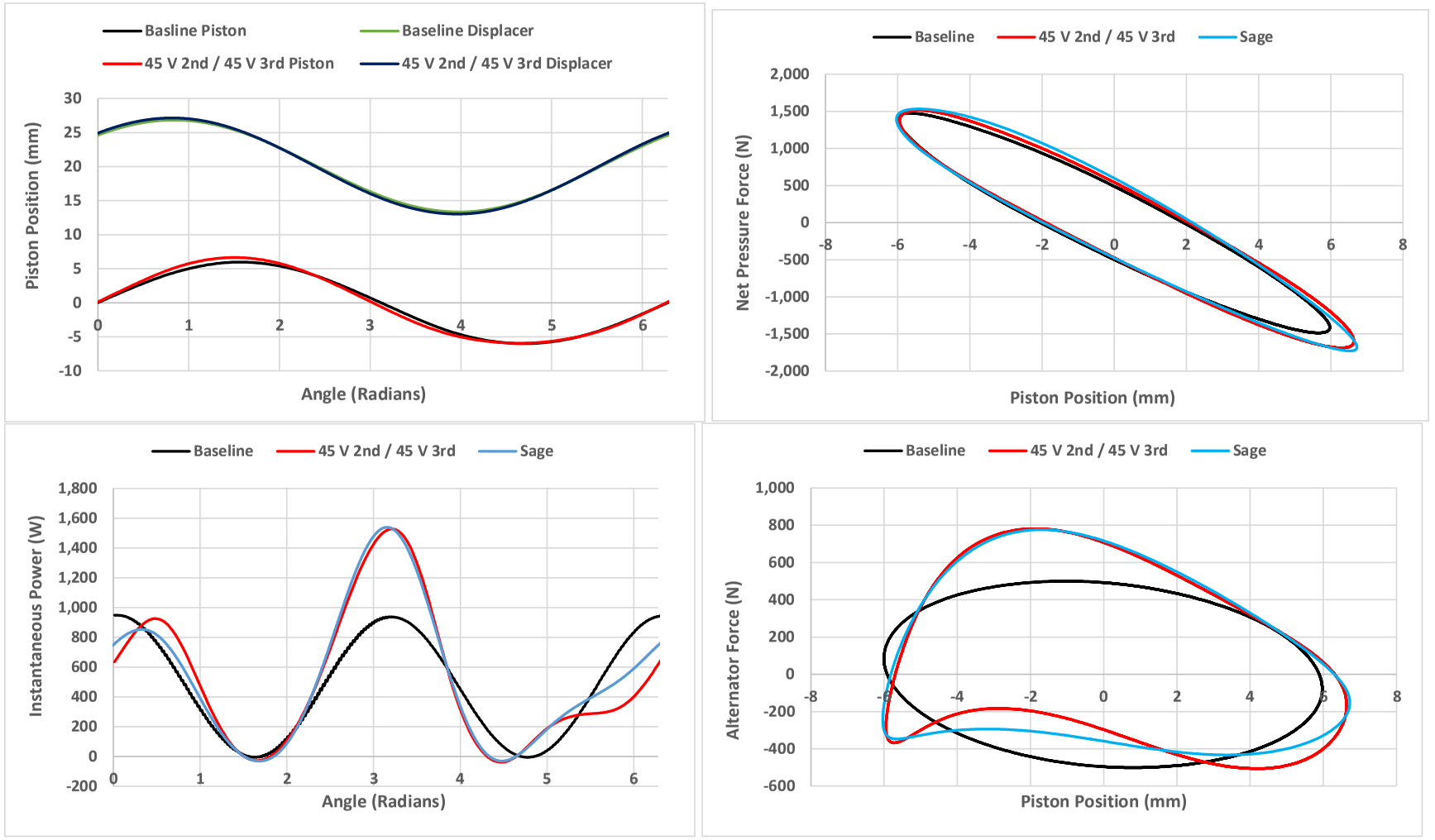

Figure 44 - Piston position, instantaneous power, and F-D diagrams for a 45 V 2nd 45 V 3rd harmonic. Nodal analysis (Sage) and Baseline data included for comparison.

Figure 44 shows the piston position, instantaneous power, and force-displacement diagrams for the 90 V 2nd harmonic and a 45 V 3rd harmonic case. Table XIII shows the cyclic steady-state values of the alongside the baseline point and Sage predictions. At these operating conditions thermodynamic power increases 11%, the usable electric power increases 5.5% from the baseline value. The gross efficiency decreases to 0.247 from 0.262 in the baseline case.

Table XIV - Cyclic steady-state data for the 90 V 2nd harmonic and a 45 V 3rd harmonic case, nodal analysis (Sage), and baseline data

	Alternator Power (W)	Post-Cap Power (W)	Alt Power + Resistive Loss (W)	Net Pressure Power (W)	Alternator Force Power (W)	$I*V_{EMF}$ Power (W)	Gross Eff (%)	Net Eff (%)
Baseline	411	411	435	463	463	467	26.2	
90 V 2nd 45 V 3rd	434	443	484	558	558	564	24.7	
Sage	525	525	573	573	573	573		33.9

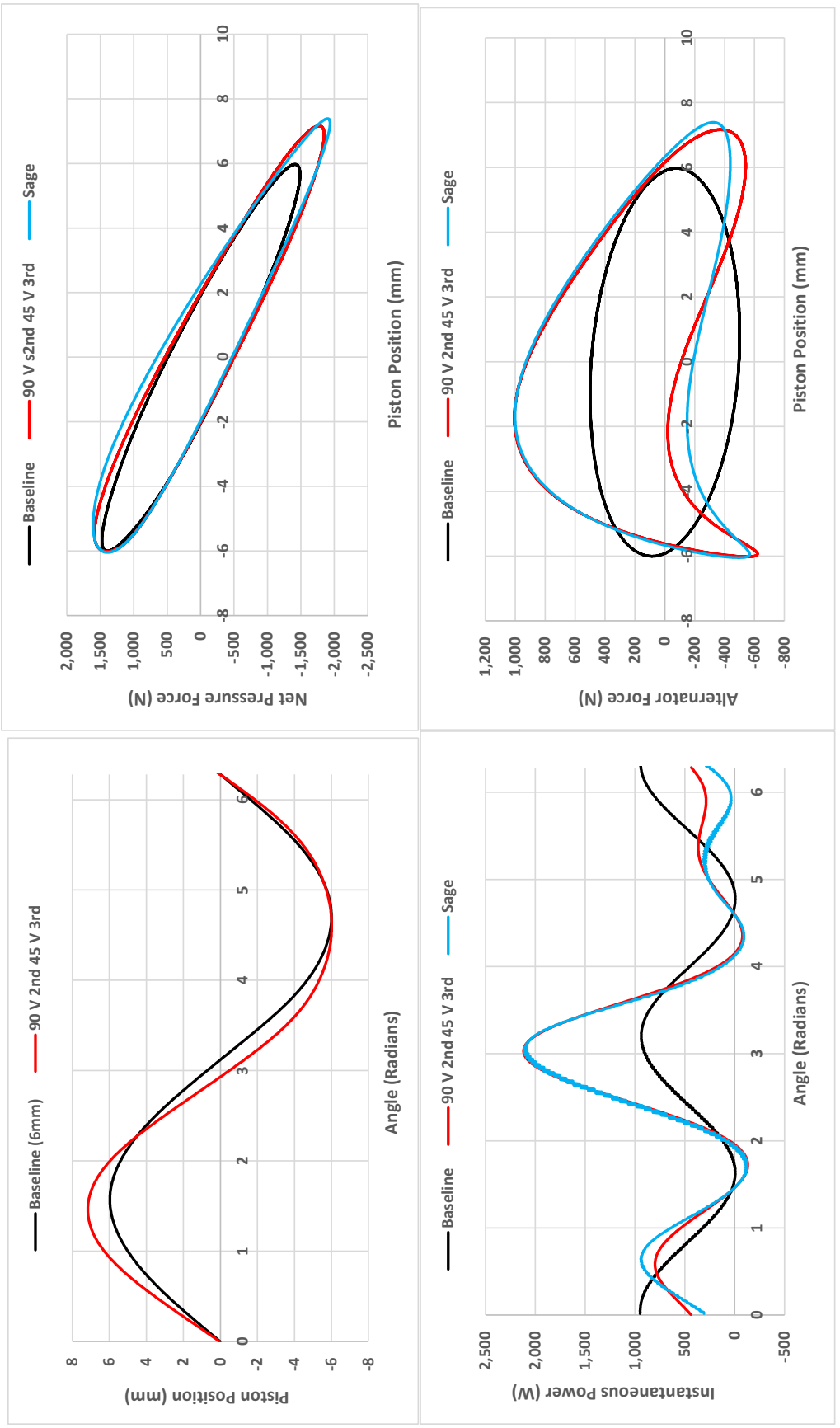

Figure 45 - Piston position, instantaneous power, and F-D diagrams for a 90 V 2nd Harmonic 45 V 3rd harmonic. Nodal analysis (Sage) and Baseline data included for comparison.

Figure 46 shows the piston position, instantaneous power, and force-displacement diagrams for the 110 V 2nd harmonic and a 45 V 3rd harmonic case. Table XV shows the cyclic steady-state values of the alongside the baseline point and Sage predictions. At these operating conditions thermodynamic power increases 12.4%, the usable electric power increases 3.9%. Gross thermal efficiency decreases to 0.237 from 0.262 in the baseline case.

Table XV - Cyclic steady-state data for the 110 V 2nd harmonic and a 45 V 3rd harmonic case, nodal analysis (Sage), and baseline data

	Alternator Power (W)	Post-Cap Power (W)	Alt Power + Resistive Loss (W)	Net Pressure Power (W)	Alternator Force Power (W)	$I*V_{EMF}$ Power (W)	Gross Eff (%)	Net Eff (%)
Baseline	411	411	435	463	463	467	26.2	
110 V 2nd 45 V 3rd	427	437	489	580	580	579	23.7	
Sage	544	544	602	602	602	602		33.9

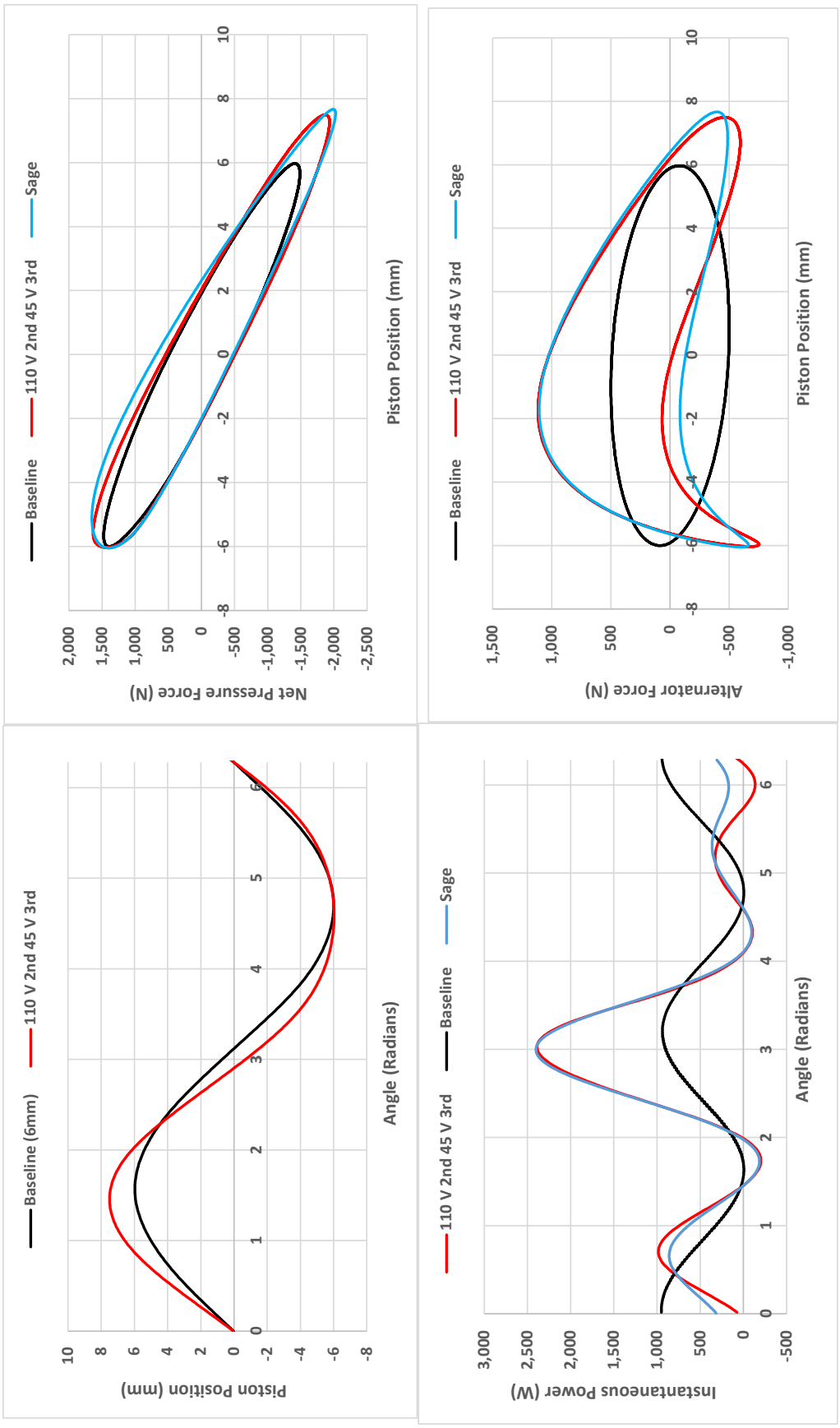

Figure 46 - Piston position, instantaneous power, and F-D diagrams for a 110 V 2nd Harmonic 45 V 3rd harmonic. Nodal analysis (Sage) and Baseline data included for comparison.

Figure 46 shows the piston position, instantaneous power, and force-displacement diagrams for the 45 V 2nd harmonic and a 90 V 3rd harmonic case. Table XV shows the cyclic steady-state values of the alongside the baseline point and Sage predictions. At these operating conditions thermodynamic power increases 11%, the usable electric power increases 8.3%. Gross thermal efficiency decreases to 0.258 from 0.262 in the baseline case. The discrepancy between calculated power and electric power measured either at the alternators or post-capacitor increases to 12%.

Table XVI - Cyclic steady-state data for the 45 V 2nd harmonic and a 90 V 3rd harmonic case, nodal analysis (Sage), and baseline data

	Alternator Power (W)	Post-Cap Power (W)	Alt Power + Resistive Loss (W)	Net Pressure Power (W)	Alternator Force Power (W)	$I*V_{EMF}$ Power (W)	Gross Eff (%)	Net Eff (%)
Baseline	411	411	435	463	463	467	26.2	
45 V 2nd 90 V 3rd	445	449	483	541	538	541	25.8	
Sage	504	504	541	541	541	541		33.9

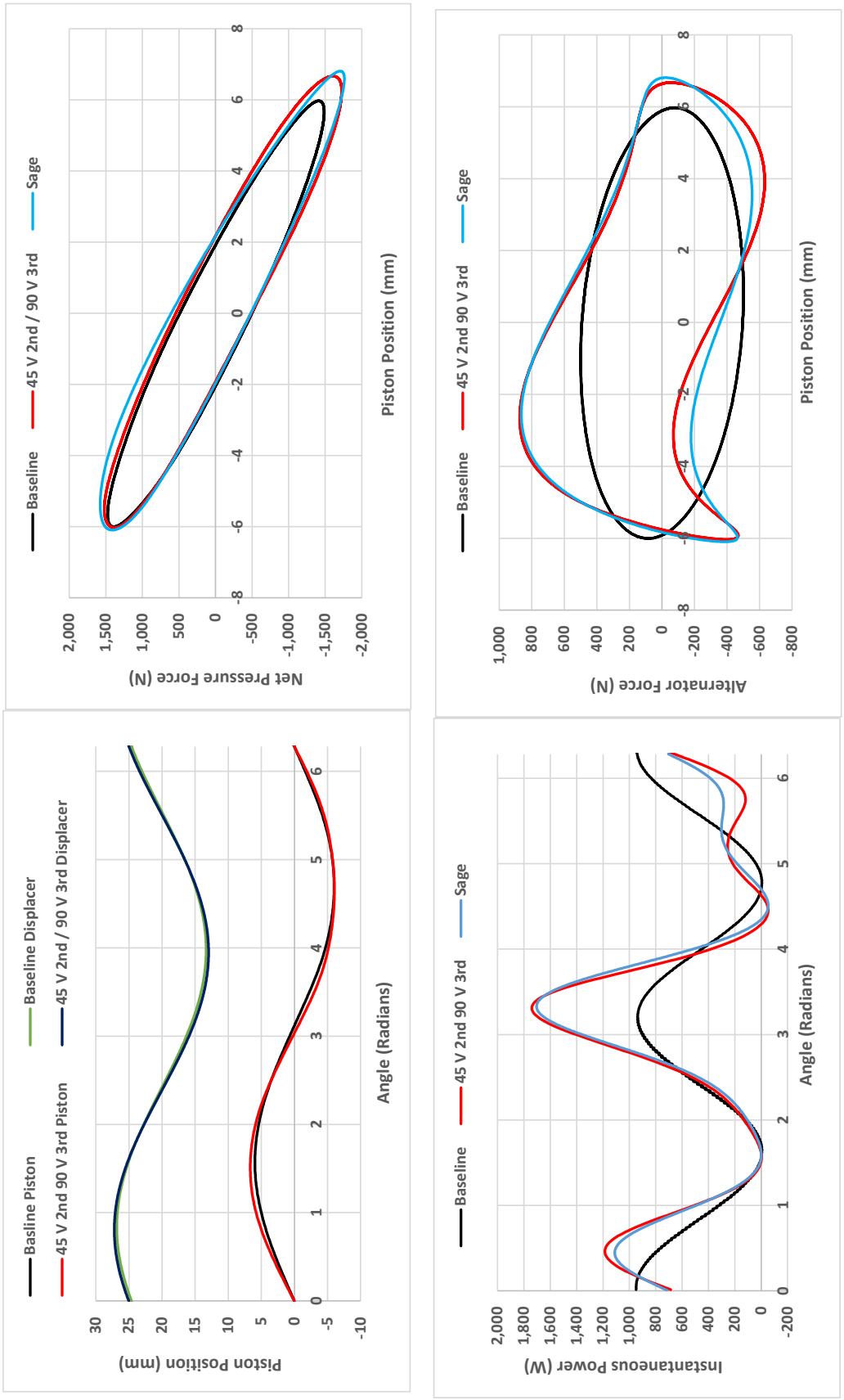

Figure 47 - Position, instantaneous power, and F-D diagrams for a 45 V 2nd Harmonic 90 V 3rd harmonic. Nodal analysis (Sage) and Baseline data included for comparison.

Figure 46 shows the piston position, instantaneous power, and force-displacement diagrams for the 90 V 2nd harmonic and a 90 V 3rd harmonic case. Table XV shows the cyclic steady-state values of the alongside the baseline point and Sage predictions. At these operating conditions thermodynamic power increases 9.7%, the usable electric power increases 6.8%. Gross thermal efficiency decreases to 0.245 from 0.262 in the baseline case.

Table XVII - Cyclic steady-state data for the 90 V 2nd harmonic and a 90 V 3rd harmonic case, nodal analysis (Sage), and baseline data

	Alternator Power (W)	Post-Cap Power (W)	Alt Power + Resistive Loss (W)	Net Pressure Power (W)	Alternator Force Power (W)	$I*V_{EMF}$ Power (W)	Gross Eff (%)	Net Eff (%)
Baseline	411	411	435	463	463	467	26.2	
90 V 2nd 90 V 3rd	439	451	494	583	583	582	24.5	
Sage	546	546	599	599	599	599		34.0

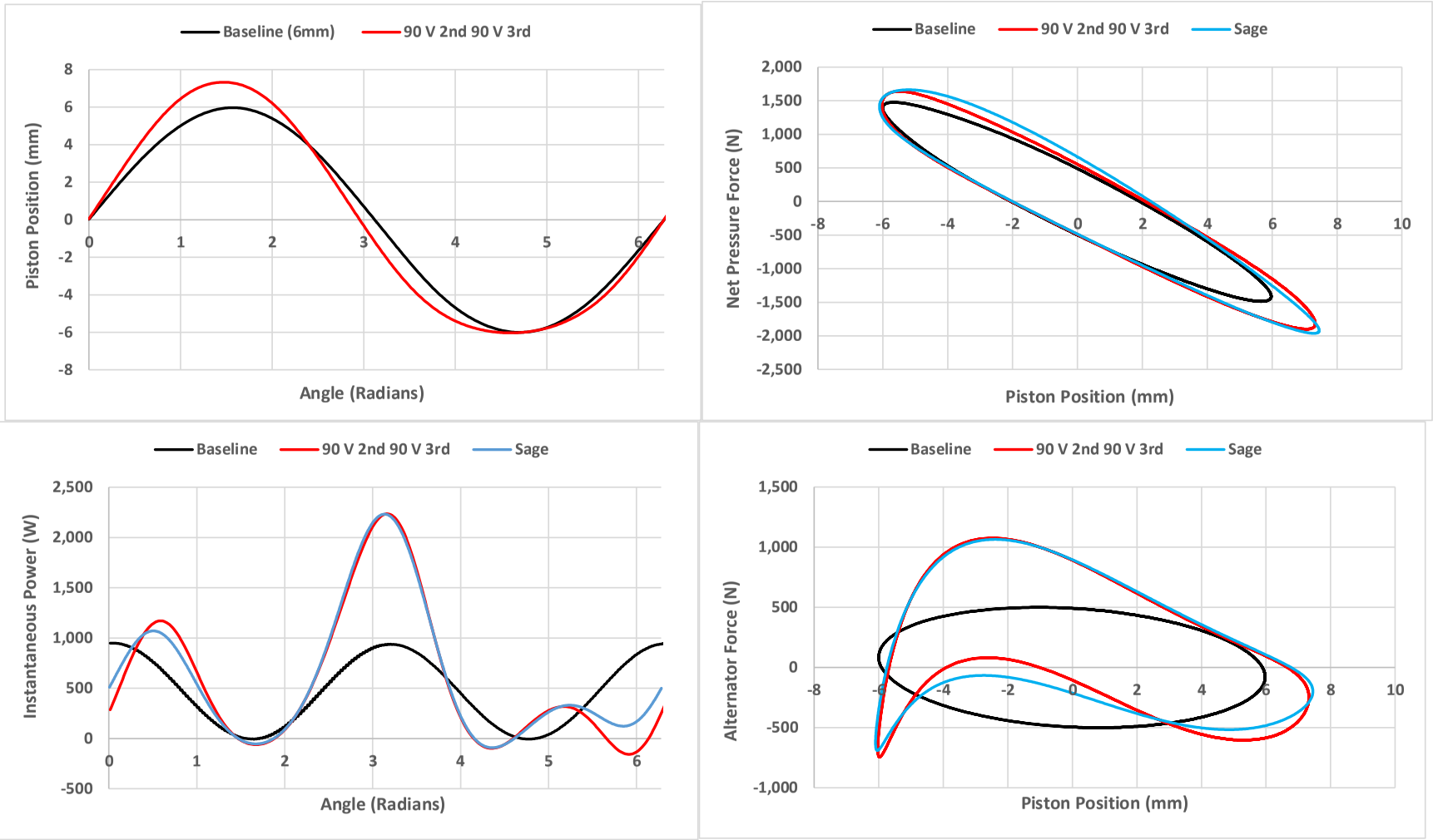

Figure 48 - Piston position, instantaneous power, and F-D diagrams for a 90 V 2nd Harmonic 90 V 3rd harmonic. Nodal analysis (Sage) and Baseline data included for comparison.

Figure 49 shows the trend in piston power, as measured by the electric power output plus the alternator resistive losses, versus the second harmonic voltage for constant third harmonic voltage. Increasing the third harmonic voltage from 0 V to 45 V is most beneficial at low second harmonic voltage. As the second harmonic voltage increases, the power output becomes less sensitive to increases in both the second and third harmonic voltage. The maximum piston power increase of 13.6% is achieved at a 90 V second harmonic and 90 V third harmonic.

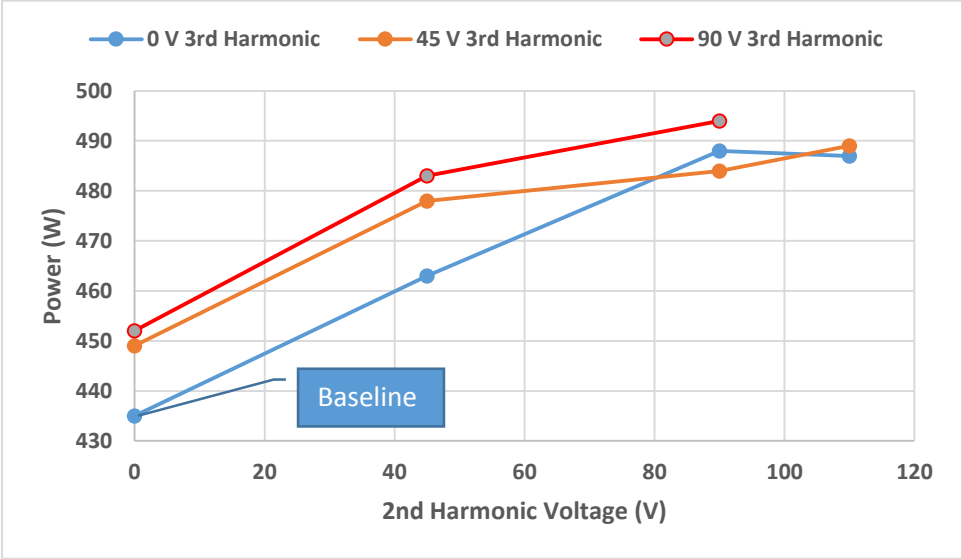

Figure 49 – Measured piston power versus 2nd harmonic voltage for 0, 45, and 90 V third harmonics

Figure 50 shows the trend in piston power, as measured by the electric power output plus the alternator resistive losses, versus the third harmonic voltage for constant second harmonic voltage. The zero volt second harmonic case shows a maximum power output at 90 V, with a piston power improvement of 3.7%. It is unknown whether the 45 V and 90 V second harmonic cases reach a maximum and at what voltage, due to restrictions on the test matrix described more completely in the Methodology section.

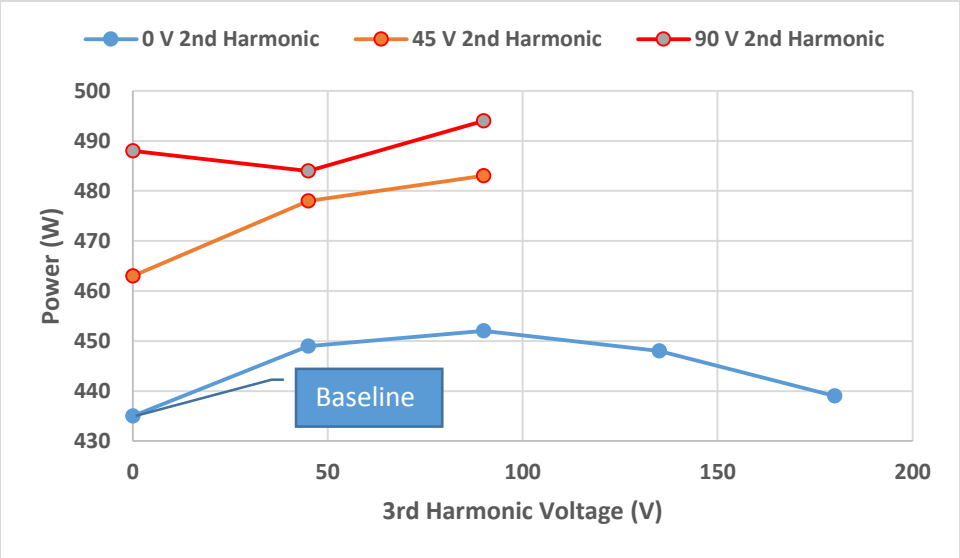

Figure 50 – Measured piston power versus 3rd harmonic voltage for 0, 45, and 90 V second harmonics

Figure 51 and Figure 52 show that analytical predictions are in close agreement with thermodynamic power as calculated by integrating the net pressure force with respect to piston position through a cycle, but diverge quantitatively and qualitatively from the direct electrical measurement of power. The measured values reported in Figure 51 and Figure 52 take the directly measured alternator power and add the resistive losses based on measured alternator current and resistance. This method assumes that other alternator loss mechanisms can be neglected. The method used for the calculated values is to solve for pressure forces using piston acceleration (based on measured position) and alternator force (based on measured current). This calculation is described in more detail in the Methodology section. This net-pressure force calculation assumes that the only forces acting on the piston are pressure forces and inertial forces, alternator forces, and that these alternator forces are equal to the alternator current times the measured motor constant (123 N / Amp). It may be possible to resolve the discrepancy between the

measured and calculated with in-depth analysis of alternator losses or with direct measurement of dynamic pressure, but these methods are outside of the scope of this project and are left to future work.

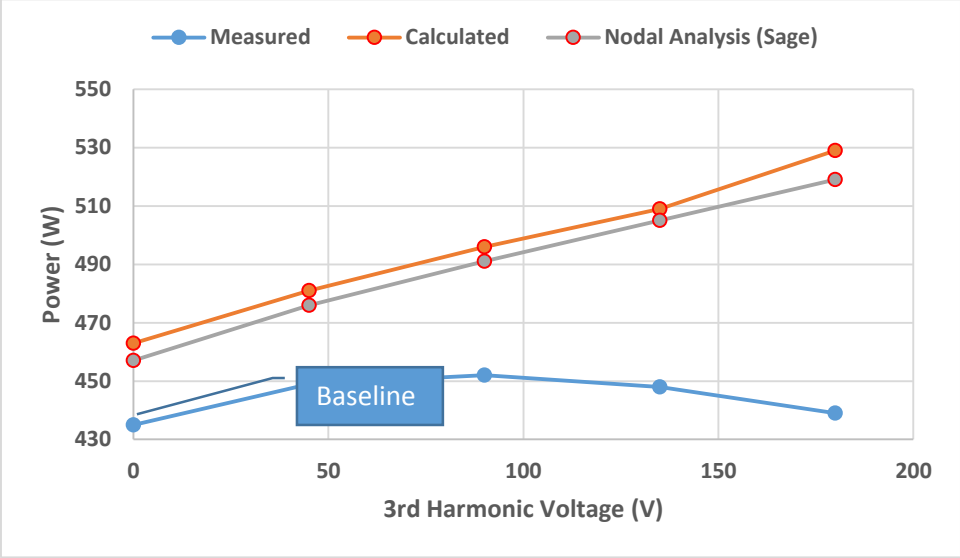

Figure 51 – Measured, Calculate, and Sage Predicted piston power versus 3rd harmonic voltage for the 0 V second harmonic case

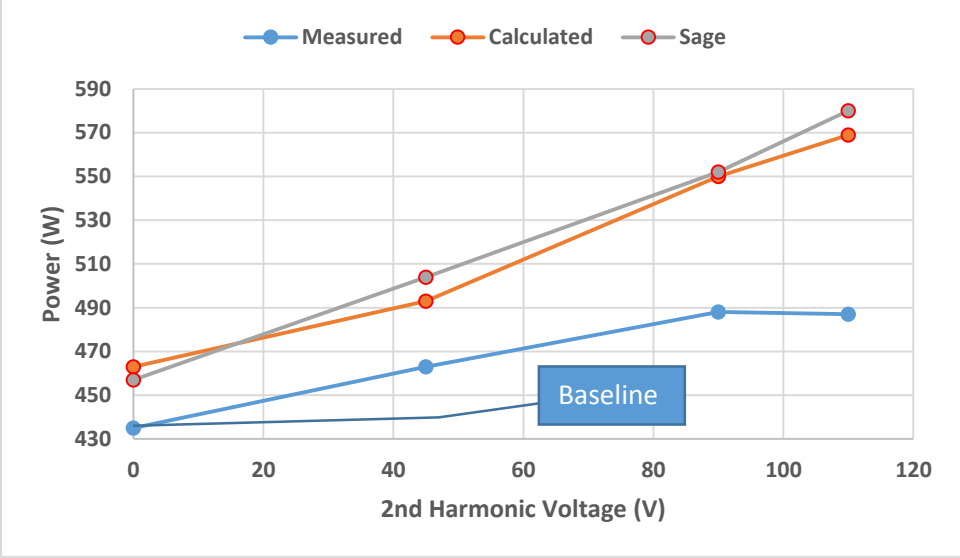

Figure 52 – Measured, Calculate, and Sage Predicted piston power versus 3rd harmonic voltage for the 0 V third harmonic case

Discussion of Results

This experiment shows that second and third harmonic waveforms can be superimposed on the single harmonic piston waveforms typically used on Stirling engines. Higher harmonic waveforms with correct phasing are shown to increase both thermodynamic power and, in some cases, usable electric power. The engines chosen for testing (and the vast majority of free-piston Stirling engine designs) have no mechanism available for controlling displacer motion, so optimized displacer waveforms could not be imposed, and displacer amplitude could not be limited. The resulting free-displacer motion is very close to sinusoidal and in many cases increases the out-limit of displacer motion during higher harmonic testing beyond the out-limit of displacer motion measured during the sinusoidal baseline test. Therefore, the increase in piston power measured during this test does not necessarily prove an increase in power density because the engine would have to grow to accommodate the displacer motion. Furthermore, since increased displacer amplitude can lead to increased power output, in the absence of changes to the piston waveform, it is not clear how much of the power output increase measured during testing can be directly attributed to altering the piston waveforms, and what portion should be attributed to the increase in displacer amplitude. However, since the displacer is a passive component, driven by the pressure differential between the bounce space and the workings space, the increased amplitude is itself an indication of increased pressure forces and increased power output caused by higher harmonic piston motion.

The thermodynamic power, calculated by several methods described in the Methodology section is in close agreement with analytical results provided by the Sage

nodal analysis tool. However, thermodynamic power calculated by adding resistive alternator losses to the measured alternator power is consistently lower than calculated values and Sage predictions. This could be an indication of an inadequate alternator loss model or a breakdown of the assumptions going into the thermodynamic power calculations. Future work could address this discrepancy by developing a comprehensive alternator model and/or including a dynamic pressure measurement so that the thermodynamic power can be measured directly. In the event that future work shows Sage predictions and calculated thermodynamic power to be accurate, it will still be necessary to understand the loss mechanisms that prevent the thermodynamic power being measured at the alternator leads.

Numerical optimization, using the Sage nodal analysis tool, identified a second piston position harmonic of $-\pi/2$ and a third piston position harmonic phase angle of zero as producing the maximum increase in power output. These were the only phase angles tested in this test experiment. Future work could identify other optimal waveforms based on other objective functions. Alternatively, a more Edisonian approach could be used in which the entire range of possible phase angles is explored observing their effects on power density and efficiency. This method would eliminate the need for accurate nodal analysis.

Conclusion

Isothermal analysis of ideal engines shows that the use of ideal piston and displacer waveforms increases Stirling engine power density. The degree of the increase depends on the method of constraint, but is found, in all cases to be proportional to the

natural logarithm of the working space volume ratio. Isothermal analysis of more realistic engines with dead volume shows that Stirling engines operating with ideal piston and displacer waveforms could increase power output 50% - 315% depending on the method of constraint. Nodal analysis shows that loss mechanisms not taken into account in isothermal analysis reduce the power output expected from ideal waveforms, often times below the power output expected from sinusoidal motion. Numerical optimization shows that piston and displacer waveforms that compromise between the benefits of ideal motion and the reduced losses of sinusoidal motion can be used to increase power output by as much as 58%, depending on the method of constraint. Experimental data shows that engines operating with same out-limit of piston motion can be made to produce as much as 14% additional thermodynamic power by superimposing a second and third harmonic on the original sinusoidal piston waveform. Since the engines are not designed to operate at higher harmonics, relatively high currents are required to achieve the desired waveforms, resulting in increased resistive losses and a maximum usable electric power increase of 8.3%.

Outline of Future Work

- Analytical
    - Optimize waveforms based on alternative objective functions such as efficiency, or minimize temperature required to produce the required power.
    - Resolve discrepancy between measured electrical power and calculated thermodynamic power.
    - Determine potential benefits of including piston and displacer waveforms in the trade space during engine design.

- Determine system level benefits of increased power density in specific Stirling engine applications.

- Experimental
  - Resolve the discrepancy between calculated thermodynamic power and electrical power by including a dynamic pressure measurement.
  - Explore a more comprehensive range of phase angles and waveforms. This could identify high efficiency waveforms, or high power waveforms not identified by nodal analysis.
  - Include higher harmonics.
  - Test engines that are capable of imposing desired waveforms on both the piston and displacer.
- Hardware
  - Create a more sophisticated control system capable of reducing voltage and current requirements.
  - Design mechanisms to impose the desired waveforms on the piston and displacer without increasing alternator force / current

Appendix I

Isothermal Analysis of Stirling Engines

Ideal Stirling Analysis

The thermodynamic solution of the ideal Stirling engine is well known and can be readily found in Stirling cycle literature (references here). It is repeated herein to aid in the verification of the results presented within the main text. The analysis begins with the most general case of an ideal Stirling engine, allowing for dead volume and imperfect regeneration. Simplification will then be made to analyze cases of zero dead volume and perfect regeneration. This analysis makes no assumptions about the configuration of the engine and can be applied equally to either the alpha or beta-configurations.

The working space volume is defines as:

$$V_{WS} = V_{CS} + V_C + V_R + V_H + V_{ES}$$

Where V is the instantaneous volume in a given gas space and the subscripts WS, CS, C, R, H, and ES refer to the working space, compression space, cooler, regenerator, heater and expansion space, respectively. It is convenient to combine any volume that remains constant throughout the cycle (including clearance volumes in the compression and expansion spaces) into a single parameter referred to as the dead volume:

$$V_D = V_{CS,Cl} + V_C + V_R + V_H + V_{ES,Cl}$$

Where the subscript Cl denotes a clearance volume not traversed by either the compression or expansion piston. The working space volume can then be rewritten as:

$$V_{WS} = V_{CS,Active} + V_D + V_{ES,Active} \qquad (A1.0)$$

Where the subscript, Active, denotes the instantaneous volume of the portion of the gas space that is traversed by one of the pistons. Referring to Figure 1 in the main text, $V_{ES,Active}$ is equal to zero during the compression process 1-2 and $V_{CS,Active}$ is equal to zero during the expansion process 3-4.

Assuming no gas leakage from the working volume and the general Stirling engine layout shown in Figure 16 in the main text, which includes the heater and cooler, the total gas inventory in a Stirling engine is given by:

$$M_{tot} = m_{CS} + m_C + m_R + m_H + m_{ES} \qquad (A1.1)$$

Where m is the instantaneous gas mass in a given component. Assuming that the working fluid behaves as an ideal gas and the instantaneous pressure throughout the working space is constant (no pressure drop across components) gives:

$$M_{tot} = \frac{P}{R}\left(\frac{V_{CS,Active}}{T_{CS}} + \frac{V_{CS,Cl}}{T_{CS}} + \frac{V_C}{T_C} + \frac{V_R}{T_{R,Eff}} + \frac{V_H}{T_H} + \frac{V_{ES,Cl}}{T_{ES}} + \frac{V_{ES,Active}}{T_{ES}}\right) \qquad (A1.2)$$

Where P is the instantaneous pressure in the working volume, R is the gas constant of the working fluid, V is the instantaneous volume, T is the instantaneous temperature within a given fluid volume, for isothermal analysis temperatures are constant in time but vary across components. The effective regenerator temperature $T_{R,Eff}$ can be determined by assuming a linear temperature profile in the regenerator with a minimum temperature

equal to the cooler temperature and a maximum temperature equal to the heater temperature giving:

$$m_{Reg} = \int_0^{V_{Reg}} \rho dV = \frac{A_R P}{R} \int_0^{L_R} \frac{1}{(T_H - T_C)\frac{x}{L_R} + T_C} dx = \frac{V_R P}{R} \left(\frac{\ln\left(\frac{T_H}{T_C}\right)}{T_H - T_C} \right) \quad \text{(A1.3)}$$

$$T_{R,Eff} \equiv \left(\frac{T_H - T_C}{\ln\left(\frac{T_H}{T_C}\right)} \right) \quad \text{(A1.4)}$$

The net cycle work can be calculated by taking the cyclic integral of P dV in the working space. Since there is no work done during the isochoric processes the cyclic integral can be represented as the sum of the work done during compression and expansion:

$$W_{net} = \int_{V_1}^{V_2} P \, dV_{WS} + \int_{V_3}^{V_4} P \, dV_{WS} \quad \text{(A1.5)}$$

Where V_1, V_2, V_3, and V_4 are the working space volumes at the end of cooling, compression, heating, and expansion respectively (Figure 1). For ideal piston motion V_2 is equal to V_3 and V_1 is equal to V_4.

Realizing that the active expansion space volume is zero during compression and the active compression space volume is zero during expansion and substituting Equation A1.2 into A1.5. gives:

$$W_{net} = \left(\int_{V_1}^{V_2} \frac{M_{tot} R \, T_{CS}}{(V_{CS,Active} + T_{CS} C_1)} dV \right)_{WS} + \left(\int_{V_2}^{V_1} \frac{M_{tot} R \, T_{ES}}{(V_{ES,Active} + T_{ES} C_1)} dV \right)_{WS}$$

$$C_1 = \left(\frac{V_{CS,Cl}}{T_{CS}} + \frac{V_C}{T_C} + \frac{V_R}{T_{Eff\,R}} + \frac{V_H}{T_H} + \frac{V_{ES,Cl}}{T_{ES}} \right)$$

Substituting A1.0 into the above equation and again recognizing that the active compression space volume equals zero during expansion and that the active expansion space volume is zero during compression gives:

$$W_{net} = \left(\int_{V_1}^{V_2} \frac{M_{tot} R\, T_{CS}}{(V_{WS} - V_D + T_{CS} C_1)} dV\right)_{WS} + \left(\int_{V_2}^{V_1} \frac{M_{tot} R\, T_{ES}}{(V_{WS} - V_D + T_{ES} C_1)} dV\right)_{WS}$$

Defining the Effective Dead Volume Temperature as:

$$T_{D,Eff} = \frac{V_D}{C_1}$$

Gives:

$$W_{net,Ideal} = \left(\int_{V_1}^{V_2} \frac{M_{tot} R\, T_{CS}}{(V_{WS} + V_D(\tau_d - 1))} dV\right)_{WS} + \left(\int_{V_2}^{V_1} \frac{M_{tot} R\, T_{ES}}{(V_{WS} + V_D(\tau\tau_d - 1))} dV\right)_{WS}$$

$$W_{net,ideal} = M_{tot} R T_{CS} \left[\tau \ln\left(\frac{r + K_d(\tau\,\tau_d - 1)}{1 + K_d(\tau\,\tau_d - 1)}\right) - \ln\left(\frac{r + K_d(\tau_d - 1)}{1 + K_d(\tau_d - 1)}\right)\right] \qquad (A.1.6)$$

$$r = \frac{V_1}{V_2} \qquad \tau = \frac{T_{ES}}{T_{CS}} \qquad K_d = \frac{V_D}{V_2} \qquad \tau_d = \frac{T_{CS}}{T_{D,Eff}}$$

This analysis predicts that the power density of the ideal cycle is a function of the four dimensionless parameters, volume ratio (r), temperature ratio (τ), dead volume ratio (K_d), and the dead volume temperature ratio (τ_d), and is independent of regenerator effectiveness.

The thermal efficiency of the ideal Stirling cycle can be calculated as the ratio of the net cycle work to the external heat input to the expansion space and heater. Applying conservation of energy of an open system to any of the gas volumes gives:

$$dU = \delta Q - \delta W + \left[(\dot{m}h)_{\text{Boundary 1}} + (\dot{m}h)_{\text{Boundary 2}}\right]dt \qquad \text{(A1.7)}$$

$$dm = (\dot{m}_{\text{Boundary 1}} + \dot{m}_{\text{Boundary 2}})dt$$

Analyzing the isothermal expansion space, assuming that the expansion space temperature is equal to the heater temperature reduces equation A1.7 to:

$$\delta Q_{ES} = \delta W_{ES} - RT_{ES}dm_{ES}$$

Taking the cyclic integral and assuming that the cycle has reached cyclic steady-state gives the following equation for heat transfer in the expansion space:

$$Q_{ES} = \oint P dV_{ES} \qquad \text{(A1.8)}$$

The heat transfer in the expansion space is therefore equal to the net work in the expansion space and can be calculated as:

$$Q_{ES} = \int_{V_{ES,1}}^{V_{ES,2}} P dV_{ES} + \int_{V_{ES,2}}^{V_{ES,3}} P dV_{ES} + \int_{V_{ES,3}}^{V_{ES,4}} P dV_{ES} + \int_{V_{ES,4}}^{V_{ES,1}} P dV_{ES}$$

$$P = MR\left(\frac{V_{CS,Active}}{T_{CS}} + \frac{V_D}{T_D} + \frac{V_{ES,Active}}{T_{ES}}\right)$$

Process 1-2 is the compression process in which the expansion space remains at constant volume, so there is no work done. Process 2-3 is the heating process in which the working space volume remains at its minimum value throughout. Process 3-4 is the

isothermal expansion process in which $V_{CS,Active}$ is zero. Process 4-1 is the cooling process in which the working space volume remains at its maximum value throughout. Using equation A1.0 and these constraints gives:

$$Q_{ES} = MRT_{ES}\left[\int_0^{V_{WS,min}-V_D} \frac{dV_{ES}}{V_{ES}(1-\tau)+\tau\left[V_D(\tau_D-1)+V_{WS,min}\right]} + \int_{V_{WS,min}-V_D}^{V_{WS,max}-V_D} \frac{dV_{ES}}{V_{ES}+V_D\tau\tau_D} + \int_{V_{WS,max}-V_D}^{0} \frac{dV_{ES}}{V_{ES}(1-\tau)+\tau\left[V_D(\tau_D-1)+V_{WS,max}\right]}\right]$$

Which, after a bit of simplification, gives:

$$Q_{ES} = \frac{MRT_{ES}}{\tau-1}\left[\tau \ln\left(\frac{r+K_d(\tau\,\tau_d-1)}{1+K_d(\tau\,\tau_d-1)}\right) - \ln\left(\frac{r+K_d(\tau_d-1)}{1+K_d(\tau_d-1)}\right)\right]$$

Analyzing the heater gas volume, which is both isochoric and isothermal, and considering imperfect regeneration for which the temperature of the gas entering the heater from the regenerator is lower than the temperature of the gas within the heater gives:

$$\delta Q_H = \oint \dot{m}_{H\_Reg}(C_v T_H - C_p T_{h,Reg})dt$$

Where T_h is piecewise defined by:

$$T_{h,reg} = \begin{cases} T_H, & \dot{m}_{H\_Reg} < 0 \\ T_C + \epsilon_h(T_H - T_C), & \dot{m}_{H\_Reg} \geq 0 \end{cases}$$

Where ε is the regenerator effectiveness on either the cold or hot side. The cyclic integral can then be taken to determine the heat requirement at the heater-regenerator boundary.

In the case of perfect regeneration $T_{h,reg}$ is equal to T_H throughout the cycle and the net heat requirement is zero at the boundary.

Similar analysis and conclusions apply to the cold side of the regenerator and the cooler, leading to the conclusion that, in an ideal Stirling engine with perfect regeneration, all heat transfer takes place within the compression and expansion spaces where work is being done on or by the working fluid. The heater and cooler are therefore unnecessary, hence many schematics of ideal Stirling engines do not include them, as shown in Figure 2 in the main text.

Ideal Stirling efficiency, allowing for dead volume and imperfect regeneration, can be calculated as the ratio of the net work (Eq. A1.6) to the external heat input. The external heat input of the Stirling cycle is equal to the sum of the net external heat input to the expansion space and the additional heat required by the heater due to imperfect regeneration:

$$\eta_{\text{Ideal Stirling}} = \frac{W_{\text{net}}}{Q_{\text{in,ext}}}$$

$$= \frac{M_{\text{tot}} R T_{CS} \left[\tau \ln\left(\frac{r + K_d(\tau\,\tau_d - 1)}{1 + K_d(\tau\,\tau_d - 1)}\right) - \ln\left(\frac{r + K_d(\tau_d - 1)}{1 + K_d(\tau_d - 1)}\right)\right]}{M_{\text{tot}} R T_{CS} \left(\frac{\tau}{\tau - 1}\right)\left[\tau \ln\left(\frac{r + K_d(\tau\,\tau_d - 1)}{1 + K_d(\tau\,\tau_d - 1)}\right) - \ln\left(\frac{r + K_d(\tau_d - 1)}{1 + K_d(\tau_d - 1)}\right)\right] + \oint \dot{m}_{H\_Reg}(C_v T_H - C_p T_{h,Reg})dt}$$

As the regenerator effectiveness approaches unity the second term in the denominator approaches zero and the above equation is simplified to:

$$\eta_{\text{Ideal Stirling}} = \frac{W_{\text{net}}}{Q_{\text{in}}} = \left(1 - \frac{1}{\tau}\right) = \eta_{\text{Carnot}} \qquad \text{(A1.9)}$$

This analysis shows that the efficiency of an ideal Stirling with perfect regeneration is not affected by dead volume and is equal to the Carnot efficiency.

Further restricting the scope of the analysis to an ideal Stirling engine with perfect regeneration and zero dead volume gives the following result:

$$W_{\text{Ideal Stirling}} = M_{tot} R T_{CS} \ln(r) (\tau - 1) \qquad \text{(A1.10)}$$

Equation A1.10 appears as equation 1 in the main text and is used as the basis for ideal Stirling power density comparisons.

Schmidt Cycle Analysis

In Schmidt cycle analysis the compression and expansion pistons move sinusoidally (or in this case cosinusoidally) with phase angle α. As a result, the working volume does not undergo isochoric or isothermal processes, complicating the analysis. However, there is a well-known closed form solution for the Schmidt cycle which is reproduced herein.

Substituting sinusoidal volume variations into Equation A1.2 gives:

$$M_{tot} = \frac{P}{R}\left(\frac{V_{CS,Cl}+\frac{V_{CS,sw}}{2}[1+\cos(\theta)]}{T_{CS}} + \frac{V_C}{T_C} + \frac{V_R}{T_{R,Eff}} + \frac{V_H}{T_H} + \frac{V_{ES,Cl}+\frac{V_{ES,sw}}{2}[1+\cos(\theta+\alpha)]}{T_{ES}}\right) \qquad \text{(A1.11)}$$

Where $V_{CS,Cl}$ is the clearance volume in the compression space, $V_{ES,Cl}$ is the clearance volume in the expansion space, $V_{CS,SW}$ is the swept volume in the compression space, and $V_{ES,}$sw is the swept volume in the expansion space. Equation A1.11 can be simplified by combining all constant terms and all θ dependent terms:

$$M_{tot} = \frac{P}{R}\left(C_2 + \left(\frac{V_{CS,sw}}{2T_{CS}} + \frac{V_{ES,sw}\cos(\alpha)}{2T_{ES}}\right)\cos(\theta) - \frac{V_{ES,sw}\sin(\alpha)}{2T_{ES}}\sin(\theta)\right)$$

$$C_2 = \left(\frac{V_{CS,sw}}{2T_{CS}} + \frac{V_{CS,cl}}{T_{CS}} + \frac{V_C}{T_C} + \frac{V_R}{T_{Eff\,R}} + \frac{V_H}{T_H} + \frac{V_{ES,cl}}{T_{ES}} + \frac{V_{ES,sw}}{2T_{ES}}\right)$$

Using trigonometric substitution and solving for pressure:

$$P = \frac{M_{tot}R}{C_2(1 + b\cos(\theta + \beta))}$$

$$b = \frac{\sqrt{\tau^2 + 2\kappa\tau\cos(\alpha) + \kappa^2}}{K_t}$$

$$\beta = \tan^{-1}\left(\frac{\kappa\sin\alpha}{\kappa\cos\alpha + \tau}\right) \qquad (A1.12)$$

$$\tau = \frac{T_{ES}}{T_{CS}} \qquad \kappa = \frac{V_{ES,sw}}{V_{CS,sw}} \qquad K_t = \frac{2T_{ES}C_2}{V_{CS,sw}}$$

Taking the cyclic integral of the work done in the compression and expansion spaces gives:

$$W_{CS} = \frac{M_{tot}RT_{ES}}{K_t}\int_0^{2\pi}\frac{\sin(\theta)}{(1 + b\cos(\theta + \beta))}d\theta$$

$$W_{ES} = \frac{M_{tot}RT_{ES}}{K_t}\int_0^{2\pi}\frac{\sin(\theta + \alpha)}{(1 + b\cos(\theta + \beta))}d\theta$$

Evaluation of these integrals is not trivial, but they have been solved by several different methods, one of which can be found in Urieli & Berchowitz, "Stirling Cycle Machine Analysis", 1984.

$$W_{CS} = \left(\frac{2\pi M_{tot} R T_{ES}}{K_t}\right)\left(\frac{\sqrt{1-b^2}-1}{b\sqrt{1-b^2}}\right)\sin(\beta)$$

$$W_{ES} = \left(\frac{2\pi M_{tot} R T_{ES} \kappa}{K_t}\right)\left(\frac{\sqrt{1-b^2}-1}{b\sqrt{1-b^2}}\right)\sin(\beta-\alpha)$$

$$= \left(\frac{2\pi M_{tot} R T_{ES}}{K_t}\right)\left(\frac{1-\sqrt{1-b^2}}{b\sqrt{1-b^2}}\right)\tau\sin(\beta)$$

The net cycle work is given by the sum of the work done in the compression and expansion spaces:

$$W_{Net,Schmidt} = W_{ES} + W_{CS} = \left(\frac{2\pi M_{tot} R T_{ES}}{K_t}\right)\left(\frac{1-\sqrt{1-b^2}}{b\sqrt{1-b^2}}\right)(\tau-1)\sin(\beta)$$

$$= 2\pi M R T_{CS}\left(\frac{\tau\kappa}{K_t{}^2}\right)\left(\frac{1-\sqrt{1-b^2}}{b^2\sqrt{1-b^2}}\right)(\tau-1)\sin\alpha$$

Equation A1.7 and A1.8 used in the analysis of the ideal Stirling cycle also apply to the Schmidt cycle, giving

$$\eta_{Schmidt} = \frac{\left(\frac{2\pi M_{tot} R T_{ES}}{K_t}\right)\left(\frac{1-\sqrt{1-b^2}}{b\sqrt{1-b^2}}\right)(\tau-1)\sin(\beta)}{\left(\frac{2\pi M_{tot} R T_{ES}}{K_t}\right)\left(\frac{1-\sqrt{1-b^2}}{b\sqrt{1-b^2}}\right)\tau\sin(\beta) + \oint \dot{m}_{H\_Reg}(C_v T_H - C_p T_{h,Reg})dt}$$

Considering only the Schmidt cycle with perfect regeneration gives:

$$\eta_{Schmidt} = 1 - \frac{1}{\tau} = \eta_{Carnot}$$

This analysis shows that, for engines with perfect regeneration, Schmidt cycle efficiency is equal to ideal Stirling efficiency and both are equal to the Carnot efficiency.

For the simplified case of zero dead volume the Schmidt cycle work becomes:

$$W_{Schmidt} = 2\pi MRT_{CS}\left(\frac{\tau\,\kappa}{(\tau+\kappa)^2}\right)\left(\frac{1-\sqrt{1-b^2}}{b^2\sqrt{1-b^2}}\right)(\tau-1)\sin\alpha$$

Comparing the Ideal and Schmidt Cycles

The effect of deviating from ideal motion in favor of sinusoidal motion can be seen by taking the ratio of the cyclic work for the ideal Stirling and Schmidt cycles. In general, ideal Stirling cycle work is a function of the four dimensionless parameters τ, r, K_d and τ_d. Schmidt cycle work is a function of the four dimensionless parameters τ, α, κ, and K_t. With only one dimensionless parameter in common, the ratio of Schmidt cycle work to ideal cycle work is a function of 7 independent dimensionless parameters. Restricting the analysis to engines with zero dead volume eliminates K_d and τ_d from the above equations and gives the following expression for the cyclic work ratio:

$$\frac{W_{\text{Ideal Stirling}}}{W_{Schmidt}} = \frac{\ln(r_{Ideal})}{2\pi\left(\frac{\tau\,\kappa}{(\tau+\kappa)^2}\right)\left(\frac{1-\sqrt{1-b^2}}{b^2\sqrt{1-b^2}}\right)\sin\alpha}$$

More detailed comparisons can be made by relating the working volume ratio, r, in the ideal Stirling cycle to the swept volume ratio, κ, in in the Schmidt cycle.

In general the working space volume ratio of the Schmidt cycle can be determined by:

$$V_{WS,Schmidt} = \frac{1}{2}\,V_{ES,Max}(1+\cos(\theta+\alpha)) + \frac{1}{2}\,V_{CS,Max}(1+\cos(\theta))$$

$$= \frac{V_{CS,Max}}{2}\left\{(\kappa+1) + \left(\sqrt{\kappa^2+2\kappa\cos(\alpha)+1}\right)\,\cos\left[\theta+\tan^{-1}\left(\frac{\kappa\sin\alpha}{\kappa\cos(\alpha)+1}\right)\right]\right\}$$

$$r_{Schmidt} = \frac{V_{WS\ max,Schmidt}}{V_{WS\ min,Schmidt}} = \frac{(\kappa + 1) + \left(\sqrt{\kappa^2 + 2\kappa\cos(\alpha) + 1}\right)}{(\kappa + 1) - \left(\sqrt{\kappa^2 + 2\kappa\cos(\alpha) + 1}\right)} \qquad (A1.12)$$

One method of constraining piston motion is to require the maximum and minimum working space volumes of the two cycles to be equal, forcing the working space volume ratios of the Schmidt and ideal Stirling cycles to be equal. In this case, any difference in power density can be attributed directly to thermodynamic advantages of the ideal cycle. It does not take into account the fact that, for the same limits of piston motion, the ideal cycle can achieve a higher working space volume ratio. Under this constraint the working space volume ratio of the Schmidt cycle is equal to that of the ideal cycle.

$$r_{Ideal} = \frac{V_{WS\ max,Ideal}}{V_{WS\ min,Ideal}} = \frac{V_{WS\ max,Schmidt}}{V_{WS\ min,Schmidt}} = \frac{(\kappa + 1) + \left(\sqrt{\kappa^2 + 2\kappa\cos(\alpha) + 1}\right)}{(\kappa + 1) - \left(\sqrt{\kappa^2 + 2\kappa\cos(\alpha) + 1}\right)}$$

The ratio of ideal Stirling work to Schmidt cycle work can then be calculated as a function of τ, α, and κ by substituting A1.12 into equation A1.9 and taking the ratio of the cycle work. The results of this calculation appear in Figure 6 and Figure 7 in the main text.

Although engines typically operate with phase angles near $\frac{\pi}{2}$, taking limits as the phase angle approaches 0 and π explains the differences in the behavior of the curves in Figure 6 and Figure 7 :

$$\lim_{\alpha \to 0} \frac{W_{\text{Ideal Stirling}}}{W_{\text{Schmidt}}} = \frac{\ln\left(\frac{4(\kappa+1)^2}{\kappa\,\alpha^2}\right)}{2\pi\left(\frac{\tau\,\kappa}{(\tau+\kappa)^2}\right)\left(\frac{1-\sqrt{1-b^2}}{b^2\sqrt{1-b^2}}\right)\alpha} \to \infty$$

$$\lim_{\alpha \to \pi} \frac{W_{\text{Ideal Stirling}}}{W_{\text{Schmidt}}} = \frac{\ln(\kappa)}{2\pi\left(\frac{\tau\,\kappa}{(\tau+\kappa)^2}\right)\left(\frac{1-\sqrt{1-b^2}}{b^2\sqrt{1-b^2}}\right)(\pi-\alpha)} \to \infty \; for \; \kappa \neq 1$$

$$\lim_{\alpha \to \pi} \frac{W_{\text{Ideal Stirling}}}{W_{\text{Schmidt}}} = \frac{1}{4\pi\left(\frac{\tau}{(\tau+1)^2}\right)\left(\frac{1-\sqrt{1-b^2}}{b^2\sqrt{1-b^2}}\right)} \; for \; \kappa = 1$$

This analysis explains the difference in trends seen in Figure 6-Figure 7 for when κ equals one.

A less restrictive constraint is to force the ideal Stirling cycle and Schmidt cycle to share the same limits of piston motion. This allows the ideal cycle to achieve lower minimum and higher maximum working space volume than the Schmidt cycle because in the ideal cycle one piston can dwell at the inmost and outmost position while the other traverses its full range of motion. Under this set of constraints the swept volume ratio of the Schmidt cycle, κ, is forced to unity as shown below:

$$\kappa = \frac{V_{\text{ES Sw,Schmidt}}}{V_{\text{CS Sw,Schmidt}}} = \frac{\left(V_{\text{ES max,Schmidt}} - V_{\text{ES min,Schmidt}}\right)}{\left(V_{\text{CS max,Schmidt}} - V_{\text{CS min,Schmidt}}\right)}$$

$$= \frac{\left(V_{\text{ES max,Ideal}} - V_{\text{ES min,Ideal}}\right)}{\left(V_{\text{CS min,Ideal}} - V_{\text{CS min,Ideal}}\right)} = 1$$

Under these constraints the ideal cycle working volume ratio and the Schmidt cycle swept volume ratio are decoupled. Since the ideal cycle power output is proportional to

the natural log of the ideal working volume ratio, the power density ratio, in theory, ranges from negative to positive infinity. However, running an ideal Stirling at a lower working space volume ratio than the working volume ratio of the equivalent Schmidt cycle would be counterproductive, so the Schmidt cycle working volume ratio determines the practical lower limit for the ideal cycle working volume ratio. The Schmidt cycle working space volume ratio, for κ equal to one, can be determined from Equation A1.12:

$$r_{min,Ideal} = \frac{V_{WS\ max,Schmidt}}{V_{WS\ min,Schmidt}} = \frac{\sqrt{2} + \left(\sqrt{1 + \cos(\alpha)}\right)}{\sqrt{2} - \left(\sqrt{1 + \cos(\alpha)}\right)} \qquad (A1.13)$$

Equation A1.13 appears as Equation 7 in the main text. Figure 8 - Figure 10 show the results of this analysis.

Bibliography

[1] G. Wood and N. Lane, ""“Advanced 35 W Free-Piston Stirling Engine for Space Power Applications”," in *Space Technology and Applications International Forum (STAIF)*, 2003.

[2] W. Martini, "Stiurling Engine Design Manual 2nd Ed.," NASA CR-168088, Cleveland, Ohio, 1983.

[3] I. Urieli and D. Berchowitz, Stirling Cycle Engine Analysis, Bristol: Adam Hilger, 1984.

[4] J. Senft, "Drive mechanism for Stirling engine displacer and piston and other reciprocating bodies". United State Patent US 4339960 A, 30 June 1980.

[5] A. Chertok, "Free Piston Stirling Engine Control". US Patent US 7200994 B2, 1 July 2004.

[6] J. Beggs, "Stirling cycle cryogenic cooler". United States Patent US 4389849 A, 2 October 1981.

[7] T. McWaters, "Kinematic Stirling Engine". United States Patent US 5644917 A, 13 May 1996.

[8] G. Mungas, "High Efficiency Energy Conversion". United States Patent US 20120031091 A1, 3 August 2011.

[9] D. Keiter, "Sunpower Cryotel Cryocoolers and Pulse Tube Crycoolers," 2005. [Online]. Available: http://sunpowerinc.com/library/cryocooling/. [Accessed 23 January 2015].

[10] "Free Piston Stirling Crycooler," Janis, [Online]. Available: http://www.janis.com/Products/productsoverview/FreePistonStirlingCryocooler.aspx. [Accessed 29 January 2015].

[11] Stirling Power, "Stirling Solutions in Renewable Power," Stirling Power, [Online]. Available: http://www.sp-usa.com/. [Accessed 26 January 2015].

[12] Microgen, "Your Personal Power Plant," Microgen, [Online]. Available: http://microgen-engine.com/. [Accessed 26 1 2015].

[13] "60 Years of Cryogenic Experience," Stirling Cryogenics, [Online]. Available: http://www.stirlingcryogenics.com/. [Accessed 29 January 2015].

[14] "United Sun Systems," United Sun Systems, [Online]. Available: http://www.unitedsunsystems.com/. [Accessed 29 January 2015].

[15] L. Mason, "Solar Stirlng for Deep Space Applications," NASA Glenn Research Center, Cleveland, 1999.

[16] J. Stearns, "Solar Stirling Receiver Alternatives for the Terrestrial Solar Application," Joint Propulsion Lab, Pasadena, 1986.

[17] F. S. P. Team, "Fission Surface Power System Initial Concept Definition," NASA, 2010.

[18] L. Mason, L. Qualls and D. Poston, "System Concepts for Affordable Fission Surface Power," NASA Glenn Research Center, Cleveland, 2008.

[19] M. Gibson, L. Mason, C. Bowman, D. Poston, P. McClure, J. Creasy and C. Robinson, "Development of NASA's Small Fissoion Power System for Science and Human Exploration," in *Internation Energy Conversion Engineering Conference*, Cleveland, 2014.

[20] J. Schreiber, "Assessment of the Stirling Power Option for Space Science Applications," in *Aerospace Conference*, Big Sky, 2000.

[21] S. Wilson and W. Wong, "NASA Glenn Research Center Support of the ASRG Project," in *Propulsion and Energy Forum*, Cleveland, 2014.

[22] W. Wong, S. Wilson and J. Collins, "Advanced Stirling Convertor Development for NASA RPS," in *AIAA Propulsion and Energy Forum*, Cleveland, 2014.

[23] L. Mason, "A Comparision of Fission Power Systems Options for Lunar and Mars Surface Applications," in *Space Technology and Applications International Forum*, Albuquerque, 2006.

[24] W. Graham, Stirling Engines, New York: Oxford University Press, 1980.

[25] G. Schmidt, "The Theory of Lehmann's Calorimetric Machine," 1871.

[26] J. Senft, Ringbom Stirling Engines, New York: Oxford University PRess, 1993.

[27] D. Gedeon, "Sage User's Guide," 20 June 2014. [Online]. Available: http://www.sageofathens.com/Documents/SageStlxHyperlinked.pdf. [Accessed 15 April 2015].

[28] S. Geng, M. Briggs, B. Penswick, B. Pearson and T. Godfroy, "Test Results from a Pair of 1 kWe Dual Opposed Free-Piston Stirling Power Convertors Integrated With a Pumped NaK Loop," NASA, Cleveland, 2011.

[29] S. Geng, M. Briggs and D. Hervol, "Performance of a Kilowatt-Class Stirling Power Conversion System in a Thermodynamicall Coupled Configuration," NASA, Cleveland, 2011.

[30] M. Briggs, S. Geng, J. B. Pearson and T. Godfroy, "Summary of Test Results from a 1kWe-Class Free-Piston Stirling Power Convertor Integrated with a NaK Pumped Loop," NASA, Cleveland, 2010.

[31] Briggs, "Dynamic Behavior of Kilowatt Class Stirling Convertors with Coupled Expansion Spaces," in *Nuclear and Emerging Technologies for Space (NETS)*, Albuquerque, 2012.